School of Industrial and Information Engineering
Department of Electronics, Information and Bioengineering
Master of Science in Biomedical Engineering

POLITECNICO
MILANO 1863

Master Thesis

EXPLOITATION OF A NOVEL PROCEDURE FOR THE QUANTIFICATION OF FOOT BONES ARCHITECTURE, UNDER BODY WEIGHT CONDITION: CLINICAL APPLICATION IN FLATFOOT CORRECTION

Supervisor:
Prof. Carlo Albino Frigo

Co-Supervisors:
Dr. Alberto Leardini
Dr. Claudio Belvedere

Student:
Luigi Piarulli
940648

Academic Year 2020-2021

.

Abstract

Introduction

The human foot is a very complex structure located in the distal portion of the lower limb. It is composed of 26 bones, 33 joints and more than 100 muscles ligaments and tendons. All these components work together to ensure support, load absorption, body mobility and adaptability to any kind of ground irregularity. However, the presence of such an interconnected architecture continuously charged by the body weight can easily lead to foot deformities. The most common ones are hallux valgus, hindfoot instability, pes cavus and flatfoot deformity. The latter has been characterized and evaluated during this project. A flatfoot deformity is a complex deformation that involves 3D morphological changes between the foot bones. This includes flattening of the medial longitudinal arch (MLA), hindfoot valgus and forefoot abduction. Furthermore, this kind of deformity is associated with ligaments laxity, which hinders the keeping of the bones in the right position. If this pathology is present in adult age, due to trauma, degenerations, or ligament laxity, it is called Adult Acquired Flatfoot Deformity (AAFD), even if recently a new terminology has been introduced, naming this pathology as Progressive Collapsing Foot Deformity (PCFD). This condition leads to continue foot pain and difficulties in walking or in keeping the orthostatic position, largely affecting the quality of life. In this contest, in order to support physicians in the decision-making process for indication of the treatments, the development of a repeatable, reliable, and standardized procedure for a quantitative evaluating this deformity is necessary.

State of art

In daily clinical practice, biomedical imaging is one of the most important tools in the evaluation of foot deformities and for surgical planning. Usually, clinical specialists draw geometrical measurements on 2D X-ray images or computed tomography (CT) planar projections, by tracing bones silhouettes and axes. These obviously lead to operator bias and standardization problems. Radiography (X-ray) allows for the collection of bidimensional (2D) images, where all the bones are overlapped and projected onto the plane of interest (frontal, transversal, lateral); CT allows the acquisition of three-dimensional (3D) volumes. Radiographs are the most used imaging modality in orthopaedics because they provide images in a very short time, even if these present some

drawbacks. X-rays images consist of bidimensional (2D) projections of 3D structures; hence the bones appear overlapped, making observable morphology less realistic. Moreover, the projection plane is dependent on the operator and on the relative position of the foot and the X-rays source. On the other hand, CT technology makes the harvesting of 3D structures possible, but the patient is acquired in supine position, hence not under body weight. In the last decades, the modern Cone-Beam Computed Tomography (CBCT) technology has been used in orthopaedics, overcoming these limitations and providing 3D weight-bearing CT scans. This technique allows for the acquisition of 3D structures of the foot under body weight, combining the advantages of X-rays (weight bearing) and standard CT (3D). By means of this technology, diagnosis and evaluation are becoming more and more accurate recently. Moreover, CBCT has also a high spatial resolution, low radiation dose and low time expenditure for the acquisition and for 3D elaboration. Common foot deformity quantifications are bone inclinations in frontal, lateral, and transversal planes, or relative angles between two bones, in order to assess their mutual orientation. However, in the literature, definitions and nomenclature of these measurements are not standardized, making it hard to find a large dataset of control values, which is necessary to evaluate the severity of the deformity. Some of the most common angles in the literature comprise Moreau-Costa-Bertani angle, Hibb angle and Meary's angle. Moreover, in the literature, more complex 2D measurements can be found, such as the Williamson angle, which is useful to calculate the hindfoot alignment. Recently, CBCT opened the doors to the development of new 3D measurements thanks to the exploitation of bone models. An example is the foot and ankle offset (FAO), proposed by Lintz and colleagues in 2019. This measurement is able to quantify the hindfoot alignment, using the forefoot as reference. In this contest, the procedure described in this project allows the automatic computation of traditional 2D planar angles and new 3D measurements, starting from 3D models obtained from CBCT, finally in weight-bearing, i.e., in the most realistic condition of daily living.

Materials and methods

The adopted procedure follows different steps. First of all, patients undergo a CBCT scan, in an upright single-leg posture. By using a conic beam, this technology allows for a 3D volume acquisition of the whole foot in a single rotation. Then, for each scan, virtual slicing of this 3D dataset produces 960 CT images at 0.26 mm distance, in DICOM format. Consequently, DICOM files are converted into STL files through the segmentation

process, using a state-of-art software tool (Mimics - MIS, Materialise, Belgio). Segmentation by MIS is a semi-automatic procedure, where bones contours are recognized slice by slice and it requires about 12 hours per scan on average. The final result is a 3D detailed bone model (represented in STL file format) formed by a surface mesh made of a huge number of points and triangles. This file is then imported in the Matlab environment, where traditional planar angles and new 3D measurements are computed by means of a consolidated procedure [Carrara et al., 2020]. Using an automatic statistical method, the *Principal Component Analysis* (PCA), 3D anatomical axes of each bone (antero-posterior, medio-lateral e dorsi-plantar) are defined as the three axes with the highest variance, which represent well the bone anatomical reference frame. Moreover, a global foot reference frame (FootAF), in solidarity with the foot, is defined. Therefore, all the STL models, once imported in Matlab, are aligned in the FootAF to avoid problems related to positioning of the foot during the acquisition. In addition, 3D axes computed through the PCA can be projected onto the lateral, frontal, and transversal planes of the footAF, allowing the computation of the angular and linear measures presented in this study. The presented automatic method avoids errors due to projection artefacts and foot positioning, leading to objective and complete measurements.

The aim of this thesis is to evaluate if the whole procedure described above can characterize the foot architecture and can be used to quantify the outcomes of foot and ankle surgical treatment, identifying precisely the morphological changes of the foot. In particular, 10 patients affected by AAFD were acquired through CBCT before and after the *mini bone block distraction subtalar arthrodesis* (SAMBB). This surgery has the aim of realigning the talus over the calcaneus inserting bone grafts in the sinus tarsi, that is the tunnel between these two bones. In particular, 27 automatic measurements were obtained, observing if the differences between the preoperative (pre-op) and postoperative (post-op) values were statistically significant, and if the post-op measurement are toward the right direction, i.e. those values from control. Previously, the intra-operator and inter-operator repeatability of the segmentation process was assessed using the interclass correlation coefficient (ICC), because this was the only operator-dependent phase of the whole procedure so the only one that could have repeatability issues. Finally, a qualitative approach in the comparison between pre-op and post-op models was carried out. To do this, STL files were imported in Geomagic Control X (3D Systems, Rock Hill, USA) virtual environment, where pre-op and post-op scans were overlapped keeping the

calcaneus as a reference, and thus observing the expected realignment of the remaining bone structures. In figure I, all the steps of the procedure are shown schematically.

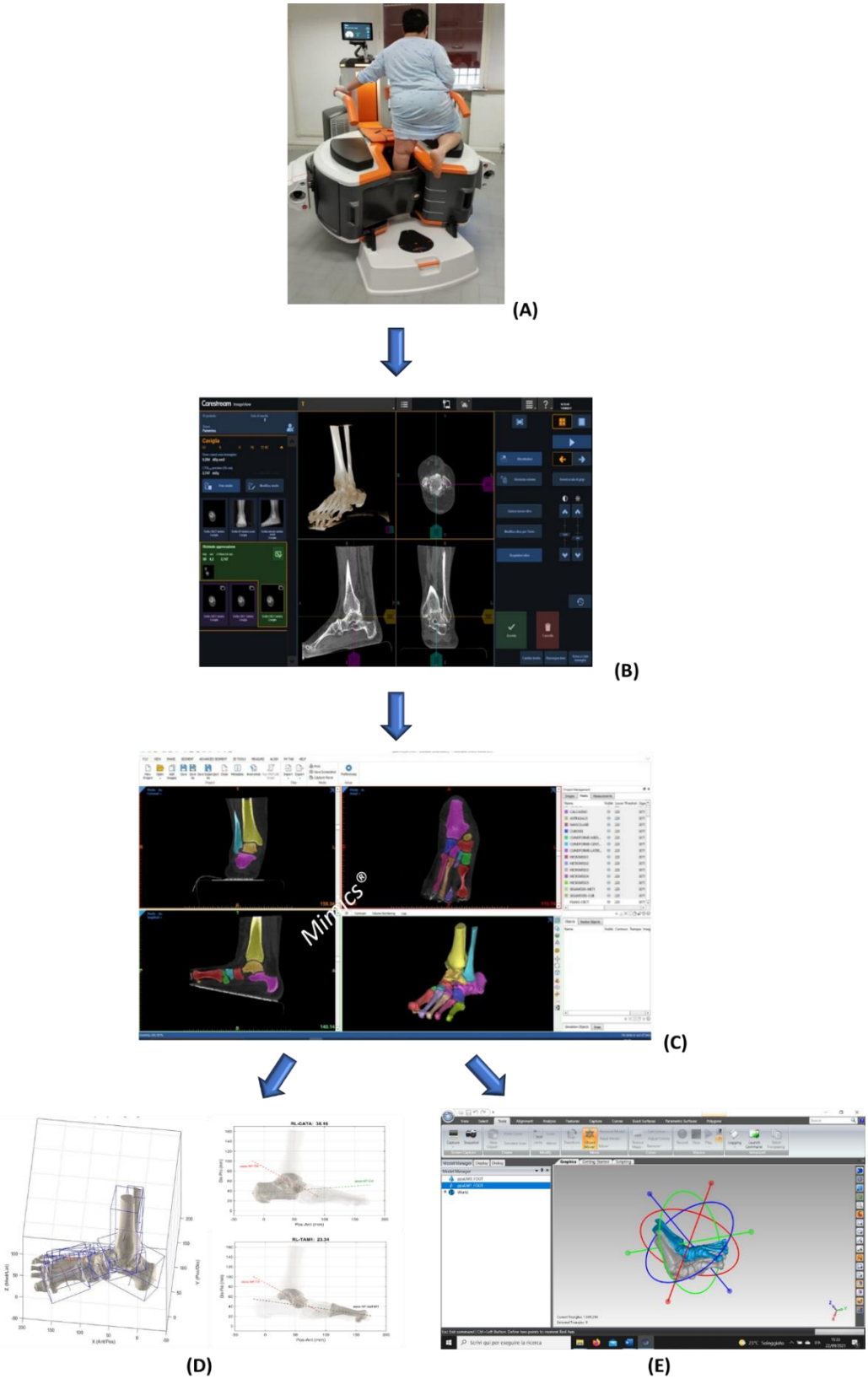

Figure I: Workflow. Acquisition of the foot by CBCT (A), three-dimensional rendering of the foot bones built up by means of an automatic image processing (B), Segmentation of the foot bones on Mimics (C), Matlab elaboration of the STL file and automatic computation of morphological measurement (D), Geomagic elaboration of STL file to obtain the qualitative comparison between pre- and post-op feet (E)

Results and discussion

First the intra-operator and inter-operator repeatability has been investigated. The former was analysed by using three different scans segmented by the same operator in three different time moments. The latter by using the same scans each segmented by three different operators. By mean of the ICCs, an excellent intra-operator and inter-operator repeatability on average has been demonstrated. The most frequent issue during the segmentation was the correct semi-automatic identification of the bone silhouettes. In fact, in a pathological foot, irregularities and osteophytes make the contours jagged, which lead to different decisions among the operators about what is the real border of the bone. Nevertheless, as shown in table I, on average, ICCs demonstrated excellent repeatability in both cases (ICC>= 0.9).

	INTRA-OP OVERALL ICC	INTER-OP OVERALL ICC
Average	0.96	0.98
sd	0.07	0.05

Table I: Average and standard deviation of the analysed measurements ICCs. They are reported for both, intra-operator, and inter-operator repeatability

Once demonstrated the repeatability of the procedure, its reliability was evaluated. 27 measurements were computed before and after the surgery with a follow up of 10 months on average, then the values were compared to those from a control population. The latter were obtained from the literature when possible, or by means of the application of the procedure on three normal feet. Such a small group of subjects cannot be considered robust, but the scan of physiological feet is actually hindered by ethical issues associated to radiation doses. Hence this reference value is considered more as an indication than a real control, useful to understand if the surgery outcomes point in the right direction. In table II reported below, the average and the standard deviation of pre-op, post-op and control values are shown.

	Pre-op		Post-op		Control	
	Average	sd	Average	sd	Average	sd
IL_TA [°]	25.4	5.9	11.7	5.0	12.7	3.5
IL_CA [°]	-8.3	4.3	-10.8	4.1	-22.0	8.0
IT_TA [°]	27.2	11.4	9.1	11.9	-23.3	1.7
IT_CA [°]	7.0	2.9	0.2	5.2	1.3	10.1
HAA_Will [°]	38.5	5.8	26.8	9.1	5.60	5.4
RL_TACA [°]	37.3	13.2	22.0	4.6	-26.7	6.0
RT_TANA [°]	-53.2	17.3	-17.6	16.6	-32.8	10.7
RL_CAM1 [°]	159.6	6.8	154.8	7.5	144.6	4.7
RL_CATAM1 [°]	139.5	8.4	126.8	6.3	114.20	5,4
RL_TAM1 [°]	-13.4	7.3	4.3	7.8	0.0	5.0
RT_TAM1 [°]	-21.6	11.8	-7.6	8.2	-10.6	6.3
RT_M1M2 [°]	-13.4	3.5	-11.1	2.6	-12.8	2.3
FAO [%]	15.0	5.3	6.8	6.0	2.30	2.9
Hg_NA_c [mm]	42.1	5.3	51.7	6.2	53.8	3.0
Hg_CU_c [mm]	33.4	4.3	33.1	3.9	37.1	3.8
Hg_CM_c [mm]	34.5	4.4	44.0	6.3	45.2	4.0
Hg_NA [mm]	23.8	6.5	36.8	7.7	39.0	4.6
Hg_CU [mm]	19.0	4.3	17.6	3.5	22.7	4.0
Hg_CM [mm]	18.4	4.0	27.1	6.1	29.3	3.8
I3_CA [°]	-8.7	4.5	-10.8	4.0	-15.5	4.1
I3_TA [°]	21.9	4.0	11.3	4.9	11.7	3.3
R3_TICA [°]	72.7	8.3	72.7	7.8	73.2	9.2
R3_TACA [°]	37.4	6.3	26.4	5.0	36.6	10.0
R3_TANA [°]	44.0	10.0	32.0	8.1	45.1	7.1
R3_CAM1 [°]	157.5	7.1	150.0	7.7	141.5	9.1
R3_CATAM1 [°]	131.1	6.2	125.8	5.0	118.8	6.4
R3_TAM1 [°]	22.8	10.3	12.7	4.6	13.0	7.7

Table II: Comparison among the pre-op, post op and control measurements. For each of them, the average and the standard deviation are reported.

From table II, it can be noticed that post-op values get closer to the control ones. Moreover, a high difference between pre-op and post-op values is shown and this is confirmed also by the statistical analysis where 24 out of 27 measurements have a p-value < 0.05, meaning a statistically significant difference. The only exceptions are the height of the centroid of the cuboid from the ground (Hg_CU_c), the 3D inclination of the calcaneus (I3_CA) and the relative angle between the 3D axes of tibia and of the calcaneus (R3_TICA). The cuboid remained at the same height on average after surgery, not the case of the navicular and the medial cuneiform. The reason is that the uprising of the MLA bones is frequently compensated by a drop of the lateral bones, such as the cuboid, may be

to keep the architecture stable. However, this lowering can be considered negligible so the value between pre-op and post-op remains similar. Hence, this result was expected and shown an improvement in the MLA bones hight. Concerning I3_CA, though the variation is not statistically significant, the calcaneus moves up after surgery, which adds the repositioning of the talus. Finally, R3_TICA is an attempt of representing the complex realignment of the hindfoot in 3D. However, this measure has a difficult geometrical consistency and interpretation. Hence, new more understandable and precise 3D measurements of the hindfoot alignment should be defined.

The last analysis about post-op outcomes is a qualitative comparison of 3D models, where bone structures from pre-op and post-op scans are superimposed. One example is shown in figure II.

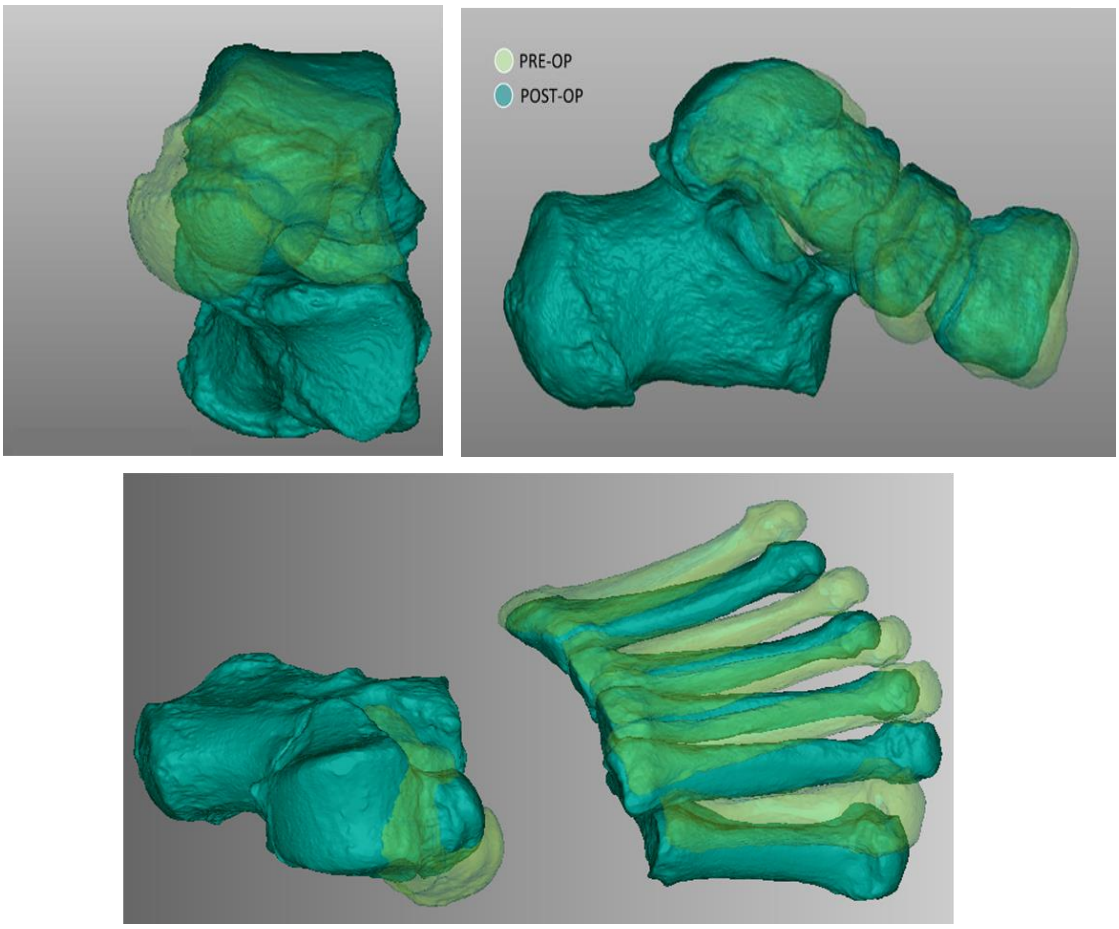

Figure II Graphical representation of superimposition of the pre-op and post-op bone structures. On the top-left the frontal view of the hindfoot is shown, on the top-right the MLA bones on the lateral view are shown, in the bottom the forefoot modification is observable. Post op scan is in blue, pre-op is in light green

Although this is simply a qualitative comparison, this image is another evidence of the data reliability. For instance, in this foot the inclination of the talus on the transversal plane is reduced, passing from 40.9° to 16.8°. The navicular and the medial cuneiform uprise from a value of 38.2 mm (Hg_NA_c) and 30.8 mm (Hg_CM_c) to 47.5 mm and 39.5 mm, respectively. Finally, the abduction of the forefoot with the respect to the talus (RT_TAM1) reduced its absolute value passing from an inclination of -36.8 ° to -9.1°. Beside confirming the numerical results, qualitative images are particularly appreciated by clinicians, because the changes in the foot bones architecture are easily figured out, thus improving also the communication between surgeons and engineers (and may be between surgeons and patients) and enhancing the interpretation of numerical results.

Eventually, exploiting the presented technique for the analysis of foot morphology, it is also possible to observe and study differences among the patients. For example, similar hindfoot realignment can lead to different modifications in the rest of the foot. For instance, the whole correction of the foot is affected by patient age, pathology, deformity severity and soft tissue laxity. Sometimes only tue hindfoot correction is not enough and should be combined with corrective surgery of the midfoot or the forefoot.

Conclusions

The described procedure has proved to be repeatable and reliable, allowing a precise characterization of AAFD pre-op and the possible improvements post-op in bone relationships as achieved by surgery. This method can be valuable in the evaluation of the severity of the deformity, in the surgical planning and in the evaluation of the outcomes. However, this work has a number of limitations. Regarding CBCT technology, standardization of the overall posture is still needed, so that also the amount of load can be more exactly controlled. Moreover, the image acquisition is limited by the size of the field-of-measurement of the scanner in the specific CBCT device used for the acquisitions (Carestream, in this work). In fact, some scans presented not fully visible metatarsal heads, resulting in a lack of accuracy for those measurements involving the metatarsal axis. As concerns the automatic PCA technique, it calculates the bone reference frames automatically. This might result, for some irregular foot bones, in a non-traditional representation of the anatomical axes. An example is represented by RT_TANA, which involves the talus and the navicular and shows higher values for the standard deviations. In addition, the data are compared with a small reference group. This procedure should be

applied to a higher number of physiological subjects, to have a more robust control dataset for the evaluation of pre-op and post-op scans.

In the future, new automatic measurements may be integrated to those presented here, making the comprehension of foot architecture more complete, especially in the characterization of 3D hindfoot alignment. Moreover, the advent of artificial intelligence may use a dataset of similar measurements to support more precisely the decisional process in clinics. The hope is to evaluate bone deformities more quickly, taking the best and most ethical choices for the patient health.

In conclusion, the present technical analysis and clinical exploitation demonstrate for the first time that a careful 3D measure of the overall foot bone architecture in weight bearing by using semi-automatic tools is feasible, reliable, and valuable; this has revealed, for the first time, the complex and full realignment of the foot bones resulted from a cautious and simple surgical treatment. This opens the door to exploitation in other pathologies and treatments, as well as additional measures, more comprehensive and may be volumetric.

Sommario

Introduzione

Il piede umano è una struttura altamente complessa situata nella parte distale dell'arto inferiore. Questo è formato da 26 ossa, 33 articolazioni e più di 100 tra muscoli tendini e legamenti. Tutte queste componenti lavorano insieme per permettere il supporto e l'assorbimento dei carichi, la mobilità dell'intero corpo e l'adattabilità ad ogni tipo di irregolarità nel terreno. Tuttavia, la presenza di tante componenti interconnesse tra loro e un persistente carico elevato su di esse, porta anche allo sviluppo più probabile di deformità. Alcune tra le più comuni sono l'alluce valgo, l'instabilità del retropiede, il piede cavo e il piede piatto. Quest'ultimo, in particolare, sarà studiato e valutato nel corso di questo progetto.

Il piede piatto e una deformità complessa che comprende malformazioni 3D nell'architettura ossea del piede. Le più comuni sono l'appiattimento dell'arco mediale, la valgia del retropiede e l'abduzione dell'avampiede. Inoltre, spesso questo tipo di deformazione è associata ad una lassità delle strutture legamentose, che non riescono più a tenere le ossa nella posizione corretta. Se il piede piatto viene acquisito in età adulta, a seguito di traumi, degenerazione o lassità dei legamenti, assume il nome di deformità acquisita di piede piatto dell'adulto (AAFD), oppure, come recentemente è stato proposto, deformità da collasso progressivo del piede (PCFD). Questa patologia può causare una riduzione della qualità della vita, per via dei persistenti dolori e difficoltà nel camminare o anche nel rimanere in posizione ortostatica. In questo contesto, si rende necessario lo sviluppo di una procedura standardizzata, affidabile e non operatore dipendente, per valutare quantitativamente il grado di deformità, supportare i chirurghi nel processo decisionale e valutare i risultati di un eventuale chirurgia.

Stato dell'arte

Nella pratica clinica ordinaria, uno degli strumenti più usati nella valutazione della deformità del piede piatto e nella programmazione della chirurgia sono le immagini biomedicali. Solitamente vengono eseguite delle misurazioni tracciando a mano il contorno delle ossa, i loro assi su lastre 2D provenienti dai raggi X oppure sulle proiezioni planari di immagini CT (tomografia computerizzata), con evidenti problemi di standardizzazione e possibili errori dipendenti dall'operatore. I raggi X forniscono, in tempi molto brevi,

immagini bidimensionali (2D) in cui sono visibili tutte le strutture ossee del piede proiettate sul piano di interesse (frontale, trasversale o laterale). Tuttavia, la proiezione 2D di una struttura 3D, induce la sovrapposizione delle ossa rendendo la morfologia osservabile meno realistica. Inoltre, il piano di proiezione, e quindi l'immagine risultante dipendono fortemente dall'operatore e dal posizionamento del piede e della fonte dei raggi. La CT è in grado di fornire invece volumi tridimensionali (3D), ma il paziente viene acquisito in posizione supina, catturando immagini dell'architettura del piede in mancanza di carico. Negli ultimi decenni, l'avvento dell'utilizzo della moderna tecnologia Cone-Beam Computed Tomography (CBCT) in ambito ortopedico sembra superare questi limiti, fornendo l'accesso a scansioni ossee 3D del piede come nella CT, ma sotto l'effetto del carico corporeo, come nei raggi X. Grazie a questa tecnologia le potenzialità per una diagnosi più accurata e affidabile e la capacità di ottenere un risultato più realistico sono notevolmente migliorate negli ultimi anni. I suoi vantaggi comprendono anche l'elevata risoluzione spaziale la bassa dose di radiazioni e i tempi rapidi di acquisizione delle immagini e di post-elaborazione.

Nella valutazione della deformità, solitamente si valuta l'inclinazione delle ossa nei piani frontale, laterale e trasversale e gli angoli relativi due ossa diverse, per valutarne il loro rapporto geometrico. Tuttavia, nella letteratura spesso la definizione e la nomenclatura di queste misurazioni risulta molto variabile, rendendo difficile anche trovare un campione di controllo numeroso, che sarebbe necessario per valutare il grado di deformità. Alcune delle misure più comuni sono l'angolo di Moreau- Costa-Bertani, l'angolo di Hibb e l'angolo di Meary. In letteratura sono presenti anche costruzioni geometriche 2D più complesse, come l'angolo Williamson, che ha come obiettivo la valutazione dell'allineamento del retropiede. Recentemente, tuttavia l'avvento della CBCT ha posto le basi per lo sviluppo di nuove misurazioni 3D, sfruttando i modelli ossei, che rendano più affidabile la stima della deformità. Un esempio è il *foot and ankel offset* (FAO), proposto da Lintz e colleghi nel 2019. Questa misura ha lo scopo di valutare la deformazione complessiva del piede, quantificando l'allineamento del retropiede, utilizzando l'avampiede come riferimento. In questo contesto si inserisce la procedura descritta in questo progetto, che rende possibile il calcolo dei tradizionali angoli planari 2D e di nuove misure 3D in modo automatico, partendo da modelli ossei 3D ottenuti tramite CBCT, finalmente sotto il peso corporeo, quindi nella condizione più comune nella vita di tutti i giorni.

Materiali e metodi

Il procedimento messo a punto si svolge seguendo diversi passaggi. Prima di tutto il piede del paziente viene scannerizzato utilizzando la CBCT, in postura eretta su una singola gamba. Il macchinario sfruttando un raggio conico è in grado di ottenere una visualizzazione 3D del piede da numerose angolazioni, dunque, al contrario delle CT tradizionali, è sufficiente una singola rotazione attorno alla gamba per avere un volume 3D ben definito. La scansione del piede viene affettata virtualmente, producendo un dataset di 960 immagini CT alla distanza di 0.26 mm l'una dall'altra, nel formato DICOM. Questa suddivisione del volume è necessaria per permettere il passaggio successivo. Questo prevede infatti di convertire il file DICOM in un file STL, utilizzando il software Mimics (MIS, Materialise, Belgio) che rappresenta il gold standard, attraverso un processo di segmentazione semi-automatica. In questa procedura vengono riconsciuti i contorni delle ossa fetta dopo fetta, richiedendo in media 12 ore di lavoro per ogni paziente. Il risultato finale è un modello 3D (il file STL) molto dettagliato e preciso, formato da numerosi punti e triangoli che costituiscono la mesh della superficie esterna delle ossa. Il file così ottenuto viene importato su Matlab, dove vengono calcolati in modo automatico i tradizionali angoli planari (2D) e quelli nuovi tridimensionali (3D) delle ossa del piede attraverso una procedura consolidata [Carrara et al., 2020]. Secondo questa tecnica, viene utilizzata una procedura statistica automatica, la *Principal Component Analysis* (PCA) con la quale si definiscono gli assi anatomici 3D di ogni segmento osseo (antero-posteriore, medio-laterale e dorso-plantare) come i tre assi geometrici a varianza maggiore, che rappresentano bene un sistema di riferimento anatomico specifico per ciascun osso. Inoltre, viene definito un sistema di riferimento solidale con il piede, denominato *foot anatomical reference frame* (FootAF), nel quale tutti i modelli STL, una volta importati nell'ambiente di programmazione Matlab, vengono riallineati, così da eliminare problematiche relative all'allineamento del piede nel macchinario. Gli assi calcolati dalla PCA, quindi, rappresentano assi 3D nel FootAF e possono essere proiettati sui piani laterale, frontale e trasversale del suddetto sistema di riferimento, consentendo il calcolo delle misure angolari e lineari presentate in questo studio. Le fonti di errore come gli artefatti da proiezione, il posizionamento del piede e l'identificazione soggettiva dei punti di repere, vengono così rimosse, portando a misurazioni oggettive e complete.

L'obiettivo della tesi è valutare se la procedura appena descritta sia in grado di caratterizzare l'architettura delle ossa del piede e se può essere utilizzata per fornire una

valutazione quantitativa del risultato di una chirurgia sul piede esulla caviglia, riuscendo a individuare in modo preciso le variazioni morfologiche di un piede. Più nel dettaglio, 10 pazienti affetti da AAFD sono stati acquisiti tramite CBCT prima e dopo l'applicazione della tecnica chirurgica *mini bone block distraction subtalar arthrodesis* (SAMBB), che mira a ripristinare il corretto rapporto tra astragalo e calcagno inserendo innesti ossei nel sinus tarsi, cioè il tunnel tra le due ossa. In particolare, sono state valutate 27 misurazioni ottenute automaticamente, osservando se la differenza tra prima e dopo l'operazione fosse statisticamente significativa e osservando se fosse avvenuto un avvicinamento dei valori a quelli di un controllo. Precedentemente, si è analizzata la ripetibilità intra-operatore e inter-operatore del processo di segmentazione, poiché questa è l'unica fase operatore-dipendente, utilizzando i coefficienti di correlazione interclasse (ICC).

Infine, all'analisi quantitativa, si è accompagnata un'elaborazione più qualitativa. In questo approccio, i file STL ottenuti a seguito della segmentazione sono stati importati nell'ambiente virtuale del software Geomagic Control X (3D Systems, Rock Hill, USA). Qui sono stati sovrapposti gli STL delle ossa delle scansioni preoperatorie e postoperatorie tenendo il calcagno come riferimento, e quindi osservando come si sono riallineate le restanti strutture ossee.

Nella figura I sono rappresentati in modo schematico tutti i passaggi della procedura.

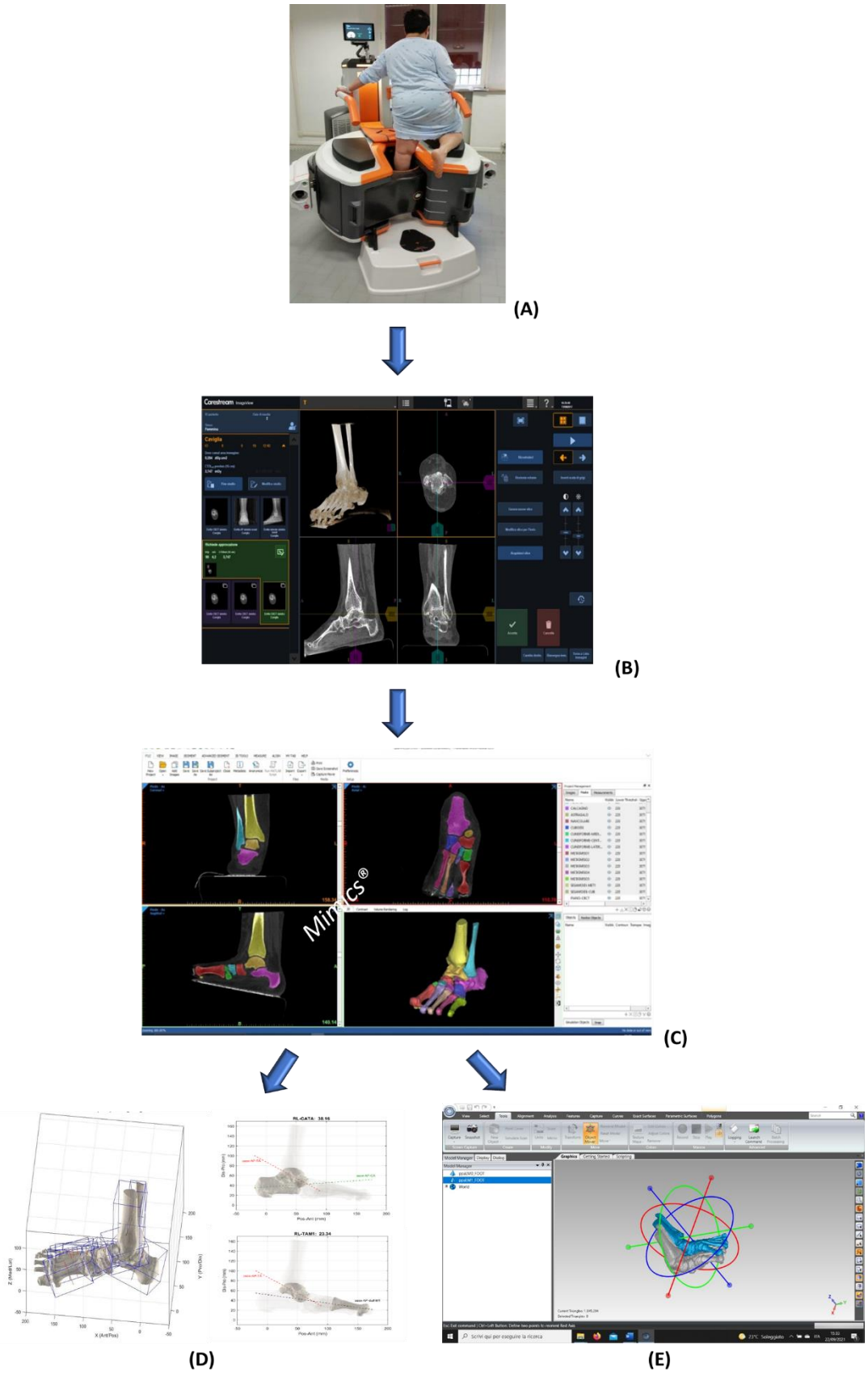

Figura I: Passaggi della procedura. Acquisizione del piede tramite CBCT (A), rappresentazione 3D delle ossa del piede costruita attraverso una lavorazione automatica dell'immagine (B), Segmentazione delle ossa del piede su Mimics (C), elaborazione Matlab del file e calcolo automatico delle misure morfologiche (D), elaborazione Geomagic del file STL per ottenere una comparazione qualitativa tra i piedi pre-op e post-op (E).

Risultati e discussione

Come primo passo, sia la ripetibilità intra-operatore che la ripetibilità inter-operatore è stata investigata. La prima è stata calcolata utilizzando tre scansioni, segmentate tre volte dallo stesso operatore in tre momenti temporali distinti. La seconda ha adoperato le stesse scansioni, facendole segmentare da tre operatori diversi. Il problema più frequente nella segmentazione è l'individuazione semi-automatica corretta dei contorni ossei. Infatti, in un piede deformato possono

essere presenti contorni frastagliati, osteofiti o porosità, che posso portare a diverse decisioni tra gli operatori riguardo quale sia il reale contorno dell'osso. Ciononostante, Come mostrato nella tabella I, in media, le ICC hanno dimostrato una eccellente ripetibilità in entrambi i casi (ICC >= 0.9)

	INTRA-OP OVERALL ICC	INTER-OP OVERALL ICC
Average	0.96	0.90
sd	0.07	0.18

Tabella I: Media e deviazione standard degli ICC ottenuti sulle misurazioni analizzate, sia per l'analisi di ripetibilità intra-operatore che per quella inter-operatore

Una volta dimostrata la ripetibilità della procedura, si è valutata la sua affidabilità. 27 misurazioni sono state registrate prima e dopo la chirurgia con un follow-up medio di 10 mesi. I valori sono stati poi confrontati con quelli di un controllo. Questi valori sono stato ottenuto quando possibile dalla letteratura, altrimenti attraverso l'applicazione della procedura su tre piedi considerati normali. Il campione non è statisticamente robusto, ma a causa di problemi etici non è possibile eseguire delle scansioni tomografiche su pazienti sani. Quindi, questo valore è da ritenersi solo un riferimento, più che un vero controllo, utile a capire se i valori dopo la chirurgia sono andati nella giusta direzione. Di seguito, nella tabella II sono riportati i valori medi e le deviazioni standard delle misure pre-op, post-op e di controllo.

	Pre-op		Post-op		Control	
	Average	sd	Average	sd	Average	sd
IL_TA [°]	25.4	5.9	11.7	5.0	12.7	3.5
IL_CA [°]	-8.3	4.3	-10.8	4.1	-22.0	8.0
IT_TA [°]	27.2	11.4	9.1	11.9	-23.3	1.7
IT_CA [°]	7.0	2.9	0.2	5.2	1.3	10.1
HAA_Will [°]	38.5	5.8	26.8	9.1	5.60	5.4
RL_TACA [°]	37.3	13.2	22.0	4.6	-26.7	6.0
RT_TANA [°]	-53.2	17.3	-17.6	16.6	-32.8	10.7
RL_CAM1 [°]	159.6	6.8	154.8	7.5	144.6	4.7
RL_CATAM1 [°]	139.5	8.4	126.8	6.3	114.20	5,4
RL_TAM1 [°]	-13.4	7.3	4.3	7.8	0.0	5.0
RT_TAM1 [°]	-21.6	11.8	-7.6	8.2	-10.6	6.3
RT_M1M2 [°]	-13.4	3.5	-11.1	2.6	-12.8	2.3
FAO [%]	15.0	5.3	6.8	6.0	2.30	2.9
Hg_NA_c [mm]	42.1	5.3	51.7	6.2	53.8	3.0
Hg_CU_c [mm]	33.4	4.3	33.1	3.9	37.1	3.8
Hg_CM_c [mm]	34.5	4.4	44.0	6.3	45.2	4.0
Hg_NA [mm]	23.8	6.5	36.8	7.7	39.0	4.6
Hg_CU [mm]	19.0	4.3	17.6	3.5	22.7	4.0
Hg_CM [mm]	18.4	4.0	27.1	6.1	29.3	3.8
I3_CA [°]	-8.7	4.5	-10.8	4.0	-15.5	4.1
I3_TA [°]	21.9	4.0	11.3	4.9	11.7	3.3
R3_TICA [°]	72.7	8.3	72.7	7.8	73.2	9.2
R3_TACA [°]	37.4	6.3	26.4	5.0	36.6	10.0
R3_TANA [°]	44.0	10.0	32.0	8.1	45.1	7.1
R3_CAM1 [°]	157.5	7.1	150.0	7.7	141.5	9.1
R3_CATAM1 [°]	131.1	6.2	125.8	5.0	118.8	6.4
R3_TAM1 [°]	22.8	10.3	12.7	4.6	13.0	7.7

Tabella II: Confronto tra le misurazioni prese in media tra i pazienti delle scansioni preoperatorie, postoperatorie e di controllo

Dalla tabella II si osserva una differenza importante tra le misure pre-op e post-op, con un avvicinamento ai valori di controllo. Inoltre, è stata eseguita anche una statistica e, considerando un a p-value < 0.05 significativo, 24 misurazioni su 27 hanno mostrato una differenza statisticamente significativa tra i valori pre-op e post.op. Le uniche eccezioni sono state l'altezza del centroide del cuboide (Hg_CU_c), l'inclinazione 3D del calcagno I3_CA e l'angolo relativo tra gli assi 3D tibia e calcagno (R3_TICA). Il cuboide in media è rimasto alla stessa altezza dopo l'operazione al contrario del navicolare e del cuneiforme mediale. Il motivo è che un innalzamento delle ossa dell'arco mediale del piede, è spesso compensato da un abbassamento delle ossa laterali, tra cui il cuboide, probabilmente per un rendere la nuova architettura stabile. Questo abbassamento, tuttavia, può essere considerate trascurabile, dunque la misura rimane molto simile tra pre-op e post-op. Quindi, questo risultato è positivo e aspettato e indica un innalzamento delle ossa del MLA. Riguardo I3_CA, la variazione non è statisticamente significativa perché il calcagno si muove verso

l'alto dopo la chirurgia, seguendo il riposizionamento dell'astragalo. Infine, R3_TICA è un tentativo di rappresentare in 3D il complesso riallineamento del retropiede, tuttavia questa misura ha una consistenza e una comprensione geometrica difficile, e bisognerebbe sviluppare delle misure 3D riguardanti questo allineamento più precise e comprensibili.

In ultima analisi è stata eseguita una comparazione qualitativa delle immagini dei modelli 3D sovrapposti di piedi pre-op e post-op. Un esempio è rappresentato dalla figura II.

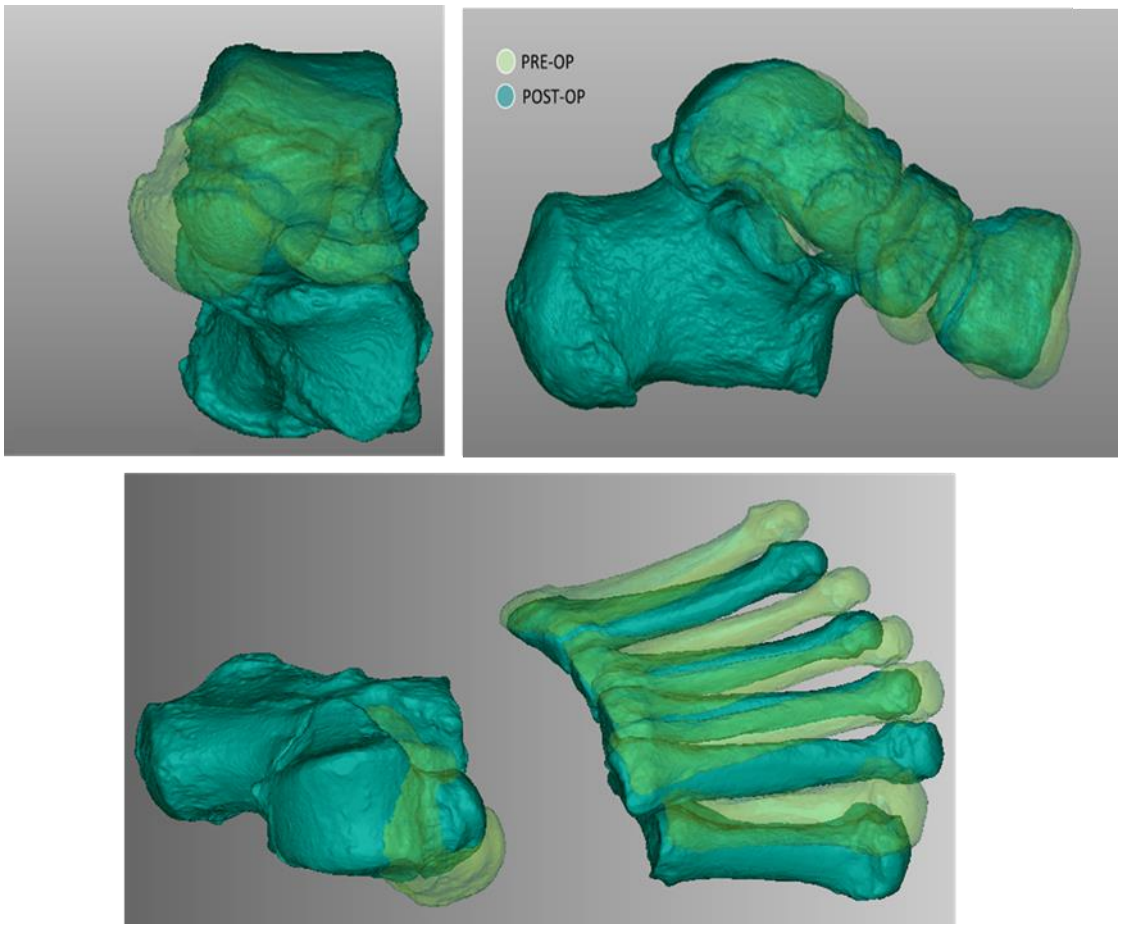

Figura II rappresentazione delle strutture ossee delle scansioni pre-op e post-op sovrapposte. In alto a sinistra è raffigurato il retropiede visto frontalmente, in alto a destra sono mostrate le ossa dell'arco mediale e in basso si osserva la modifica sull'avampiede. Il piede post-op è rappresentato in blu, mentre quello pre-op in verde chiaro

Anche se è solo una comparazione qualitativa, questa è un ulteriore prova dell'affidabilità delle misurazioni, che trovano conferma in questa immagine. Infatti, per questo piede l'inclinazione dell'astragalo sul piano trasversale rispetto all'asse longitudinale del piede (IT_TA) si è ridotta, passando da 40.9° a 16.8°. Il navicolare e il cuneiforme mediale si sono alzati, passando da un valore rispettivamente di 38.2 mm (Hg_NA_c) e 30.8 mm (Hg_CM_c) a 47.5 mm e 39.5 mm. Infine, l'abduzione dell'avampiede rispetto

all’astragalo, visibile dalla misura RT_TAM1, il cui valore assoluto si è ridotto, passando da un’inclinazione di -36.8 ° a -9.1°. Le immagini qualitative oltre a confermare i risultati numerici, sono particolarmente apprezzate dal personale medico, poiché il cambiamento dell’architettura del piede viene facilmente compreso, aiutando a interpretare meglio i valori numerici e migliorando quindi la comunicazione tra ingegneri e chirurghi o tra chirurghi e pazienti.

Infine, sfruttando questa analisi della morfologia del piede, è anche possibile osservare differenze tra i vari pazienti. Può capitare infatti che un riallineamento simile nel retropiede porti a diversi cambiamenti nel resto del piede. La correzione complessiva, infatti dipende dall’età del paziente, dal grado di deformità, dalle patologie e dalla lassità dei tessuti molli. In alcuni casi, ad esempio, non è sufficiente riallineare il retropiede per ottenere un riallineamento complessivo del piede, ma andrebbe combinato ad una chirurgia correttiva anche nelle ossa del mediopiede o dell’avampiede.

Conclusioni

La procedura descritta in questo lavoro si è dimostrata ripetibile e affidabile, rendendo possibile caratterizzare in modo preciso a morfologia dei piedi affetti da AAFD pre-op e il miglioramento delle relazioni ossee ottenuto a seguito di una chirurgia correttiva. Questo metodo può essere un valido alleato nella valutazione del grado di severità di una deformazione, nella pianificazione chirurgica e nella valutazione dei risultati. Tuttavia, il lavoro presentato ha alcune limitazioni. Riguardo la modalità di acquisizione CBCT, sono necessari standard riguardanti il posizionamento del piede all’interno del macchinario, per avere anche un carico sul piede più controllato, inoltre la CBCT ha un campo visivo limitato e talvolta può capitare che parte della testa del primo metatarso non venga catturato rendendo meno affidabili anche le misure che riguardano il suddetto osso. Riguardo la PCA, la tecnica ha il grande vantaggio di essere automatica, ma in caso di ossa dalla geometria irregolare, gli assi che si ottengono sono diversi da quelli calcolati nel modo tradizionale. Un esempio è RT_TANA, che coinvolgendo astragalo e navicolare, presenta valori variabili da un soggetto ad un altro (alta deviazione standard). Inoltre, le misure ottenute sono state confrontate con un controllo esiguo. Bisognerebbe applicare questo metodo a un numero maggiore di pazienti sani, per creare un campione normale più robusto e avere un dataset di riferimento nelle valutazioni pre-op e post-op.

In futuro sarà possibile definire nuove misure calcolabili in modo automatico da integrare a quelle già presenti, specialmente per la caratterizzazione 3D dell'allineamento del retropiede. Inoltre, l'avvento dell'intelligenza artificiale potrà utilizzare dataset di misurazioni simili a quelle presentate per supportare il processo decisionale in clinica, in modo rapido e preciso. La speranza è che in futuro saremo in grado di valutare le deformità ossee con più sicurezza, prendendo decisioni sempre più rapidamente, in modo etico e ponendo la salute e il benessere del paziente come priorità.

In conclusione, l'analisi e l'utilizzo della tecnica presente dimostra per la prima volta che la misura 3D dell'architettura complessiva delle ossa del piede, sotto il peso corporeo, attraverso strumenti semiautomatici è possibile, affidabile e valutabile. Ciò ha dimostrato il pieno e complesso riallineamento delle ossa del piede come risultato di un cauto e semplice intervento chirurgico, aprendo le porte all'utilizzo di questa tecnica in altre patologie e trattamenti.

Table of contents

List of figures

List of tables

List of abbreviations and acronyms

AAFD: Adult Acquired Flatfoot Deformity.

AP: Antero Posterior

BMI: Body Mass Index

CAD: Computer Aided Design

CBCT: Cone Beam Computed Tomography.

CT: Computed Tomography

DICOM: Digital Imaging and Communications in Medicine.

DIS: Bonelogic® Ortho Foot and Ankle, Finlandia; Disior.

footAF: foot Anatomical reference Frame

FFI: Foot Function Index.

FOV: field of view FOV

FPI: Foot Posture Index.

FAO: Foot Ankle Offset.

HAA: Hindfoot Alignment Angle.

HU: Hounsfield Units

ICC: Intraclass Correlation Coefficient

ISB: International Society of Biomechanics.

MDCT: Multi Detector Computed Tomography.

MIS: Mimics Innovation Suite, Materialise, Belgio; Mimics.

MLA: Medial Longitudinal Arch.

MR: Magnetic Resonance

MRI: Magnetic Resonance Imaging

PCA: Principal Component Analysis.

PCFD: Progressive Collapsing Foot Deformity

PTTD: Posterior Tibial Tendon Degeneration.

SAMBB: Mini Bone Block Distraction Subtalar Arthrodesis.

STL: STereo Litography.

WBCT: Weight Bearing Computed Tomography

Introduction

Foot and ankle pathologies and deformities are often causes of bad quality of life, since a damage in this body district affects the overall posture of the body starting from the inferior limbs up to the vertebral column [Caravaggi et al., 2018]. For this reason, an accurate characterization of foot deformities is essential to evaluate the degree of severity and also to plan the surgical intervention, if necessary. The type of deformity can be assessed through absolute and relative measurements of the foot bones performed on biomedical images. Examples of these measurements are bone inclination axes, their distances from the ground or angles between two bones that can be obtained by manually tracing lines on planar radiographs. However, this method presents some drawbacks, such as the bi-dimensionality of the image that leads to the overlapping of bone structures while projecting bones in a single plane, the foot positioning, the RX beam inclination and the inter-operator variability [Leardini et al., 2019]. Nowadays, thanks to the advent of CT (Computed tomography), these traditional measures can be combined with a more precise dataset of 3D measures, even though the standard CT does not allow for foot bones scans under the physiological load. To overcome this issue, WBCT (Weight-bearing computed tomography) is exploited and finally allows to obtain scans whit the patient in upright posture (single leg or double leg), i.e. with the presence of the body weight. Moreover, by means of CBCT (Cone beam computed tomography) technology, less radiation dose than traditional CT are here absorbed by the patient.

In this contest, the main focus of this study is the development and the testing of a new method to quantify the foot architecture, under body weight condition. In particular, this method is applied on patients affected by flexible flatfoot and also the subsequent evaluation of possible changes in the relationships between bones after the surgical intervention is provided. This assessment is carried out quantitatively by means of measures, computed on 3D models of the foot bones. In order to obtain these models, DICOM files from CBCT have been converted into STL format through the segmentation process. The latter is semi-automatic therefore it can be subjected to low repeatability. As a consequence of that, the second aim of this study is the evaluation of intra- and inter-operator variability of the segmentation process. Possible future prospective of this work

are the application of this foot bone morphology evaluation method to improve the daily clinical decision-making process and to assist surgeons in the surgical planning. Furthermore, this procedure may be extended to of other foot deformities, such as the pes cavus or the diabetic foot.

All the project phases were carried out at the “Laboratory of Movement Analysis and Functional Evaluation of Prostheses” of the Rizzoli Orthopaedic Institute in Bologna. This working group is involved with the international community of physicians, surgeons and bioengineers.

Chapter 1: Anatomy and Biomechanics of the Foot and Ankle

In this chapter a brief overview of the main anatomical structures, the anatomical planes and functional movements of the human foot and the ankle are introduced. At the end of the chapter, a paragraph is dedicated to repeatability analysis which is an important part of the present work.

1.1. Anatomical Planes

Biomechanics is the science that quantitatively studies the movement of the human body (kinematics) and the forces that determine and modify it (dynamics). The anatomical and functional complexity of the musculoskeletal system renders the use of simplified models necessary. These are described using three principal anatomical planes (Figure 1). To define them, the orthostatic position is used as the reference position, where the body is upright, in double leg stance.

- The *sagittal or lateral plane* (XY): it is the symmetry plane that lies vertically and passes through the centre of the body, dividing it into the right and left part; a body part that is closer or further to the sagittal plane along the medio-lateral axes is said medial or lateral respectively;
- The *frontal of coronal plane* (YZ): it is the plane, perpendicular to the sagittal one, that lies vertically and passes through the centre of the body dividing it into posterior and anterior part.
- The *transversal or horizontal plane* (XY): It is the plane perpendicular to the sagittal and to the frontal ones, that lies horizontally and passes through the body centre. It divides the body in superior and inferior parts.

For a body segment, such as the shank or the foot, the terminology *proximal* and *distal* is used to describe a point that is respectively closer or further to the centre of the body.

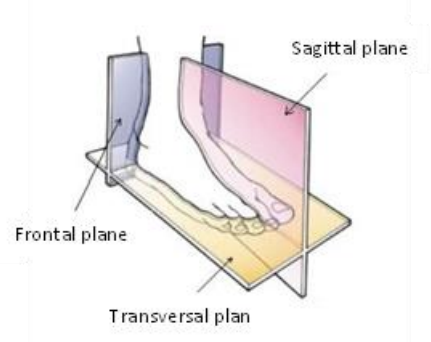

Figure 1 Anatomical planes of the foot. The sagittal plan divides the foot in medial and lateral part. The frontal plane divides the foot in anterior and posterior part and the transversal plane divides the foot in proximal and distal part [www.elearnuk.co.uk]

Three anatomical axes, originating from the centre of mass are associated to the three principal planes, in order to describe the movement of a joint.

- The *longitudinal axis* or Y axis (or proximo-distal axis): It is the vertical axis, parallel to the gravity force and formed by the intersection of the sagittal and the frontal planes. It goes from the inferior to the superior part of the body;
- The *transversal axis* or Z axis (or medio-lateral axis): It is perpendicular to the vertical axis and goes from the left to the right, it is formed by the intersection of the frontal plane with the horizontal one;
- The *sagittal axis* or X axis (or antero-posterior axis): It is the axis originating from the centre of mass and perpendicular to the other two axes. It has the direction of the walking step, and it is the intersection of the sagittal and the transverse planes.

  This is an objective description, for instance, which is used to identify the centre of mass, which is not a real anatomical point, and it is situated inside the body. Therefore, it is a limitation in the definition of the position of a point with the respect to anatomical axes. This disadvantage aggravates for the body segments, where there are not obvious symmetries, making the definition of the sagittal plane, and so of the others, not unique.

1.2. Functional movements of the foot

The human body is modelled as a chain of rigid bodies called segments that are connected by mechanical joints, representative of the anatomical joints. The foot is situated in the lower part of the body and has different functions. It not only receives static and dynamic

loads, but also gives to the body propulsion, stability during the stance and impact absorbance. These proprieties are due to the synergy between the multi articular complex of the foot and the passive structures. They are tendons and ligaments, that act as a constraint, giving stability and elasticity to the joints within the foot. The kinematic characteristics of the distal segment of the lower limb are therefore very complex. Therefore, for the sake of simplicity, to describe the functional movement of the foot, we consider it as a unique body, whose functional movement are actually a combination of the relative motions of the joints inside it.

At the current stage, there are no standards for describing the kinematics of the foot. So, in order to avoid misunderstanding, kinematics is described in accordance with the *international society of biomechanics* (ISB) [Wu et al., 2002]. Neutral position of the foot is defined as the position of the foot with respect to the leg, where the plantar plane of the former is perpendicular to the longitudinal axis of the latter, i.e. when the foot forms a 90° angle with the leg. It serves as a reference for the measurement of the amplitude of the three rotational degrees of the foot. Therefore, starting from the neutral position, the functional movements of the foot can be described as follows:

- Flexion-extension movements: These movements take place in the sagittal plane and their axis lays on the frontal and on the transversal plane. Starting from the neutral position of the ankle, dorsal flexion is the movement that brings the upper part of the foot closer to the front of the leg. On the other hand, plantarflexion sends the foot away from the leg. The flexion-extension angle is measured as the angle that the sole of the foot forms with the longitudinal axis of the leg. In dorsiflexion the maximum angle is about 30°, while in plantarflexion the foot can reach values of 50°. During gait, the range of the flexion-extension angle reaches 25°-35° but can easily exceed 60° in some activities;
- Movements of internal-external rotation: These movement occur in the transversal plane and their axis lays on the frontal and on the sagittal plane. Starting from the neutral position of the ankle, the internal rotation brings the tiptoe closer to the body symmetry plane, while the external rotations the toes away from the body symmetry plane. The internal-external rotation between foot and shank can only occur in association with adduction/abduction movements, and in that case the range of movement can be 35° - 45° . On the horizontal plane, the internal/external rotation of

the foot is obtained by a combination of internal/external rotations occurring at the knee and the hip joints.

- Inversion-eversion movement: these occur in the frontal plane with the axis of rotation lying on the sagittal and transverse planes. Inversion is the movement that turns the sole of the foot inwards, with an amplitude of approximately 50°, while the eversion orients the sole of the foot outwards. The amplitude of the latter movement is about half that of inversion and varies from 20° to 25° (Figure 2).

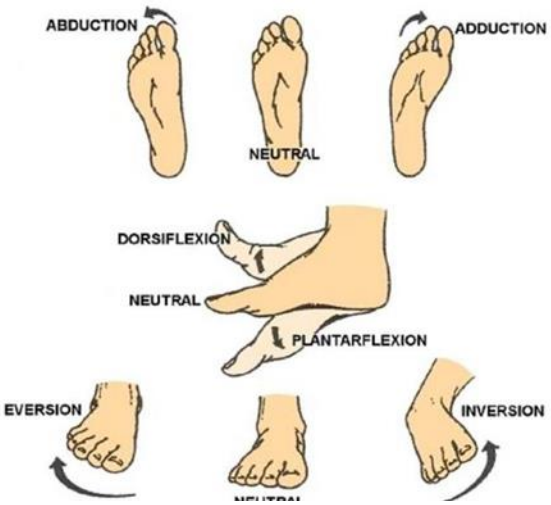

Figure 2 Functional movement of foot and ankle. Abduction/adduction in the transverse plane (top), dorsiflexion/plantarflexion in the sagittal plane (central) and eversion/inversion in the frontal (bottom) plane. [www.elearnuk.co.uk]

Beside these movements, the foot has also complex tri-planar movements which simultaneously affect all planes instead. These movement are called supination and pronation. The former is a combination of plantarflexion, internal rotation and inversion, the latter is a combination of dorsiflexion, external rotation, and eversion. The axis of the pronation/inversion goes from the lateral and plantar posterior region of the foot to the medial and dorsal anterior region.

1.3. Foot Bones

Human foot is a very complex structure situated in the distal part of the leg. It is formed by 26 bones, 33 joints and more than 100 muscles. All these structures work together to

ensure support, impact absorbance and mobility to the whole body. Moreover, the great number of structures provide a high adaptability to any kind of ground and soil. We now investigate the principal anatomical structures of the foot to better understand the morphology of the flatfoot deformation. Foot bones are divided into three sections: the tarsus, formed by 7 bones (calcaneus, talus, navicular, cuboid, three cuneiforms), the metatarsus formed by 5 bones and the 14 phalanges (named proximal, middle and distal, from the rear section of the foot to the front, respectively). Foot bones can also be grouped according to their position. The hindfoot is formed by calcaneus and talus, the midfoot by navicular, cuboid, and three cuneiforms (medial, central, lateral) and the forefoot by metatarsal bones and phalanges (Figure 3).

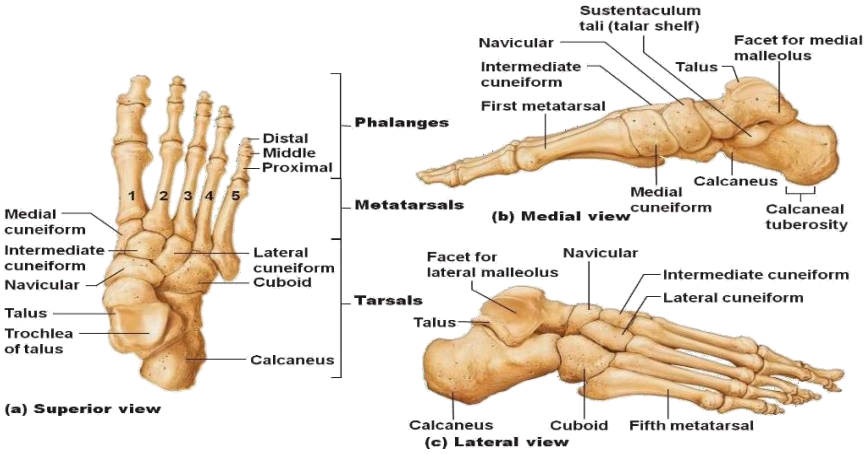

Figure 3 Arches of the foot: the longitudinal lateral arch (red), the longitudinal medial arch (green) and the transverse arch (blue). [www.pubs.rsna.org]

The foot can also be seen as a construction of a series of three intersecting arches: a longitudinal lateral arch, a longitudinal medial arch, and a transverse arch at the level of the distal tarsal bones. These arches are strictly connected, therefore, the failure of one, leads to a modification in the others. This is an example of how complex the foot is, where a single bone deformation may produce a changing in the morphology of the entire foot. The arches together have the function of weight support, and, thanks to their flexibility, they absorb the load, dynamically changing the shape during the gait. In particular, the medial arch is the highest and the most flexible. It is composed by calcaneus, talus, navicular bone, cuneiform bones and the medial three metatarsals. The lateral arch is flatter and more rigid, and comprehends the calcaneus, cuboid bone, and fourth and fifth

metatarsals. Lastly, the transverse arch runs on the frontal plane, and it is described as a composition of metatarsal bases, cuneiforms, and cuboid (Figure 4).

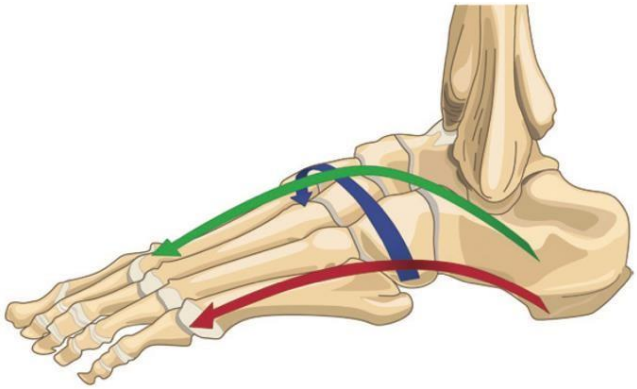

Figure 4: Foot bones in the superior (a), medial (b) and lateral (c) view. [www.healthjade.net]

As a matter of fact, sometimes a series of transverse arches of the foot is recognized, from the posterior part of the metatarsus to the anterior part of the tarsus. Arches in the foot are aligned and stable thanks to the geometry of the osseus structures, but it is not enough. Soft tissues stabilizers, such as ligaments, tendons and muscles are required to reinforce each other during the stance or the gait.

1.4. Foot Ligaments

Ligaments are a strong fibrous tissue, whose function is to stabilize joints, avoiding their luxation, and keeping them in the correct position. In general, some ligaments intervene at the extreme of the range of motions happens, hence, when the integrity of the joint is in danger.

Concerning the foot, ligaments are numerous and keep together the bone junctions, allowing articular movement. Here some of the principal ligaments:

- Medial ligament (or deltoid) supports the entire medial side of the ankle. It has a triangular shape and starts from the medial malleolus of the Tibia, spreading out into four beams, which represent other separate ligaments (Figure 5);
- Tibio-navicular ligament: It is one of the two anterior beams of the deltoid and goes to the internal and dorsal sides of the navicular bone;
- Tibio-talar ligament: It is the other of the two anterior beams of the deltoid and goes to the internal facet of the talar neck;

- Tibio-calcaneal ligament: It represents the central beam of the deltoid and fits in the *sustentaculum tali* of the calcaneus;
- Posterior tibio-talar ligament: It is the posterior beam of the deltoid and fits in the medial facet of the talus;

Figure 5 The deltoid ligament. The tibionavicular (A), tibiotalar (B), and tibiocalcaneal (C) components of the superficial deltoid ligament are shown. The posterior tibiotalar ligament (D) *is a shorter more robust ligament [Flores et al., 2019]*

- Lateral ligament supports the lateral side of the ankle. It starts from the distal part of the fibula, spreading out into three beams, which represents other separate ligaments;
- Anterior Talo-fibular ligament: It is the anterior beam of the lateral ligament and goes to the external facet of the talus;
- Calcaneo-fibular ligament: It is the central beam of the lateral ligament and goes to the external facet of the calcaneus;
- Posterior Talo-fibular ligament: It is the posterior beam of the lateral ligament and goes to the posterior process of the talus. It is thicker than the previous two ligaments;
- Talo-calcaneal ligament: It is one of the principal ligaments for the stability of the hindfoot. It prevents the subtalar joint from excessive flexion and rotation;
- Spring ligament or Plantar Calcaneo-navicular ligament: It is considered one of the principal static stabilizers of the medial arch, preventing an excessive falling of the talar head. The spring ligament consists of three portions that connect the calcaneus to the navicular bone: the supero-medial, medioplantar oblique, and inferoplantar longitudinal bundles (Figure 6). The former is the larger portion, and it is the most deformed in flat foot pathology;

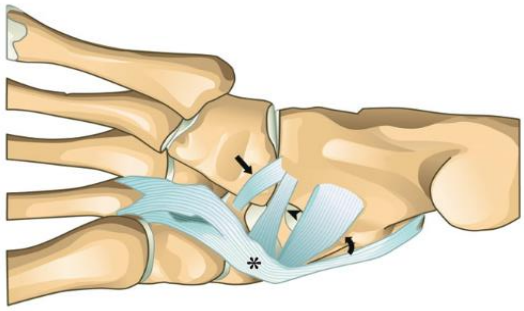

Figure 6 Spring ligament from the plantar perspective. the plantar portion of the Posterior Tibiotalar ligament (*) lies superficially to the medial navicular attachments of the spring ligament, helping to support the ligament [Flores et al., 2019]

1.5. Foot Joints

A joint is a structure that separates two or more adjacent bones to form a connection. It can be functionally classified into 3 different categories, depending on the degree of movement available between adjacent bones: synarthrosis (immobile joint), amphiarthrosis (slightly moveable joint) and diarthrosis (freely moveable joint). The foot is connected to the body through the ankle joint or tibiotalar joint. The surfaces of the distal tibia and fibula are connected by a ligament, forming a mortise which articulates with the talar dome in the central part. The lateral and the medial portion of the mortise are the lateral malleolus of the fibula and the medial malleolus of the tibia respectively. These two structures make the lateral movement of the joint negligible, therefore, this articular connection only allows the flexo-extension movement. Moreover, the joint is also stabilized by an articular capsule reinforced on the medial and lateral side by two ligaments. Talus trochlea is larger on the anterior part than on the posterior. This morphology causes a perfect lateral blockage when the foot is in extension and allows few degrees of internal and external rotation when it is in flexion. Beside the tibiotalar one, there are plenty of joints which articulate between the 28 bones of the foot, even though only some of them are considered relevant from a biomechanical point of view (Figure 7).

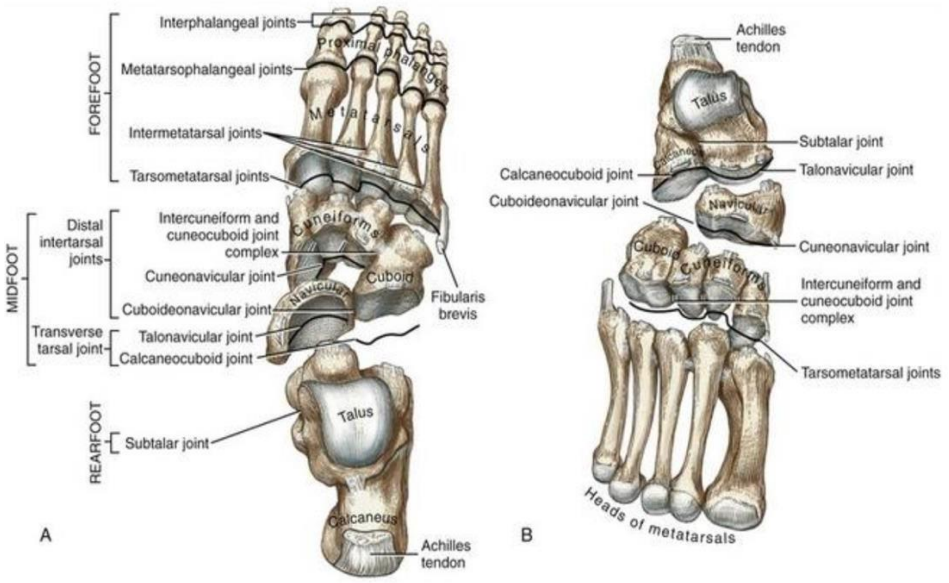

Figure 7 Principal articulations of the foot, in the dorsa (A) and plantar (B) view [www.med.upenn.edu]

Chapter 2: Fisio-pathology of the Adult Acquired Flatfoot Deformity (AAFD)

In this chapter flatfoot deformities will be described, with a special focus of the Adult Acquired Flatfoot Deformity (AAFD), along with its aetiology and classification over its different stages. An overview of the main techniques involved in flatfoot treatments will also be mentioned, with a focus on the Grice-Green technique, the surgical procedure the patients analysed in this clinical research were operated with.

2.1. Flatfoot

Foot pathologies are due to structural anatomical deformities of the bones, damage of the main ligaments and tendons and muscular imbalances. These conditions can lead to an incorrect functionality of the foot and, in the most severe cases, even to chronic pain and inability to walk. Deformations are divided into congenital, if present from birth due to genetic alteration, or acquired, which can be caused by poor posture or traumas or diseases (e.g., diabetic foot). In the present work, flatfoot deformity will be investigated, which is a complex and variable disease, with different stages of deformations and disability. Flat foot deformity can be qualitatively recognized by observing the footprint. For instance, it appears more uniform with the region under the medial arch that lies almost completely on the ground (Figure 8). This particular type of anatomical alteration occurs in most children from birth, and it usually disappears after some years, thanks to the strengthening of tendons and ligaments. In teens, if deformity persists, it may be corrected somehow by using specific orthoses, thus without surgical intervention. However, if not treated, the deformity could get worse during the adult age, leading to the need of a corrective surgery [Harris, 2010].

Figure 8 Qualitative changes in the footprint shape of a flatfoot. In the healthy foot (left), the portion under the medial longitudinal arch does not touch the ground, so it is not visible in the footprint. On the other hand, the flatfoot (right) has a more spread shape, i.e. a larger footprint of the med-foot, due to the collapse of the arch [www.mayoclinic.org].

2.2. Adult Aquired Flatfoot Deformity (AAFD)

AAFD is a very complex deformity which implies 3D modifications of the foot skeletal architecture. The most common ones are the longitudinal arch flattening, hindfoot valgus, the sliding of the talus over the calcaneus and forefoot abduction (Figure 9). In adulthood, arch flattening and excessive hindfoot pronation can affect the posture of the whole lower limb, leading to anterior pelvic tilt, internal rotation of the hip, knee valgus and internal tibia rotation [Caravaggi et al., 2018]. Several factors can cause this pathology including posterior tibialis tendon (PTT) degeneration, trauma, neuroarthropathy, neuromuscular disease, and inflammatory arthritis [Flores et al., 2019]. AAFD is usually caused by the damage of PTT, but its dysfunction is not the only factor. For instance, the cumulative damage of multiple stabilizing structures is considered a major cause. In addition to PTT, other important stabilizing structures are the talocalcaneal ligaments at the sinus tarsi, talonavicular joint capsule, deltoid and spring ligament, and other arch support ligaments, whose deficiency can occur before or after PTT degeneration [Deland et al., 2005]. PTT degeneration is caused by repetitive overloading, obesity, diabetes and inflammatory arthropathy, leading to pain, swelling, malalignment, and gait dysfunction.

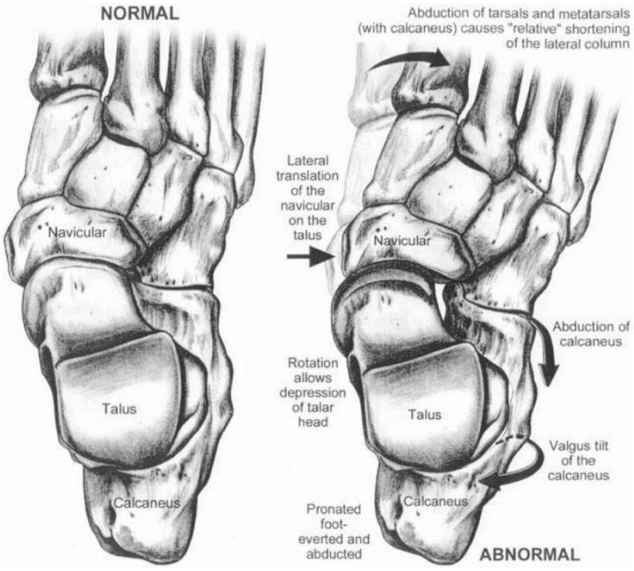

Figure 9 One of the possible effects of Flatfoot deformity: the rear- and mid- foot bones from above. Note the lateral translation of the navicular on the talus, relative shortening of the lateral column causing forefoot abduction, and valgus (and abduction) of the calcaneus. [www.digitalcommons.wustl.edu]

The importance of PTT degeneration in the AAFD is so crucial, that this condition was first described as PTT failure [Mann and Thompnson, 1985] and the severity of AAFD was classified according to the degeneration stage of this tendon. That is why, AAFD was divided firstly in three stages of severity [Johnson and Storm, 1989] and then in four stages [Myerson, 1997] (Table 1).

		Radiographs	
Stages	Deformity	Anteroposterior	Lateral
I	Pain and swelling along PTT; no deformity	No findings	May see some preexisting flatfoot
IIa	Mild flatfoot deformity, heel valgus <5 degrees, inverts past the midline, able to perform single-heel raise, minimal forefoot abduction	< 25% talar head uncoverage	< 10 degrees of collapse of the talar- first metatarsal angle
IIb	Moderate flatfoot deformity, heel valgus <15 degrees, may demonstrate inability to invert heel past the midline, difficulty with single-limb heel raise	Talar head uncoverage of between 25% and 40%	10-20 degrees of collapse at the talar- first metatarsal angle
IIc	Severe flatfoot but remains flexible, heel valgus >15, inability to invert past midline, inability to perform a single limb-heel raise, lateral subfibular impingement, severe abduction deformity	Talar head uncoverage >40%	> 20 degrees of collapse at the talar- first metatarsal angle
III	Fixed flatfoot deformity;may be able to reduce heel valgus but residual forefoot varus uncorrectable	Arthritic changes at thetalonavicular and calcaneocuboid joints may be seen; deformitytypically as described for the stage IIc	Arthritic changes notedat triple hindfoot jointswill be variable; deformity typically as described for the stageIIc
IVa	Flexible ankle valgus withunderlying flatfoot foot deformity	Evaluate ankle film forseverity of deformity and note minimal arthritic change; may utilize fluoroscopy to evaluate flexibility of the deformity	No significant ankle arthritis noted
IVb	Fixed ankle valgus deformity with flatfootdeformity	Evaluate ankle for severity of deformity and arthritis	Evaluate ankle for subluxation, joint space narrowing, osteophytes

Table 1 Stages of flatfoot deformity according to Myerson et al. 1997

However, describing AAFD only as a sort of PTT degeneration is reductive. Over the years a lot of changes in the anatomical relationships of hindfoot, midfoot and forefoot bones have been observed. Therefore, the need of a more complete classification of the stages of deformity, that does not only account for PTT degeneration, has increased. Moreover, 'stage I' as proposed by Johnson and Storm presents the absence of deformity, so the shift to the deformed PTT in stage II remains unclear. A new classification was proposed by

Myerson and colleagues to overcome these simplifications. Firstly, the deformity of the foot was divided into flexible (stage I) and rigid (stage II). Secondly, to the stage was associated one or more letter (from A to E) indicating the type or the location of the deformity (Table 2). This new classification had the purpose to better describe the deformity, taking into account all the most important deformities of the flatfoot such as the hindfoot valgus deformity (increasing of hindfoot moment arm, hindfoot alignment angle and foot and ankle offset), the midfoot/forefoot abduction deformity (decreasing in the talar head coverage and presence of sinus tarsi impingement), the forefoot varus deformity and the medial column instability. Recently, a new terminology was proposed, because it seemed to be that the term 'AAFD' may not be the correct way to refer to this complex pathology while 'Progressive Collapsing Foot Deformity (PCFD)' could be better express the idea of the worsening and collapsing of this 3D deformity [Myerson et al., 2020].

Stage of the deformity		
Stage I (flexible)		Stage II (rigid)
Types of deformity (classes – isolated or combined)		
	Deformity type/location	Consistent clinical/radiographic findings
Class A	Hindfoot valgus deformity	Hindfoot valgus alignment Increased hindfoot moment arm, hindfoot alignment angle, foot and ankle offset
Class B	Midfoot/forefoot abduction deformity	Decreased talar head coverage Increased talonavicular coverage angle Presence of sinus tarsi impingement
Class C	Forefoot varus deformity/medial column instability	Increased talus–first metatarsal angle Plantar gapping first TMT joint/NC joints Clinical forefoot varus
Class D	Peritalar subluxation/dislocation	Significant subtalar joint subluxation/subfibular impingement
Class E	Ankle instability	Valgus tilting of the ankle joint

Table 2 Classification of progressive stages of flatfoot deformity. The classification provides for the difference between flexible flatfoot (stage I) and rigid flatfoot (stage II). Moreover, the letters indicate the type of deformations that occurs in the deformation [Myerson et al., 2020]

2.3. Treatments

According to the state of the art, Myerson's classification from 1997 is still used to better indicate the most suitable treatments for AAFD, as described below.

In stage I patients can feel pain and a loss of endurance, but the tendon is not deformed, and the function of the foot is still preserved. In stage II the bones deformation starts, but it is visible only in weight-bearing: this condition is known as 'flexible flatfoot deformity' characterized by a progressive heel valgus, forefoot abduction with a consequent inability to perform a one-leg up and with a weakness of inversion of the plantar-flexed foot. In stage III the deformity becomes irreversible and in stage IV the patient shows deformities in the ankle joint in addition to the foot with the failure of the deltoid ligament, the tibiotalar joint that moves into valgus, worse lateral hindfoot valgus and tibiotalar instability and arthrosis [Flores et al., 2019].

According to the stage of the pathology, non-operative or operative treatments are recommended. Non-operative management focuses on improving patient's symptoms, usually by attempting to decrease the forces acting on the postero-medial hindfoot. This can be done by encouraging weight loss, improving footwear, decreasing repetitive loading, and other activities modifications. Nonsteroidal anti-inflammatory drugs may help in these cases, reducing pain and inflammation. Initially, patients at stage I and II may also be immobilized with removable boot or cast, followed by a specific ankle-foot orthoses device. If the initial symptoms have improved it is possible to move towards a foot orthosis, that is less cumbersome, but also less supporting [Deland et al., 2005].

Only if these first attempts do not lead to substantial changes in the foot care, different surgical treatments can be considered according to the stage of deformity. Corrective surgery has the general purpose of stabilizing the main joints of the flatfoot.

In stage I usually no surgery is performed. In stage II only some surgeons decide to treat the deformity, based on the evaluation of benefits-costs balance. With a flexible mild deformity and a damaged PTT, usually a tendon transfer from the flexor digitorum longus is chosen together with other bony procedures. These include the calcaneal osteotomy that consists in an incision made on the lateral side of the calcaneus. Consequently, the removed bone is moved to the desired location and fixed in place [www.footcaremd.org]. This procedure is meant to correct heel valgus and reduce deformations of the medial ligaments and the PTT. Surgeries involving the midfoot bones provide the metatarsal-tarsal

fusion, medial cuneiform osteotomy, or the navicular-cuneiform fusion.

For more severe stage II, the lateral column lengthening is performed, leading to the correction of the abducted talo-navicular joint and to the raising of the foot arch. The lateral column includes the calcaneus, the cuboid, and the fourth and fifth metatarsals. This procedure consists in the osteotomy of the frontal aspect of the calcaneus and the insertion of a bone graft to lengthen the column [www.footeducation.com]. However, its drawbacks include lateral foot overload, fifth metatarsal stress fracture and stiffness.

For stage III and IV, surgery is the only way to correct the deformity. In addition to the treatments reported above, more commonly, subtalar arthrodesis is performed, sometimes in combination with the fusion of the talonavicular joint and the calcaneocuboid joint [Gentchos et al., 2012]. This treatment is accomplished with an autograft, usually harvested from the tibia. Consequently to this procedure, the heel should be in $\leq 5°$ of valgus with the forefoot in neutral position and without overcorrection into varus. However, some limitations of this technique are the impossibility to walk on irregular surfaces and the increased valgus stresses at the ankle, resulting in late valgus deformity of the tibiotalar joint [Deland et al., 2005].

In conclusion, all these surgical procedures must be performed only if non-surgical treatments do not work and, accordingly to the severity of the deformity, the procedure can be a combination of the techniques shown above. Other minor interventions for the correction of the flatfoot are the reconstruction of fundamental ligaments, such as the spring and the deltoid ligaments, but these surgeries only provide an additional support for the foot heal.

2.4. Grice-Green and Mini bone block distraction subtalar arthrodesis (SAMBB) Surgery

As concerns this study, 21 patients underwent the Mini bone block distraction subtalar arthrodesis (SAMBB) Surgery. The gold standard is the Grice-Green technique, which is an extra-articular arthrodesis, described in 1952 by Grice for the correction of pes-planus in poliomyelitis patients [Grice et al., 1952]. According to this technique, the height of the tarsus is restored due to a bone graft placed in the sinus tarsi: mechanical fixation of the subtalar joint is obtained through the fusion with the graft, preventing the calcaneus from rotating and thus, blocking the heel and foot from shifting into the valgus position.

This technique has been applied especially in the correction of young people foot deformities since 1952, and, over the years it was applied for other pathologies, such as spina bifida, congenital vertical talus, talocalcaneal coalition, cerebral palsy, myelodysplasia, and idiopathic planovalgus [Mazis et al., 2012].

Due to its benefit of restoring the correct relationship of the talus with the calcaneus and the navicular, with no screw fixation, several modifications have been applied to the original technique to make it suitable for patients affected by AAFD, and SAMBB is one of them.

This technique is a modification of the Grice-Green procedure, properly adapted to adults, and has the advantage of using a structural bone graft harvested from the proximal ipsilateral tibia, instead of the iliac crest, considerably reducing the morbidity of this surgical procedure. It was initially performed at the Istituto Ortopedico Rizzoli, in Bologna [Mosca et al., 2019], and its outcome in adult patients affected by AAFD with subtalar joint osteoarthritis at a midterm follow-up has been recently reported [Mosca et al., 2020].

The SAMBB surgical procedure is about the following: Firstly, the sinus tarsi is prepared by drilling the subtalar subchondral surface to improve the recruitment of bone marrow mesenchymal stem cells, that play a crucial role in the repair of the bone and in the fusion of the graft, producing extracellular matrix. The subtalar joint is then reduced up to 5 degrees of heel valgus. The graft is cut from the ipsilateral proximal tibia and positioned into the sinus tarsi through press-fit fixation. Moreover, additional autologous cancellous chips, harvested from the proximal tibia, are pressed into the sinus tarsi to mechanically enhance fusion (Figure 10).

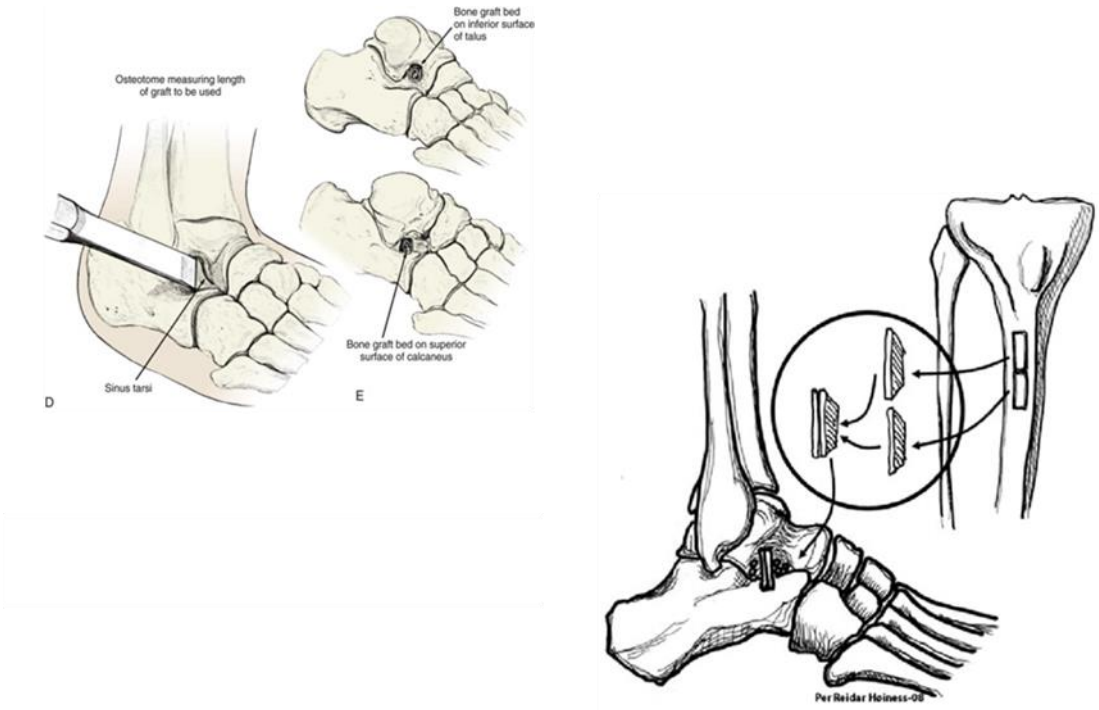

Figure 10 A diagrammatic picture of the surgical intervention taken in the operating theatre. Shaped bone graft harvested from the proximal tibia and positioned into the groove by press-fit fixation. The anatomical relationships of the bone graft with the subtalar joint structures are shown. The fusion of the graft with the bones is enhanced by extracellular matrix production [Mosca et al., 2020].

SAMBB can be performed on patients affected by AAFD with subtalar arthritis, but also in specific cases with severe joint laxity, wide synostosis, end-stage dysfunctional PTT and neurological clinical pictures.

In this current study, 21 patients were indicated for SAMBB, but only 10 of them underwent the procedure so far. Indeed, the aim of this work is the evaluation of the modification of the foot morphology after SAMBB. Therefore, patients that underwent other surgeries in addition to SAMBB were excluded from the comparison between pre- and post-op evaluation.

Chapter 3: State of art, Imaging and CBCT, review of anatomical measurement in the AAFD

Imaging has a crucial role in the pre-operative analysis of orthopaedic diseases, in the surgical planning and in the assessment of the results. In this chapter, imaging techniques used in the evaluation of AAFD will be described, with their advantages and disadvantages. These techniques include the traditional radiographs, still largely used in orthopaedics, and the innovative Cone Beam Computed Tomography (CBCT) that is used in this study. In the second part of the chapter, an overview of the principal measurements of the AAFD found in the literature is presented. Lastly, new 3D measurements in weight-bearing and a standardization of the nomenclature will be proposed.

3.1. Imaging

Medical imaging analysis has always been used to support diagnosis, evaluate the degree of deformity of the musculoskeletal apparatus and develop new techniques and treatments. Moreover, imaging can be used during surgery in order to have a direct visual access of the anatomical structure and of the implant [Leardini et al., 2019]. In the medical field, the first imaging technique was the Radiography (X-rays), developed more than 120 years ago by Röntgen. At the beginning it was a very invasive method with high doses of ionizing radiations [Kevles, 1997]. However, in recent years, the dosage of radiations has been decreasing progressively. At the same time new imaging technologies arose, including computer tomography (CT) and magnetic resonance (MR). The latter allowes to better observe soft tissue, such as cartilage and tendons, while the former and the X-rays images are commonly used to identify bone structures. In addition, it was demonstrated that a combination of CT and MR can lead to a precise characterization of the joints, because in this way both soft tissues and bones are clearly identified [Durastanti et al., 2019B]. The

development of these technologies in the last decades has led to a more accurate and rapid identification of pathologies and to a better assistance of the patient.

3.1.1. Radiography (x-rays)

Radiography is the first imaging technique used in the study of bones integrity, their geometry and alignments. Nowadays, it is the gold standard in the diagnosis of orthopaedic diseases. Radiography is a bi-dimensional representation of the absorption of X-rays by the investigated 3D object. In particular, given a certain initial X-rays beam intensity, it is exponentially attenuated in according to the mass attenuation coefficient and to the distance that the beam runs through the body. The attenuation coefficient depends, in turn, on the body density and on the beam energy. For instance, the beam will be more attenuated if the object is a material with a higher atomic number, if the energy of the beam is lower and if the thickness of the body is higher. Therefore, in X-rays images, high density objects, where the beam is highly attenuated, such as bones or metallic materials, appear more luminous and whiter, while low density tissues, i.e. ligaments and tendons, appear darker. This is the reason why X-rays images are usually used to observe bones. Moreover, X-rays imaging includes the acquisition of the patient in loading orthostatic conditions, giving more anatomically detailed bones fractures, alignments and deformities that lead to biomechanical alterations. In addition, this technique is resistant to metal artifacts and has a great bone spatial resolution. Besides, it is cheaper than the other imaging techniques. However, X-rays images have the strong limitation of being planar representations of 3D structures, hence, these depend on the foot and the beam source positioning and are inter-operator dependent. Since the superposition of the bones can distort the morphology acquired, measurements performed on radiographies are hardly repeatable, leading to less reliable clinical studies [Leardini et al., 2019].

3.1.2. Standard computer tomography CT

Computer tomography was the first digital imaging technique. It was developed by Hounsfield in 1979. CT apparatus is formed by a radiogenic source in opposition to a detector, that, rotating around the patient, scans the transversal section. The obtained signal is digitalized and sends to a computer, where a software computes the bi-dimensional distribution of absorption values of the slices and shows it on the monitor of a computer. Hence, the radiographic projections are showed as digital images, i.e. matrixes of numbers, called pixels, which correspond to a scale of grey representing the attenuation of the beam

in that specific point. New generation CTs overcome initial problems of this technique, reducing the acquisition time, and generating 3D volumes. Modern CTs are formed by a rotating machine (gantry) and a table where the patient lays. The former has detectors disposed on the opposite side with respect to the X-Rays source that rotates around the patient, obtaining a slice, while the latter moves perpendicular to the beam allowing for the acquisition of several parallel slices, one for each rotation (Figure 11). In this way the multiple slices image is elaborated by a computer that produces images representing 3D volumes, whose fundamental unit is the voxel. The more the voxel represents a small volume, the more the image will be accurate.

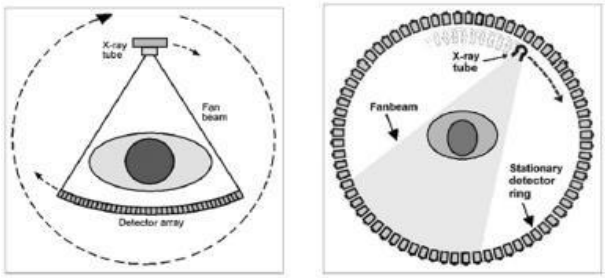

Figure 11 Old CT scans (left) and modern CT (right). The former had a higher time expenditure and a lower spatial resolution than the latter. [www.sciencedirect.com]

CT images have a high 3D spatial resolution, they are obtained in less than one minute and allow to study extended anatomical districts. However, due to its higher cost and higher radiation dosage than traditional radiographs, in orthopaedics this technique is only used for complex bone fractures and in emergency cases. In the study of foot and ankle, CT overcomes the problems related to the planar representation of the bones, avoiding the superposition of the structures. However, the acquisition is limited by the absence of the body weight. In fact, the position of the patient during the acquisition is supine and this is the reason why the relation between the foot bones results altered [Leardini et al., 2019]. To overcome this problem, several studies try to simulate the body weight in standard CT. Typically, the load is applied with a system of pulley, cables and platforms or other ad hoc apparatuses [Kido et al., 2011; Ferri et al., 2008; Zhang et al. 2012] (Figure 12). But the simulated load, that differs between 10 and 50% from the physiological body weight, underestimates subluxation of the foot joints and minor changes of the joint alignments [Hirschmann et al., 2013]. Another limitation is the application of external and passive loads, that do not imply muscular activation and relevant forces, that are usually present in

orthostatic conditions, as shown in a recent review [Barg et al., 2017]. In addition, the customized apparatus for simulating the load is cumbersome, not feasible in everyday clinical evaluation and so hardly repeatable.

Figure 12 Example of simulated loading in standard CT. The load applied is proportional to the distance between the foot plate and the knee plate. With this mechanism the simulated load is different from the real body weight. Moreover, the apparatus is customized, so the procedure is hardly repeatable [kido et al., 2011]

3.1.3. Cone beam CT (CBCT)

Cone beam computer tomography (CBCT) is a recent technology, first described in 1998 by Mozzo and colleagues [Mozzo et al., 1998]. In this technology, a rotating X-rays system moves around the centre of a circumference where the object of interest is placed. The detector and the beam source are collocated at the opposite sides of the circumference's diameter. The peculiar characteristic is the cone-shaped beam that covers the entire field of view (FOV), allowing to capture the whole volume of the object in a single rotation, reducing the time of the acquisition and the dosage of radiation. This is in contrast with the traditional CTs whose fan-shaped beam requires multiple rotations of the apparatus around the patient to obtain a large volumetric portion of the object (Figure 13).

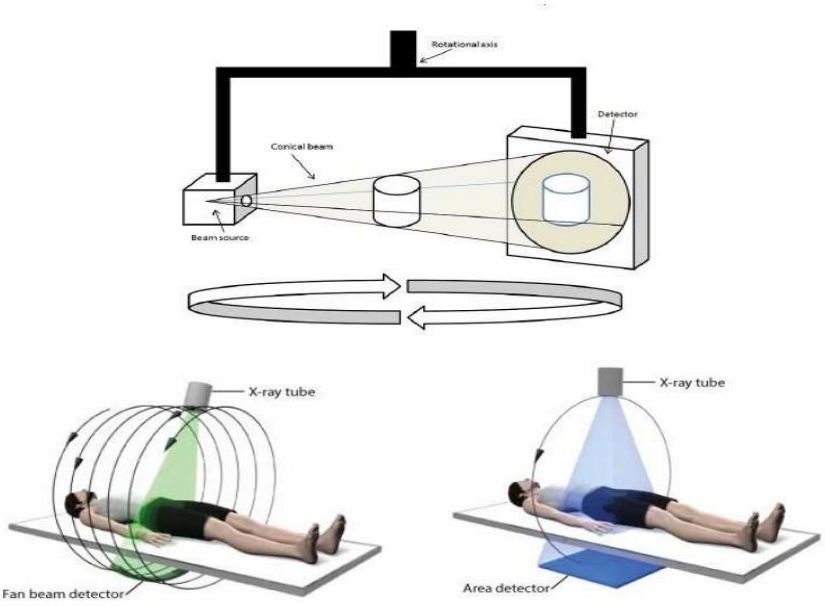

Figure 13 The functioning of the cone beam CT (top) and comparison between the fan beams of standard CT (bottom-left) and conic shape of the beam in the CBCT (bottom-right). The conic shape of the CBCT beam allows a single rotation to collect a 3D volume [www.opnews.com; www.wikipedia.org]

The cone-shaped beam ensures an isotropic spatial resolution, where the FOV is represented as a volumetric cylinder formed by millions of voxels. These are characterized by 4 dimensions, the 3 spatial coordinates (x, y, z) and the radiodensity value. For this technology, the spatial resolution depends only on the dimension of the isotropic voxels that it is lower than traditional CT (0.26 mm against 0.64 mm) [Hamard et al., 2019]. The higher resolution was also demonstrated in a study where spherical markers were segmented from CT, CBCT and other imaging techniques and compared with the 3D printed geometrical model [Durastanti et. al, 2019B]. Moreover, CBCT technology has reduced acquisition time (less than 40 seconds), radiation dose, costs and encumbrance than CT [Posadzy et al., 2018; Lintz et al., 2018; Richte et al., 2019]. However, the principal drawback of CBCT is the limited FOV, which ranges from 6 × 6 cm to maximum 18 × 16 cm, not allowing the acquisition of large volumes [Posadzy et al., 2018]. For instance, this represented a problem in the current study of AAFD because, in most of the scans, the proximal phalanges were cut, not allowing the study of the hallux valgus related to flatfoot deformity.

At the very beginning, CBCT was used in the orthodontic field, passing from traditional 2D to 3D imaging. Its first limitations, such as high costs, encumbrance and low spatial definition, were quickly overcame, so that nowadays it is the most used technology in this

field. In foot and ankle orthopaedics the interest to this technology was due to its major advantage: CBCT is able to scan the foot and the ankle under physiological weight. The first inferior limb acquisition dates back to 2013 by Touminen and colleagues. The major advantage of this technology was immediately visible because the body load allows to correctly analyse foot bones alignments and anatomical relationships, for example the reduction of the articular space in the subtalar joint.

In the current study, AAFD deformities are analysed using CBCT, because it is essential to observe this pathology under body weight. AAFD is typically identified by a flattening of the longitudinal arch, the valgus of the hindfoot and the abduction of the forefoot. It has been demonstrated that these characteristics are underestimated in absence of load [Shelton et al., 2018]. For instance, subluxation of the subtalar joint and tarsal bone shift increased under loading in patients with AAFD. Moreover, from MRI, that well highlights soft tissues, other signs of deformity can be observed, such as the failure of the spring ligaments and the posterior tibial tendon dysfunction [Kido et al., 2011]. For these reasons, nowadays, many CBCT scans are used to diagnose and evaluate deformities. Among these, Planmed Verity® Extremity Scanner is designed to find subtle and fractures hidden at the first visit to the imaging facility. The system features specialize functions and tools for extremity imaging that provide optimal imaging technique for different targets and purposes. All the targets can be reached thanks to the motorized gantry with adjustable height and tilt for the best possible extremity positioning. Another weight-bearing CT device is produced by CurveBeam: PedCat. It allows for bilateral, weight-bearing scans of the foot and ankle that give physicians the information needed to assess the biomechanical spatial relationships and alignment of the lower extremities. Moreover, PedCat gives the possibility of having a healthy-foot dataset because both feet of the patient are scanned even if the pathology affects only one foot. Concerning this work, all the acquisitions on the patients involved in this study were performed in a single leg up-right position on the OnSight 3D Extremity System by Carestream, that will be described below.

3.1.4. Onsight 3D Extremity System (by Carestream, US)

Onsight 3D Extremity System has been developed by the researchers of Carestream (Rochester, NY) and of the John Hopkins University (Baltimore, MD). This device uses the CBCT technology, and it also allows the acquisitions of the body extremities, such as foot, knee, shoulder, elbow and hand, thanks to its movable gantry, i.e. the central part of

the machine. In addition, this machine is thought to maximize the comfort of the patient allowing an easy access (Figure 14). Positioning aids help to reduce patient movements during the acquisition. Moreover, the design is thought to reduce the radiation dose, scanning only the examined part of the body, in contrast to the full body CT.

Figure 14 OnSight 3D Extremity System by Carestream [www.carestream.com]

Onsight system, as the others WBCT, has the peculiarity to acquire the patient while standing in an up-right posture, i.e. considering the presence of the body weight. As concern technical characteristics, the machine has a rotational angle of 215°, time expenditure of 25 seconds for acquisition and the FOV of 216 mm x 216 mm [Carestream Onsight 3D Extremity System, 2015]. The cone beam apparatus is formed by a high-performance flat panel detector that reduces the time for the acquisition, avoiding movement artifacts. The source, differently from the other CBCT systems, is a radiogenic tube made of three sources. The use of three sources substantially increases the volume reconstructed with respect to traditional single-source CBCT devices, as shown in the picture below (Figure 15).

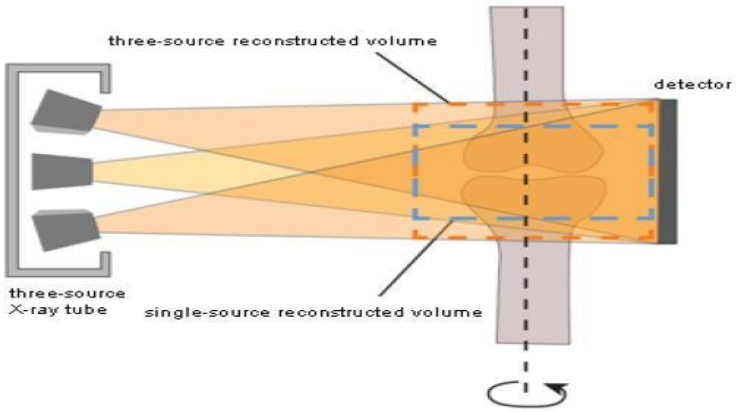

Figure 15 Volume captured by 3 cones radiogenic source. It allows to capture a higher volume compared to single cone radiogenic source [www.carestream.com].

During reconstructions of the medical imaging, sophisticated algorithms (MAR algorithms) are applied in order to reduce metal artifacts, drastically improving the quality of the imaging and the identification of bone structures. In conclusion, CBCT technology has shown the possibility of obtaining high-quality imaging of the lower limbs under the body weight, besides being low time consuming and having low radiation dose, that makes this technology suitable for clinical application [Carrino et al., 2014]. For instance, in several comparative studies the lower radiational dose of CBCT devices with respect to other imaging techniques was demonstrated [Koivisto et al.,2015, Hamard et al., 2019; Posadzy et al., 2018].

3.2. Measurements of foot architecture in the literature

AAFD is known to be a progressive and complex 3D structural deformity of the foot whose clinical assessment is obtained through imaging. As reported above, the most used imaging in orthopaedics are X-rays, MRI, and CT. For decades, all the measurements have been performed in weight-bearing but radiographically, thus missing the 3D nature of this pathology. In addition, the major axes of these bones have been traced manually by clinicians, leading also to the problem of inter-operator variability. In addition, 2D images represent the projection of 3D structures on a specific plan (sagittal, frontal, or horizontal), where the superposition of the bones can distort the morphology. As a consequence, X-

rays based measurements are hardly repeatable, making some clinical studies unreliable [Leardini et al., 2019].

Radiographic based measurements have also the strong limitation of the foot positioning in between the X-rays tube and the image plan, as demonstrated in a study about the evaluation of the first metatarsal and first metatarsophalangeal joint in different positions [Dayton et al., 2014]. On the other hand, traditional CT technology allows to acquire the 3D structure of the bones, but without the physiological weight, since the patient maintains a supine position during the acquisition. This leads to the obtainment of less reliable measurements as demonstrated in a comparative study between measurements from standard CT and WBCT [Richter et al., 2014]. Instead, MRI is usually used to highlight soft tissue structures, such as the cartilage, so it is less useful in the evaluation of foot bones relationships. In this context, CBCT has definitely the ability to demonstrate the three-dimensional relationships of the bones in a flatfoot deformity in weight-bearing condition, merging the positive aspects of both X-rays and CT [Carrara et al., 2020]. In AAFD, measurements are especially useful for evaluating longitudinal arch flattening, hindfoot valgus and forefoot abduction [Flores et al., 2019]. 2D angular measurements in the literature can be grouped according to the anatomical plane (lateral, frontal, transversal) where these are computed, and divided in absolute angles (inclination angles between a bone longitudinal axis and the ground) or relative angles (angles between the axes of two bones). Moreover, from literature, it turns out that many different ways exist, not only to name and express the same angular measurements but also to perform the relevant measure with different calculation methods. For example, the angle between the antero-posterior axis of the talus and that of the first metatarsal bone on the lateral view is usually called ‘Meary's angle’, but it can also be found as ‘Meary-Tomeno's angle’ or ‘talo-first metatarsal angle’ [Carrara et al., 2020].

3.2.1. Lateral plane

This anatomical plane is adequate to recognize the flattening of the medial longitudinal arch, the flattening of the lateral longitudinal arch or the sliding of the talus.

- Medial longitudinal arch (MLA)

This anatomical structure is fundamental in the assessment of the flat foot deformity because the flattening of MLA is one of the most evident characteristics of the AAFD,

visible even without the aid of imaging. MLA can be described using different angles. The original definition, by Moreau- Costa-Bertani, describes an MLA angle as the one with the apex in the most plantar point of the talo-navicular joint and vertexes at the most plantar points of the first metatarsal head and of the calcaneus. This classical definition can be used, for example, to evaluate the flexible flat foot deformity in children [Benedetti et al., 2010]. Recently, MLA measures have been computed in dynamic conditions, studying its changes during the gait phases that result in a smaller change in flat foot at the end of the stance [Tulaya et al., 2015]. An alternative way to see the flattening of the arch is the Hibb's angle or first metatarsal-calcaneal angle. This is the relative angle between the antero-posterior axis of the first metatarsus and of the calcaneus projected on the lateral plane [Maynou et al., 2017, Zhou et al. 2014, Gwani et al., 2017] (Figure 16). In the literature, this angle can be calculated using different plantar prominences of the calcaneus to define the inclination lines [Menz et al., 2010; Maynou et al., 2017; Zhou et al. 2014]. In this study, in order to standardize this angle, the antero-posterior axis of the calcaneus was used.

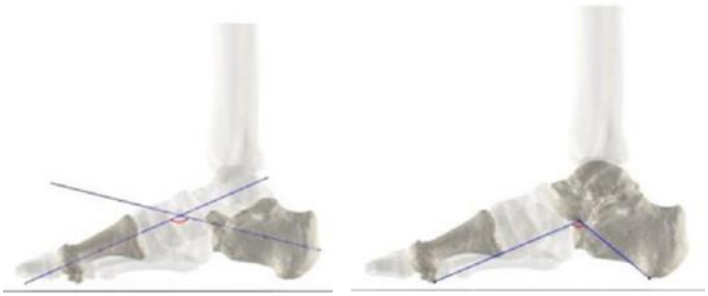

Figure 16 Two different ways to define and to calculate the angle of the medial longitudinal arch. The Hibbs angle (left) defines it as the angle between the His of the calcaneus and the first metatarsus. The Moreau- Costa-Bertani definition (right) describes it as the angle with the apex in the most plantar point of the talo-navicular joint and vertexes at the most plantar points of the first metatarsal head and of the calcaneus [Carrara et al. 2020]

To evaluate the flattening of MLA, the distances between the midfoot bones to the ground have also been proposed. These measurements are represented by the length of the line segment that joins the most plantar point of the medial cuneiform, cuboid, and navicular perpendicularly with the ground plane [Gwani et al., 2017, Shakoor et al., 2021]. These distances are also used to determine if any change in the relationship between soft tissues and bony architecture occurs, especially under load [Ferri et al., 2008].

- Lateral longitudinal arch

Even if the MLA is usually used to evaluate the flattening of the foot, in some cases the lateral arch is also observed, tracing the angle between the long axis of the calcaneus and the long axis of the 5th metatarsal bone [Gwani et al., 2017].

- Bone inclination

Usually, on the lateral view, the inclination of foot bones is studied in order to evaluate the changes in the orientation due to the deformity. In particular, these inclination angles are formed between the antero-posterior axis of each bone and the ground plane [Carrara et al., 2020]. An example is the Calcaneal inclination angle or calcaneal pitch angle. The latter represents the inclination angle of the calcaneus with respect to the ground plane in the sagittal view (Figure 17)

Figure 17 An example of inclination angle of the Calcaneus. It is called the calcaneal inclination angle or calcaneal pitch angle, defines it as the inclination of the AP axes of the calcaneus with respect of the ground [Carrara et al. 2020]

- Other measures

In general, flat foot deformity leads to the variation of the relationships between foot bones. Therefore, to have a more accurate observation of the foot in the lateral view, several other angles are reported in the literature. The most common ones are the Meary's angle, the tibio-talar angle, the talo-calcaneal angle, and the talo-navicular angle. The first one is the angle between the antero-posterior axes of the talus and the first metatarsus and shows the collapse of the forefoot with respect to the talus [Maynou et al., 2017; Zhou et al. 2014; Cody et al., 2016]. The second one is the angle between the longitudinal axis of the tibia and the antero-posterior axis of the talus [Zhou et al. 2014]. The third one is the angle between the antero-posterior axis of the talus and that of the calcaneus [Cody et al., 2016]. The last one is most commonly measured on the transversal plane, and it is the

angle between the longitudinal axis of the talus and the antero-posterior axis of the navicular [Carrara et al., 2020].

3.2.2. Transversal plane

In this anatomical plane the abduction of the forefoot and the valgus of the hindfoot can be observed thanks to several measurements. The most common ones are represented by the talo-calcaneal angle (Kite angle), the talo-1st metatarsal angle (anteroposterior Meary's angle), and the talo-navicular coverage angle. The Kite angle is the one between the longitudinal axis of the talus and that of the calcaneus and is used to assess heel valgus. Antero-posterior (AP) Meary's is the angle formed by the longitudinal axis of the talus and that of the 1st metatarsal bone, that are normally aligned. The talo-navicular coverage angle is between the lines perpendicular to the talar head and navicular bone articular surfaces and is useful for the evaluation of the lateral rotation of the navicular bone with respect to the talus bone (Figure 18).

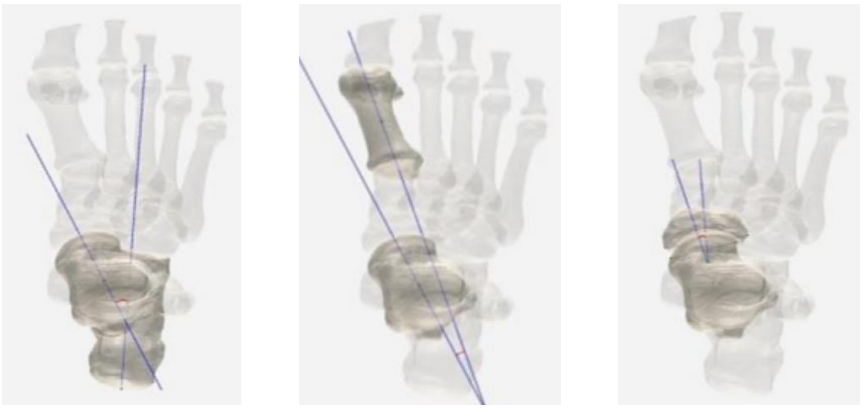

Figure 18 Some examples of angles in the transversal plane. The kite angle (left) between the AP axes of the talus and the calcaneus. The AP Mearys angle (centre) between the AP axes of the talus and the first metatarsus. The talonavicular coverage angle (right) between the AP axes of the talus and the navicular [Carrara et al., 2020]

In addition, other measurements can be observed most rarely in the literature, such as the angle between the longitudinal axis of the 1st metatarsal bone and that of the 2nd metatarsal bone or the angle between the longitudinal axis of the 2nd metatarsal bone and that of the calcaneus [Carrara et al., 2020, Cody et al., 2016]. In this anatomical plane, recently another innovative measurement has been assessed. It is called foot and ankle offset (FAO) and it was defined by Lintz and colleagues in 2017. This measurement has

the purpose of detecting the hindfoot alignment using the forefoot as reference. The first difference with the other measurements reported above is that FAO is measured starting from 3D foot models by WBCT that allow to observe the morphology and the relation between the bones under the physiological body weight, and without all the limitations of the traditional 2D X-rays images [Lintz et al., 2018]. FAO represents the lever arm created in the ankle from the combined actions of body weight and ground reaction force. The construction of this measurement starts from the identification of four specific points, A, B, C, D1 that are the most plantar aspect of the first metatarsal head, the fifth metatarsal head, the calcaneus and the talus, respectively. Once we have obtained these anatomical landmarks, the foot length can be calculated as the length of the line that joins C to the middle point (E) between A and B. D1 is the position of the centre of the talus, identified by its orthogonal projection (D) on the ABC plane. Then, the perpendicular line to CE, passing through D, is drawn so that F, the intersection point of these 2 lines, is found. Lastly, DF represents the desired offset that is given as a percentage of foot length CE, positive when D is medial with respect to F and negative when lateral (figure 19). The value of the offset is expressed as a percentage of foot length to make it independent on foot size and therefore comparable between feet of different sizes. In the above-reported paper, for the analysed cohort, mean value for FAO was 11.4% ± 5.7% in patients with valgus hindfoot alignment [Lintz et al., 2017]. Moreover, a recent study has found out a high correlation between this novel 3D measure and some traditional common measures and demonstrate a slightly higher reliability than traditional 2D measures [de Cesar Netto et al., 2020].

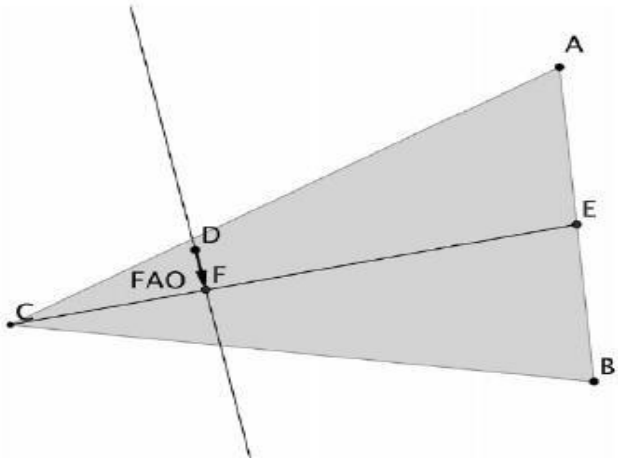

Figure 19 Representation of FAO. It represents the lever arm created in the ankle from the combined actions of body weight and ground reaction force and show the hindfoot alignment using the forefoot as reference. It is defined as the DF segment length [Lintz et al., 2017].

3.2.3. Frontal Plane

The frontal plane is useful to identify other peculiar characteristics of AAFD such as the hindfoot alignment or the forefoot arch flattening. It was demonstrated that patients with flatfoot deformity had more innate valgus in their talar anatomy and more valgus alignment of the subtalar joint than people with physiological feet [Cody et al., 2016].

- Hindfoot alignment

In severe cases of AAFD, valgus of the subtalar joint axis increases with a subsequent valgus of the hindfoot. Therefore, the hindfoot alignment is one of the main parameters to assess flatfoot deformity [Cody et al., 2016]. Notably, these authors define the hindfoot alignment as the angle between the longitudinal axes of tibia and calcaneus in the frontal plane, while Richter and colleagues define it as the angle between the principal axis of the tibia and the line that joins the centre of the talar dome and the posterior calcaneal process.

The gold standard to assess hindfoot alignment is the hindfoot arm, that was defined by Saltzman and El-Khoury in 1995, as the distance between the tibial axis and the most plantar aspect of the calcaneus. However, Williamson and colleagues define a more precise and reliable parameter to identify the valgus of the hindfoot in AAFD, called hindfoot alignment angle (HAA). This angle is comprised between the tibial principal axis and the calcaneal tuberosity axis, so taking into account only the posterior part of the calcaneus. The calcaneal tuberosity axis is built starting from the identification of four points: the most inferior-lateral point and the most superior-lateral point of the lateral part of the calcaneal tuberosity, and the most inferior-medial point and the most superior-medial point of the medial part of the calcaneal tuberosity. The line that joins the first two points is the line describing the lateral osseous contour (line B), while the line that joins the third and the fourth point is the line adapted to the medial osseous contour (line C). The transverse lines (lines D1 and D2) are drawn parallel and form equal angles (α) at the intersection points with lines B and C. Lastly, the calcaneal axis is defined as the bisector of these transverse lines (Figure 20).

This new way of calculating the hindfoot alignment results in relevant differences between measurements in flat feet and non-pathological ones. Moreover, it exploits a precise definition of the points used to define the calcaneal tuberosity axis, making this measurement useful in daily clinical practice [Williamson at al., 2015].

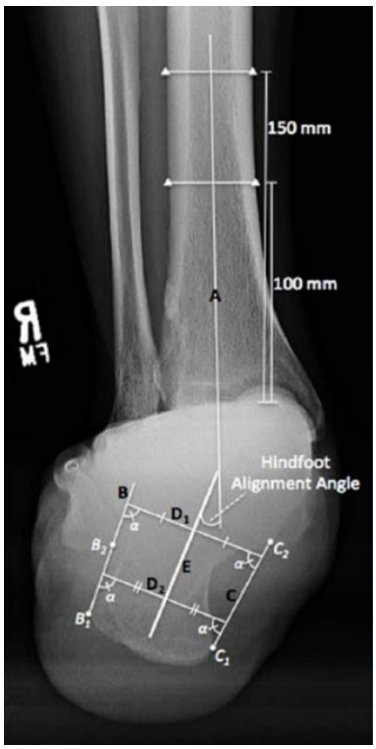

Figure 20 Representation of HAA. It is one of the most reliable measurement to assess the hindfoot alignment. It is defined as the angle formed between the longitudinal axes of the tibia and of the calcaneal tuberosity. [Williamson at al., 2015]

- Forefoot arch angle

This represents the angle between the transverse plane and a line drawn from the inferior aspect of the medial cuneiform to the inferior aspect of the fifth metatarsal. It constitutes a measurement of forefoot pronation or supination, but it also expresses the collapse of the MLA [Ferri et al., 2008].

3.3. Drawbacks of the above reported measurements

All these radiological measurements in literature have some limitations. 2D measurements from X-ray images are underestimated compared to 3D measurements [Shakoor et al., 2021]. For instance, the lateral talus-first metatarsal angle (Meary's angle) in weight-bearing CT images showed higher values than those obtained from weight-bearing radiographs. Probably, the value of that measurement may decrease during radiographic examination, owing to mispositioning of the lower extremity that leads to a slight foot

supination [Richter et al., 2014]. Moreover, the repeatability of X-rays images depends also on the operator, on the superposition of bone structures in the projections and on the rotational bias. On the other hand, traditional CT has the limitation of the acquisition without physiological load condition. This leads to a substantial change in the values of the measures. For instance, most of the 2D biometrics such as forefoot supination, the height of the medial arch and hindfoot valgus change substantially under physiological load. In particular, these measurements in pathological cases are often underestimated in absence of load [Hirschmann et al., 2013]. To overcome this problem, before the advent of CBCT, several studies tried to simulate the body weight in standard CT leading to an applied load that varied between 10 and 50 % of the physiological body weight, underestimating subluxation of the foot joints and changes of the joint alignment [Hirschmann et al., 2013]. The simulation of the load was carried out by using custom apparatus, giving more reliable results than the acquisitions without load. However, the different simulation apparatus could lead to a lack of repeatability between different studies [Kido et al., 2011; Ferri et al., 2008].

Therefore, in the last years, CBCT has been used to scan flat feet, since it provides 3D weight-bearing images, overcoming the limitations of both X-rays and standard CT imaging. In fact, CBCT is able to better represent the severity of osseous derangement in patients affected by this pathology, with respect to non-weight-bearing images [De Cesar Netto et al., 2017]. Consequently, given the shortcomings of both radiographs, including inaccuracies due to projections and foot orientation, and standard CT, including the absence of body weight, it can be concluded that WBCT provides considerable benefits in detecting proper angles for the assessment of complex 3D deformities such as AAFD.

Another step forward in the study of AAFD is the development of innovative measurements, taking advantages of CBCT technology. Thanks to this technology that provides 3D volumes of the foot skeletal architecture, it is possible to measure and compute 3D angles between foot bones, that correspond to the 2D angles from radiographs. These innovative 3D measurements can then be compared with the measures present in the literature, such as the Pitch angle, Williamson angle, Meary's angle, Moreau- Costa-Bertani. Moreover, the measurements describing the distances of the midfoot bones from the ground can be computed more precisely tracing the line that joins the centroid of the bones to the ground. The use of 3D measurements and their comparison with the traditional ones has just begun, showing good results in terms of correlation

between 2D and 3D. This was proved, for example, for the hindfoot alignment, and, as expected, 3D hindfoot alignment overcomes the disadvantages which affect 2D analysis [Burssens et al., 2016].

In the literature, however, the nomenclature used to express such measurements is very variable, so the need of common guidelines for describing them has progressively increased. In this context, the Weight Bearing CT Society (WBCT Society) built up a new terminology, meant to provide a single, unequivocal name to all possible measurements of the foot bone architecture [Leardini et al., 2019; Carrara et al., 2021].

As concerns this work, the angular measurements are the same of a previous study, developed in the research group at IRCCS Istituto Ortopedico Rizzoli. These are divided into absolute inclination of a single bone with respect to the ground (I) and relative orientation between two adjacent bones (R) [Ortolani et al., 2021]. All these measurements are then further divided in 3D measurements (3) or their planar projections into the three lateral (L), frontal (F) or transverse (T) anatomical planes, similarly to what traditionally accomplished in standard foot radiographs [Lamm et al., 2016]. Heights of a single bone with respect to the ground (Hg) are calculated as well. In the present work, the following bones are still considered: tibia (TI), calcaneus (CA), talus (TA), navicular (NA), cuboid (CU), medial cuneiform (CM), 1st and 2nd metatarsal (M1, M2) (Table 3).

1st letter ⇩ / 2nd letter ⇨	Lateral Plane (L)	Transverse Plane (T)	Frontal Plane (F)	3D (3)	Bone names
Single bone Inclinations (I)	IL_TI , IL_TA, IL_CA	IT_TA IT_CA		I3_CA I3_TA	Calcaneus (CA) Talus (TA) Tibia (TI) Cuboid (CU) Medial cuneiform (CM) First Metatarsus (M1) Second Metatarsus (M2)
Relative bone angles (R)	RL_TICA RL_TACA RL_TANA RL_CAM1 RL_TACAM1 RL_TAM1	RT_TICA RT_TACA RT_TANA RT_TAM1 RT_M1M2	RF_TICA RF_TACA RF_TANA	R3_TICA R3_TACA R3_TANA R3_CAM1 R3_TACAM1 R3_TAM1	
Heights from the ground (Hg)	Hg_NA, Hg_CU, Hg_CM				
Foot and Ankle Offset	FAO_%, FAO_mm				

Table 3 The way to build the nomenclature of this study

For instance, for any relative orientation, the distal with respect to the proximal bone is considered so that RL_TACA represents the angle between the calcaneus and the talus in the lateral plane projection, and R3_TACA is the corresponding 3D measurement.

RL_TAM1 is the angle between the 1st metatarsus and the talus in the lateral plane projection, i.e. the Meary's angle, and RL_CAM1 is the angle between the 1st metatarsus and the calcaneus in the lateral plane projection, i.e. the Hibb angle [Carrara et al., 2021].

For the sake of clarity, a parallelism between the traditional names of the 2D conventional radiographic measurements and the corresponding ones obtained in this work is outlined (Table 4).

NAME OF THE ANGLE	WBCT NOMENCLATURE
CALCANEAL PITCH ANGLE	IL_CA
TALOHORIZONTAL ANGLE	IL_TA
HIBB ANGLE	RL_CAM1
MEARY'S ANGLE	RL_TAM1
TALO-CALCANEAL DIVERGENCE	RL_TACA
TALO-NAVICULAR ANGLE	RL_TANA
MEDIAL LONGITUDINAL ARCH	RL_CATAM1
AP MEARY'S ANGLE	RT_TAM1
KITE ANGLE	RT_TACA
TALO-NAVICULAR COVERAGE ANGLE	RT_TANA
HINDFOOT ANGLE	RF_TICA
FIRST INTERMETATARSAL ANGLE	RT_M1M2

Table 4 Name of the angle found in literature and its analogous according to WBCT nomenclature

In conclusion, the DICOM files coming from CBCT device can be segmented and processed in order to compute all the 3D measurements along with the traditional 2D ones, by merely projecting the bones into the 3 anatomical planes. Moreover, the traditional 2D angles, as measured with this methodology, may be more precise because the artefacts due to the superposition of structures in the X-rays are here avoided. However, even if these 2D and 3D measures may be more repeatable, it is important to have control values to which refer them to and the possibility to carefully control patient foot positioning and loading condition during acquisition. For example, the measurements may be different if the patient is in double-leg or single-leg position [Leardini et al., 2019].

Chapter 4: Materials

In this chapter a brief description of all techniques and definitions, including relevant software tools, that are used in this study is reported. The segmentation software tools here are MIS (Mimics Innovation Suite) and DIS (Bonelogic® Ortho Foot and Ankle – Disior), state-of-the-art for respectively semi-automatic and full-automatic bone segmentation. Matlab is used then to assess the principal inertial components of the foot bones, to compute the measures, both those found in the literature and those novel 3D. Lastly the description of Geomagic tools is necessary, because this is used to save images representing the 3D foot models, and to qualitatively compare pre-op and post-op foot bone architecture.

4.1. Segmentation process

After an acquisition, DICOM format images are obtained. These are formed by a multiplicity of planar images one above the other. In the segmentation process, for each slice, the contour of any relevant bone has to be identified and tracked, i.e. segmented. At the end of this process the bone models are exported in standard stereo-lithography (STL) format. In this format, bones are represented as a huge number of points and triangles, forming the overall mesh of the external surface [Bucking et al., 2017]. The segmentation process is a long process which includes manual, semi-automatic or automatic recognition of bone contour, slice by slice and it is a crucial step in the analysis and in the practical use of biomedical imaging. Below some applications of STL files are described.

First, STL files can be directly 3D-printed, so that the surgeons can exploit the most realistic 1:1 scale model of the patient bones. Consequently, the printed model can be used to accurately plan the surgery or to enhance the communication between patients and surgeons [Leardini et al., 2019]. STL files can also be exported in a CAD modelling software, where a customized prosthesis can be designed accordingly to the real bone morphology and then 3D-printed. For instance, this procedure was applied in a study

where a patient underwent a total ankle replacement procedure: the prosthesis was designed directly to the patient bone and compared to a standard implant, highlighting the advantage of the former of saving more natural bone during its insertion [Durastanti et al., 2019A]. Lastly, STL files can be exported in Matlab, where bones anatomical relationships and angles can be computed easily and automatically, ensuring a high inter-operator repeatability [Carrara et al., 2020].

For the above-reported reasons, the segmentation process needs to be accurate and reliable. Therefore, it is necessary to choose the best segmentation tool in according to the purpose. There is a variety of different software: some of them are freeware, other very expensive, some are semiautomatic or completely automatic. Recently several studies dealt with the comparison between different software, showing the accuracy and the reliability of them [Matsiushevich et al., 2019; Virzì et al., 2020; Ortolani et al., 2021]. As concern this work, among all these software packages, MIS was chosen, because it represents the state-of-the-art semi-automatic segmentation tool.

4.2. MIS - Mimics Innovation suite

MIS is a semi-automated software for image segmentation, considered the most popular in clinical data processing according to the state-of-art [Byrne et al., 2016]. Its interface appears user friendly, with a clear division of the workflow in the upper part of the windows (file, view, segment, advanced segment, 3D tools, measure, align, my tab, help). The MIS window is divided into 4 views: sagittal, coronal, axial and the 3D volume rendering (Figure 21).

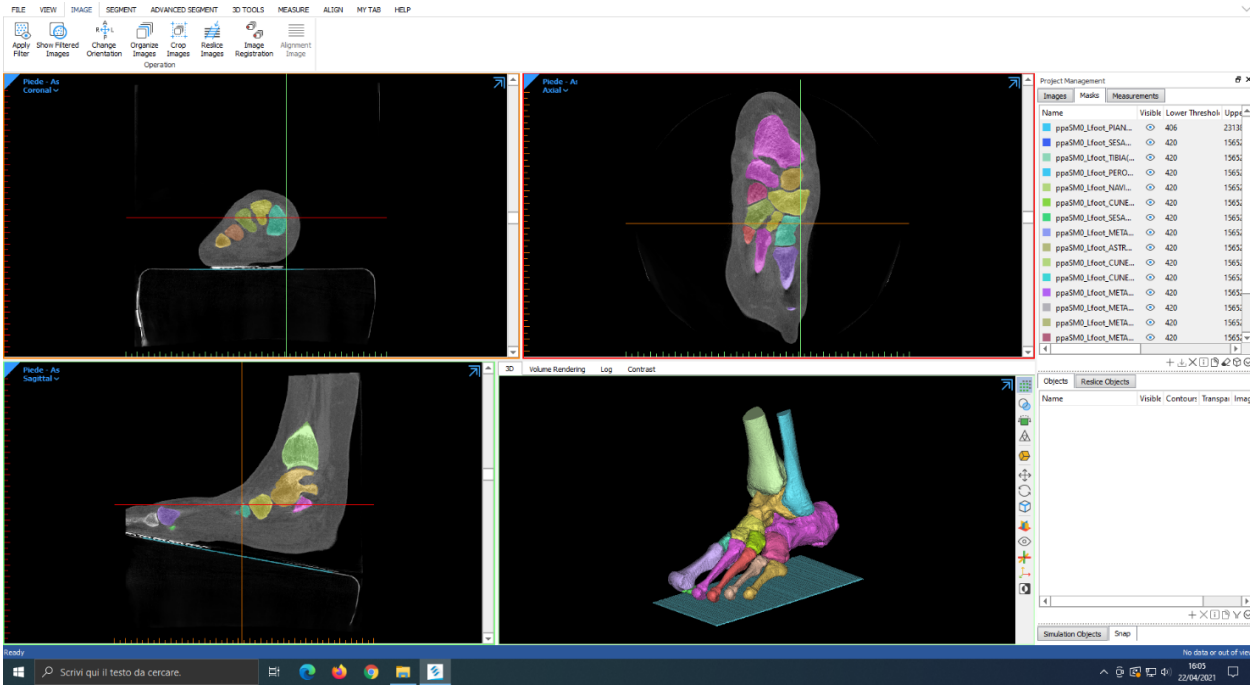

Figure 21 A snapshot from the Mimics interface. The bones are visible into three different anatomical planes (sagittal, frontal and transversal) and into a 3D volume rendering. On the right there is the list of the masks (one for each bone) that will be converted in STL files.

Firstly, a gaussian filter is applied to reduce considerably the noise of the imaging. Secondly a proper threshold corresponding to the Hounsfield Units (HU) is selected. This is a crucial step because the 3D foot volume is divided into internal and external regions on the basis of the values of the voxels: each voxel having a value below the threshold is assigned to the external material and each voxel whose value is greater than or equal to the threshold is assigned to the internal material. Hence, adjusting the threshold of the voxels wisely, we can obtain a preliminary 3D render of the foot. In this work, the threshold was adjusted according to the morphology and bone density of each foot: the minimum value is set at 400 HU, on average to discern the trabecular bone. The maximum of the HU range is left to the default value to capture the cortical bone and the ground plan of the cone beam device. With the command 'Region grow' single masks of each bone can be extracted from the entire foot mask. To do so, every foot bone must be isolated from the others, without having any voxel in common, and if it is not, the shared voxel needs to be manually eliminated. Once the single bone masks have been obtained, these have to be segmented one by one by using two principal commands: 'Edith mask' and 'Smart Fill'.

- Edit mask: it is used to remove noise from the 3D rendering view using the tool 'Lasso'. The latter allows to manually remove the voxels that do not belong to the examined bone, simply by tracking a contour around the voxels that should be eliminated.

In some cases, it is necessary to proceed in one of the 2D views layer by layer in order to remove more accurately all the rest of the noise with the tool ‘multiple scale edit’.

- Smart fill: Due to the presence of trabecular bones, usually the foot bones are not completely automatically recognized in the selection of the mask. With this command the contour of the bones, slice by slice, can be drawn manually with the local method. Once the boundaries of each bone have been tracked, with the global method, the internal trabecular bone is automatically filled.

At the end, when all the masks have been created and refined, the window should look like the screen capture shown above, with every bone mask represented by a different colour. Consequently, with the command ‘Calculate Part’ all the masks can be exported into STL models. There is also a 3D tools section, that allows to further smooth the 3D model. As concerns the present work, it was chosen to not perform any smoothing operation, since the external morphology of each bone segment is of fundamental importance for a correct anatomical characterization. To complete the whole 3D foot model the average time spent by the operator is about 12 hours.

4.3. Principal Component Analysis (PCA)

Once the segmentation process is over, the STL files are imported on Matlab. In this environment, bones anatomical frames and principal axes are computed, mostly using the Principal Component Analysis (PCA).

PCA technique is used to characterize other joint and musculoskeletal structures that can be adapted in the assessment of foot bones geometry and axes [Lenz a et al., 2021]. For instance, PCA was used by Belvedere and colleagues to assess diabetic foot deformity from CBCT imaging [Belvedere et al., 2020].

In this study PCA was used to define the geometrical axes of the bones and a global foot geometrical reference system. Moreover, an anatomical reference frame was given for each bone of the midfoot and of the hindfoot. These anatomical reference systems are not standardized; therefore, an original procedure was used [Carrara et al., 2021].

On Matlab, the 3D foot model is represented in the CBCT reference system which has no anatomical meaning. Hence, firstly, the foot is oriented in the global foot anatomical reference frame (footAF). This reference frame is in solidarity with the foot in order to avoid problems related to its orientation during the acquisition, i.e. inside the CBCT device. It is built up as follows; the segmented ground plane is taken as the transverse plane and the dorsi-plantar axis is defined as the one normal to the ground. The antero-posterior is the axis that connects the projection of the most plantar points of the calcaneus and of the second metatarsal head. The two axes compose the sagittal plane. The cross product of their unit vectors defines the medio-lateral axis. The origin of the system is located in the projection of the most plantar point of the calcaneus on the transverse plane [Carrara et al., 2020] (Figure 22).

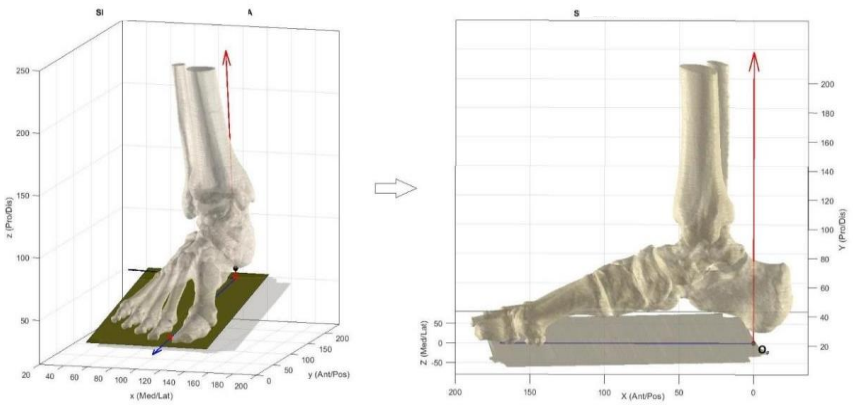

Figure 22 The CBCT reference system (left) vs the footAF (right). The former depends on the foot positioning in the CBCT machine, so it has not an anatomical meaning and it is different for each patient. The latter is defined starting from anatomical landmarks (the most plantar point of the calcaneus and of the first, second and fifth metatarsal bones) as reference, so, it is independent from the foot positioning in the machine. All the measurements will be defined in the footAF.

Once the footAF is established, PCA is used to define the anatomical reference frame of each bone. PCA is a statistical technique that uses 3D points coordinates, to define the 3 axes with the highest variance, i.e. those directions with the most or least spread of the surface points, under the constraint of their mutual orthogonality. It provides 3D axes of each bone respectively along their longitudinal direction (antero-posterior), their vertical direction (dorsi-plantar) and their medio-lateral direction. These are the orthogonal eigenvectors of the matrix of covariance of the vertex matrix, and these originate from the centroid of each segment, forming the technical reference frame [Carrara et al., 2021].

The STL files imported on Matlab appear as structures in many levels. These files are formed by triangles that describe the anatomical surfaces of the bones. The ‘vertex matrix’ is a [N x 3] matrix which contains the coordinates of the N vertices of the triangles and allows to represent the STL file as a cloud of points on which PCA can be applied (Figure 23).

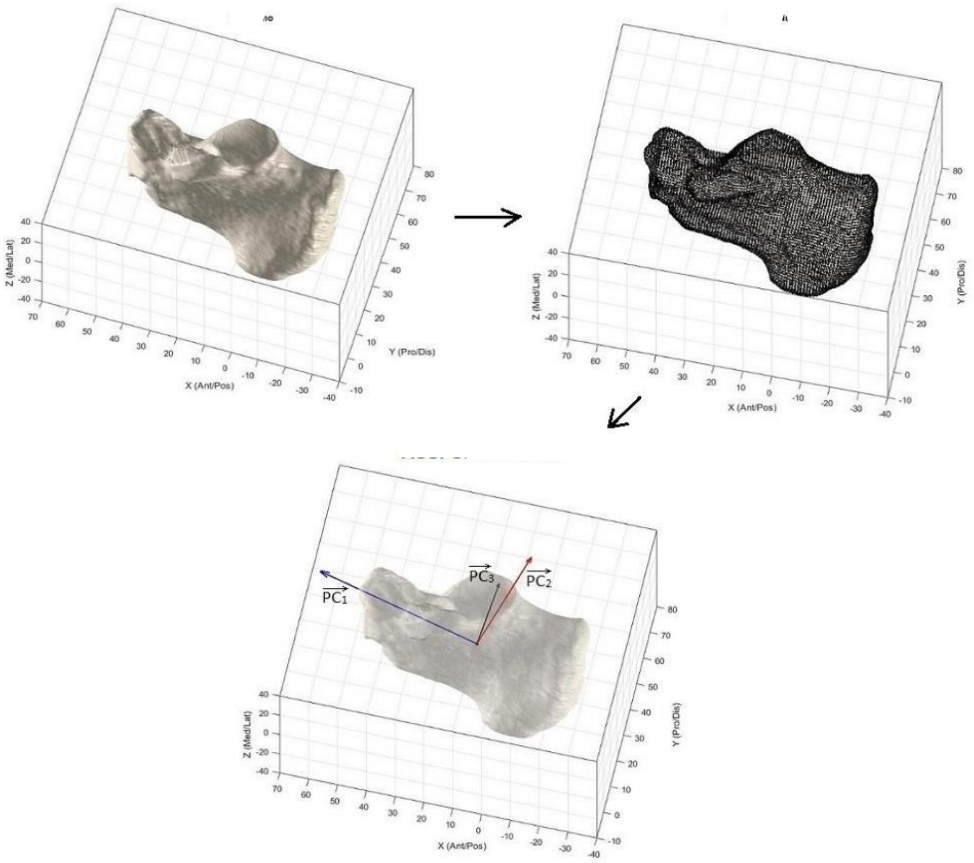

Figure 23 Application of PCA to define geometrical axes, in this case of the calcaneus. The figure shows the 3 main components that describe the external geometry, in blue (PC1), in red (PC2) and in black (PC3).

Bone axes can be used to calculate novel 3D measures, such as bone inclination with the respect to the ground, and relative 3D angles between bone segments. Moreover, anatomical axes can be projected in the three planes of the footAF (transversal, fontal and lateral) in order to obtain 2D measures, that are comparable with the ones present in literature [Carrara et al., 2020].

4.4. Pre-op and post-op qualitative comparison

Beside the angular measurements, the qualitative comparison between the morphology of the pre- and post-op models is carried out through the software Geomagic Control X (3D Systems, Rock Hill, USA). It is a 3D dimensional control software that allows to compare two different objects represented by STL files by means of Distance Map Analysis. Moreover, in this environment, the so-called test object can be overlapped to the reference one, and after a best-fitting procedure, Root Mean Square error is obtained.

Therefore, Geomagic control X is a useful tool, to assess the quality of the segmentation process, to compare foot morphology pre- and post-surgery and to help clinicians in the treatment planning. The 3D view of the object is easy to understand and helps in the communication between clinicians and patients. For these reasons pictures captured from this software are used to assess qualitatively the changes in the foot morphology. For example, a best-fit procedure was applied between the pre-op and the post-op calcaneus. In particular, the latter was moved, while the former remained in the same position. Once the best-fit was completed, the rotational matrix of the post-op calcaneus is recorded (Figure 24). So, while keeping the calcaneus as reference, the bones of the pre-op foot can be compared with the ones of the post-op. To do so the recorded rotational matrix can be applied to the post-op models.

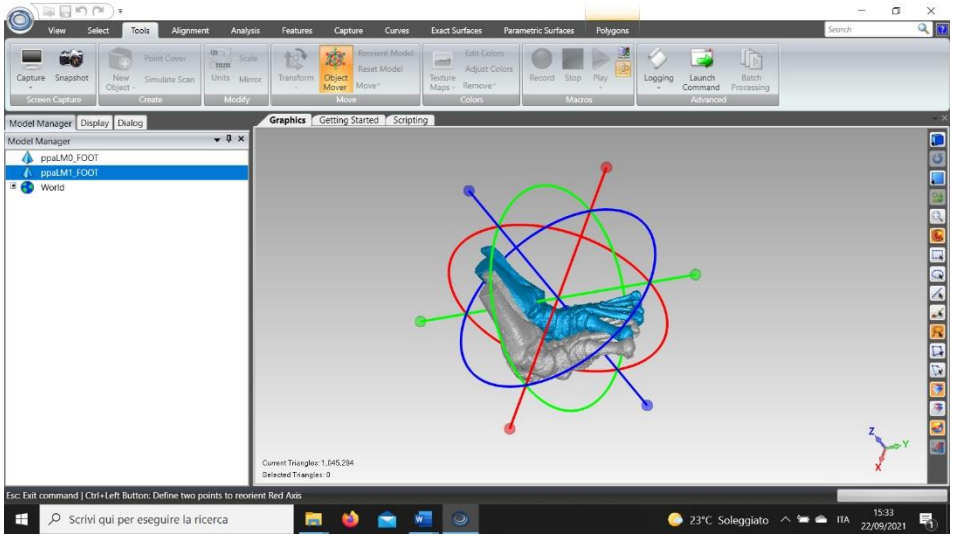

Figure 24 A snapshot from the Geomagic interface. This is the way the bones from pre-op and post-op foot scans are superimposed. The grey foot (pre-op) is the reference and remained fixed, while the blue foot is the test (post-op) and is moved on the former. Once they are approximately superimposed, the best fit function is applied, and the rotational matrix of the post-op foot is recorded.

Chapter 5: Methods

This chapter is necessary to comprehend the outcomes of the study. The workflow of the present measurements is described in detail, as well as the patient enrolment criteria, together with a description of all the measurements used in the observation of the outcomes of SAMBB procedure. At the end of the chapter the statistical analysis method is described

5.1. Workflow

The focus of this study is the investigation of a new procedure for quantifying the foot bones morphology and architecture. This method is applied in the case of severe flatfoot deformity, before and after their surgical treatment (SAMBB technique). This evaluation method follows a precise workflow. first, patients' feet were scanned through CBCT, pre- and post-operatively, in upright, single leg posture. Then, for each scan, virtual slicing of this 3D dataset produced 960 CT images at 0.26 mm distance, in DICOM format, i.e. the output file of the CBCT device. Acquisition time is about 25 seconds. After that, the three-dimensional rendering of the foot was built up in a few minutes for an initial check, by means of an automatic image processing. Due to the limited field of view, the machine allowed to scan just the feet of length equal or less than 22 cm. As a consequence, the metatarsal heads of some patients were not able to be acquired completely so they appeared severed in the whole 3D model of the foot resulting from the DICOM file bones segmentation. Consequently, DICOM files were converted into a STL file through the segmentation process. The tool used for segmentation was MIS. It is the state-of-art semiautomatic software, and requires about 12 hours, but it gives a more precise result [Ortolani et al., 2021]. Before proceeding in the geometrical evaluation of the foot architecture, intra-operator and inter-operator repeatability analysis of the segmentation process was performed. The former was estimated using the geometrical measurements of three pre-op scans, segmented by the same operator, after some weeks, three times. The

latter was obtained through the comparison of the same geometrical measurements obtained from three pre-op scans segmented by three different operators.

This evaluation was essential since the STL models used in this work were carried out by two different operators and were grouped together in order to increase the number of patients involved.

Once the repeatability analysis was ended, STL files were processed in different ways according to the purpose.

In the first approach they were imported in Matlab where bones principal axes were computed. These were obtained automatically in Matlab through PCA technique, making the computation of angles not operator dependent. Then, 39 geometrical measurements for each foot were collected, such as single bone inclination angles, relative angles, or distances from the ground. Some of these measurements were used to quantitatively compare pre-op, post-op and control values. Moreover, some of these are novel 3D measures that open the doors to more complex geometrical considerations, that avoid the superpositions of bone structures such as in traditional X-rays based imaging.

In the second approach STL files were imported in Geomagic where a qualitative comparison between pre- and post-op models took place. The image such obtained is a superposition of the 3D bone structures of pre- and post-op models, keeping the calcaneus of both feet at the same position, as a reference. Even if it is just a qualitative comparison, it was well appreciated by the surgeons, who could see how the relationships between the bones change after the surgery, and how the correction on the hindfoot could affect the morphology of the forefoot (Figure 25).

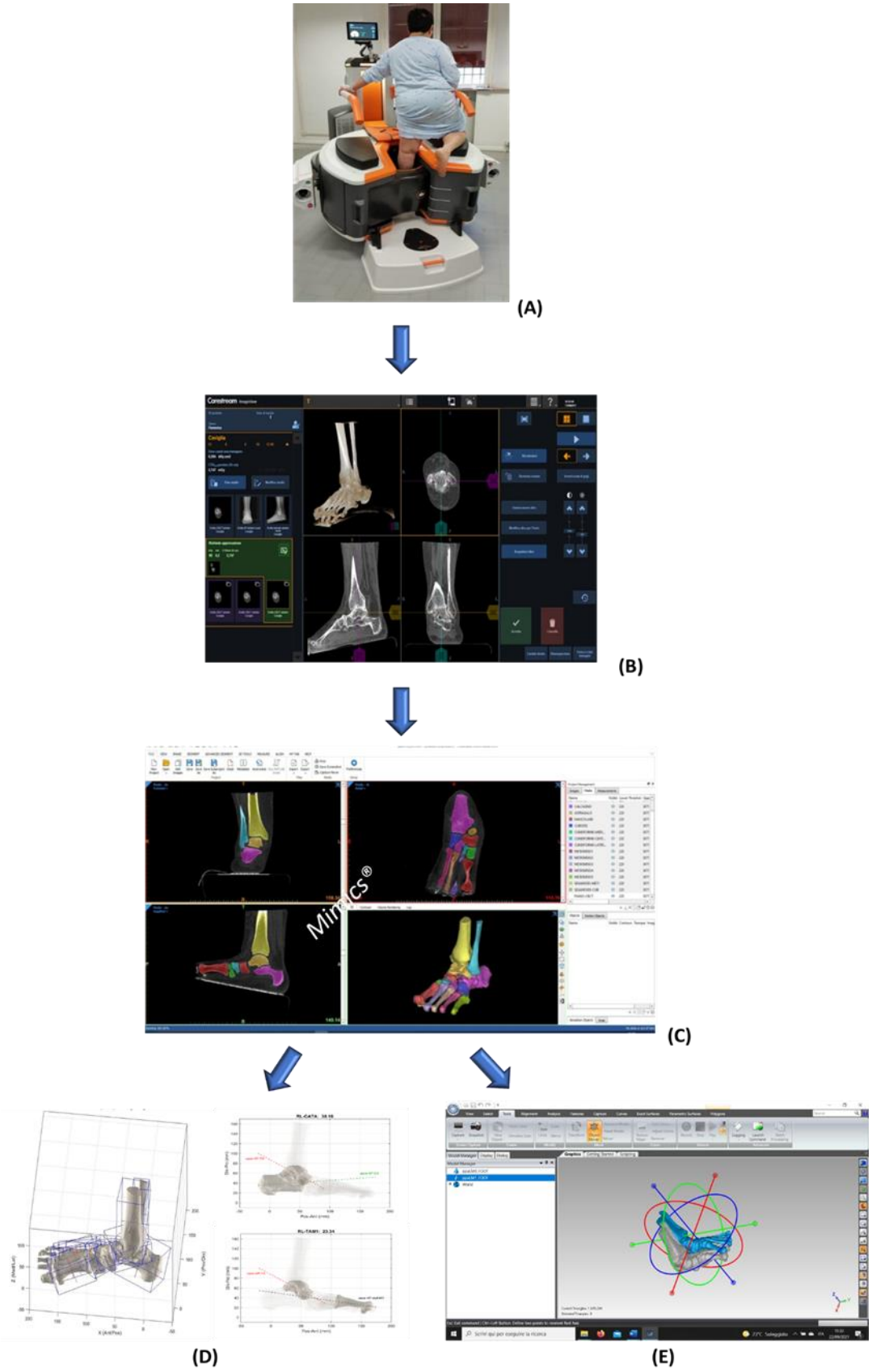

Figure 25 Workflow. Acquisition of the foot by CBCT (A), three-dimensional rendering of the foot bones built up by means of an automatic image processing (B), Segmentation of the foot bones on Mimics (C), Matlab elaboration of the STL file and automatic computation of morphological measurement (D), Geomagic elaboration of STL file to obtain the qualitative comparison between pre- and post-op feet (E)

5.2. A previous study

The present study is subsequent to a previous one where the analysis of 32 angular measurements between flatfoot bones axes were proposed. 21 patients, the same of this study, were scanned before the SAMBB surgical intervention. The measurements were obtained as reported in this study: the segmentation process and the application of the PCA on Matlab allowed to gain the principal axes of the bones. The aim was to compare the measurements obtained from the two state-of-the-art segmentation techniques, i.e. MIS and DIS (Bonelogic® Ortho Foot and Ankle, Disior, Finland), for the necessary 3D bone model reconstruction. Therefore, a statistical analysis was performed to identify statistically significant changes between MIS and DIS evaluations. The result was a very small significant difference between the two software for most of the 32 measurements with a linear correlation. MIS resembles more precisely the morphology of the bones, while DIS has the limitation of an unrealistic excess in surfaces smoothing. However, the dissimilarity in time consuming was evident, with a ratio of 1:10 of time expenditure between DIS and MIS. Hence, for a rapid assessment of the deformity DIS is a valid alternative to MIS, because of a substantial time saving. But, if the goal of the segmentation is an accurate surgery planification, or a prosthesis customization, MIS remains more reliable [Ortolani et al., 2021]. The second aim of the study was the assess of reliability of 3D and 2D measurements obtained through the anatomical axes of the bones found using the PCA in Matlab. The results showed a general higher consistency in 3D measurements compared with the traditional 2D angles from X-rays, pointing out the limitations related to the latter.

Therefore, given the more precise morphology of the bones of the MIS model and the reliability of PCA measurements, in this study, this procedure was applied on the post-op scans of the same patients, evaluating if this method can assess the modifications in foot architecture after the surgery.

5.3. Enrolment of patients

21 patients (9 male / 12 female, 50.9±13.6 years old, 79.5±16.2 Kg weight, 170.3±11.9 cm height, 142 27.3± 4.0 BMI) with indication for the SAMBB were enrolled in this study.

Inclusion criteria were:

- patients with idiopathic flatfoot, with indications for a corrective arthrodesis of the subtalar joint;

- patients with an age between 18 and 65;

- patients with BMI under 40;

-patients who signed the informed consent.

Exclusion criteria were:

- patients with serious morpho-structural alteration or other pathology of the foot and of the inferior limbs;

- patients with serious systemic or cardiovascular diseases;

- patients with BMI over 40, so only large obese were excluded, with the consequence of a great variability in BMI of the treated patients from 20.1 to 32.1.

Concerning this study, in order to have a uniform dataset, just 10 patients were considered. All these patients underwent only the SAMBB procedure, so people that underwent more surgeries were excluded in the comparison between pre- and post-op.

Moreover, other two diagnostic clinical tools were introduced to characterize each patient: the Foot Posture Index (FPI) and the Foot Function Index (FFI).

FPI is an outcome measure developed about fifteen years ago and it is used to quantify quickly and precisely the variation in the orientation of the foot in a clinical setting, focusing on the pronation or on the supination of the foot. This index takes in consideration the forefoot, the midfoot and the rearfoot in the three body planes (sagittal, transverse and coronal). In particular, the clinician has to observe six morphological criteria of the foot and assign to them a score from -2 to +2. All observations are made with the subject standing in double leg support and in static stance position.

The criteria include:

1- Talar head palpation;
2- Curves above and below lateral malleoli;

3- Inversion and eversion of the calcaneus;
4- Prominence in the region of the Talonavicular joint;
5- Congruence of the medial longitudinal arch;
6- Abduction and adduction of the forefoot on the rear foot.

The lower the score (-2 is the minimum), the more supinated is the foot, while the higher the score (+2 is the maximum), the more pronated is the foot. Obviously, a 0 scoring means a neutral position, i.e. a physiological foot. Once all the scores were collected, these were summed up, giving a final score that goes from -12 to +12 [Keenan et al., 2006]. For all the patients in the study, in the pre-op, FPI was collected, showing positive scores (i.e., pronated foot), consistently with the needing of the surgical intervention.

The Foot Function Index (FFI) was originally thought to assess functional ability and pain in patients with rheumatoid arthritis and foot pathologies. FFI comprises 23 criteria divided into three subscales: disability, pain, activity limitation. For each criterion, the patient was required to assign a score from 0 (no pain) to 10 (worst possible pain or limitation). The sum of all these items gave the total score (calculated as a percentage of the maximum score achievable) describing the condition of the patient [Martinelli et al., 2014].

The FFI and the FPI were administered the day before surgery and during the follow-up visit to all patients (Table 5).

PATIENTS	GENDER	AGE (YEARS)	BMI	FPI PRE-OP	FFI PRE-OP [%]
AC	F	52.3	27.9	12.0	52.4
BA	M	31.8	23.0	6.0	67.1
CP	F	56.3	20.5	12.0	84.7
DER	M	59.7	31.0	12.0	18.2
DN	M	75.0	32.0	12.0	67.7
LM	F	43.9	26.9	8.0	57.1
MM	F	54.2	34.4	12.0	34.7
SM	F	52.3	27.1	8.0	79.4
TV	M	31.8	29.6	12.0	76.5
VL	F	56.3	28.4	10.0	69.4

Table 5 list of the 10 patients operated only with SAMBB procedure and their pre-op FPI *and FFI scores.* Positive values for FPI indicate pronated foot, 12 is the maximum. Higher value of FFI indicates higher *disability*, *pain* and *activity limitation*

5.4. Measurements on the foot

After segmentation, the obtained STL files, containing bone segments and CBCT ground were imported in Matlab (Mathworks Inc., Natick, MA, USA). In this environment, an algorithm based on PCA and implemented in Matlab was used to perform all the necessary geometrical characterization of the bones, including anatomical reference systems and anatomical axes [Carrara et al., 2021]. PCA was chosen because it is a fully automatic technique, not affected by the operator or by the foot positioning during CBCT.

Firstly, a global foot anatomical reference frame was defined, the footAF. The antero-posterior axis is the line joining the projections on the ground of the most plantar point of the calcaneus and of the second metatarsal head, the vertical axis is the normal to the ground and the medio-lateral axis is the cross product of the last two. In this way, the bias due to the foot positioning during the acquisition was eliminated.

Then, PCA technique was performed to obtain the anatomical reference system for each bone, formed by the highest variance axes. These represent the longitudinal, medio-lateral and dorsi-plantar anatomical axes, identified automatically. These axes characterizing each single bone ultimately represented 3D axes in the foot anatomical frame which were also projected onto the lateral, frontal and transverse anatomical planes of the Foot reference system (FootAF), in order to make all the following calculations possible (Figure 26).

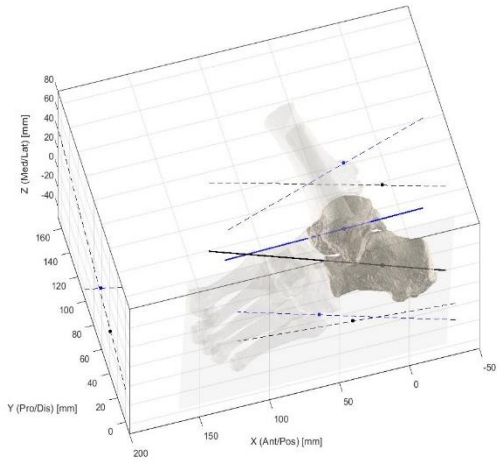

Figure 26 Relative angle between calcaneus and talus. As described above, the angle is computed between the 3D antero-posterior axes of the two bones: these are here also projected into the three anatomical planes: transverse, lateral and coronal.

The same procedure was performed on 10 post-op patients, allowing for a quantitative comparison of the geometrical outcomes with the pre-op feet. Also, the values of FPI and

FFI, resulting in lower values, were used to assess the healing of the foot. For planar angles, the longitudinal axis of each bone, obtained through PCA, was projected into the three anatomical planes of the footAF. For each segment, the inclination of the axis with the respect of the ground was obtained and identified by the letter "I". Consequently, also the relative inclination between two bones was considered and identify by the letter "R". These 2D data most resemble the state-of-art X-ray based angular measurements [Lamm et al., 2016; Carrara et al., 2021]. Thus, inclinations (I) of single bones, i.e. absolute angles, and bones mutual orientation, i.e. relative angles, were computed in the lateral (L), in the transverse (T) and in frontal (F) anatomical planes so that the following measurements were obtained:

- IL_TI: angle between the proximal-distal axis of the tibia and the ground plane;
- IL_TA: angle between the anterior-posterior axis of the talus and the ground plane;
- IL_CA: angle between the anterior-posterior axis of the calcaneus and the ground plane;
- IL_M1: angle between the anterior-posterior axis of the diaphysis of the first metatarsal and the ground plane;
- IT_NA: angle between the anterior-posterior axis of the navicular and the ground plane;
- IT_TA: angle between the anterior-posterior axis of the talus and the anatomical anterior-posterior axis (Figure 27);
- IT_CA: angle between the anterior-posterior axis of the calcaneus and the anatomical anterior-posterior axis.

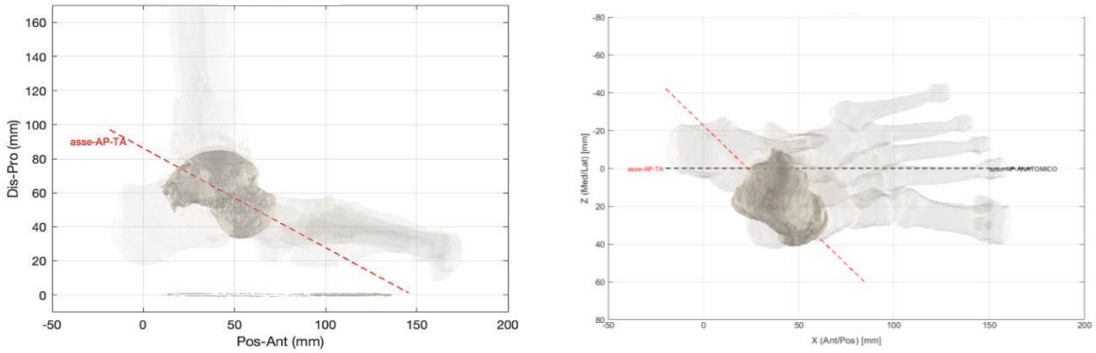

Figure 27 Example of Absolute inclination of the talus AP axis in the lateral view (left) and in the transversal view (right). The former is called IL_TA and the second is called IT_TA using the nomenclature proposed by Ortolani and colleagues [Ortolani et al., 2021].

Consequently, sign conventions for these measurements were chosen:
- In the lateral view (L), plantar-flexion movements were indicated by a positive sign (+), whereas dorsi-flexion ones were indicated by a negative sign (-);
- In the transverse view (T), intra-rotation movements were indicated by a positive sign (+), while extra-rotational movements were indicated by a negative sign (-).

- RL_TICA, RF_TICA, RT_TICA: relative angle between the proximal-distal axis of the tibia and the anterior-posterior axis of the calcaneus, projected onto the three anatomical planes;
- RL_TACA, RF_TACA, RT_TACA: relative angle between the anterior-posterior axis of the talus and that of the calcaneus, projected onto the three anatomical planes;
- RL_CAM1: relative angle between the anterior-posterior axis of the calcaneus and that of the diaphysis of the first metatarsus, in the lateral view;
- RL_TAM1, RT_TAM1: relative angle between the anterior-posterior axis of the talus and that of the diaphysis of the first metatarsus, both in the lateral and transverse view (Figure 28);

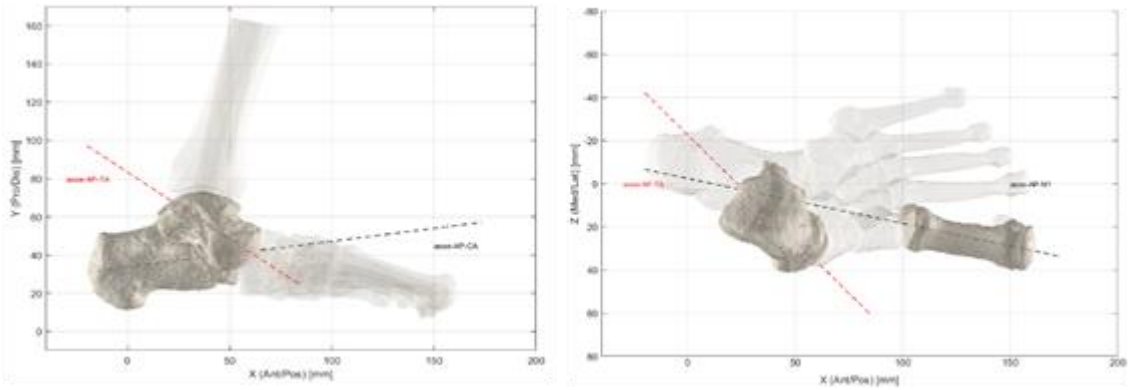

Figure 28 Example of two relative angles. On the left, RL_TACA on the lateral view, that is the angle between the AP axes of the calcaneus and of the talus. On the right, RT_TAM1 on the transversal view, which is the angle between the AP axes of the talus and of the first metatarsus. RT_TAM1 is found in the literature as the AP Mearys angle.

-RT_M1M2: relative angle between the anterior-posterior axis of the diaphysis of the first metatarsus and that of the diaphysis of the second one, in the transverse view.
- RL_TANA, RF_TANA, RT_TANA: relative angle between the anterior-posterior axis of the talus and that of the navicular. In particular, the third one is equivalent to the talo-

navicular coverage angle, very useful for the assessment of forefoot abduction, representing the degree of shift of the navicular on the talus.

For such relative angles, a negative sign (-) was attributed to an extra-rotation movement or a dorsiflexion movement of the second bone appearing in the name of the angle (according to WBCT nomenclature) with respect to the first bone mentioned; on the other hand, a positive sign (+) was used for indicating an intra-rotation movement or a plantarflexion movement of the second bone with respect to the first one.

- RL_CATAM1: This measure represents the Medial Longitudinal Arch (MLA) according to Moreau-Costa Bertani. The collapse of the MLA, in fact, is one of the three principal geometric deformation that characterize the flatfoot deformity, along with hindfoot valgus and forefoot abduction. It was measured by connecting three points: the most plantar point of the calcaneus to that of the talar head and the latter to the inferior point of the first metatarsal head. Another indicator of the same measurement is RL_CAM1 (Figure 29).

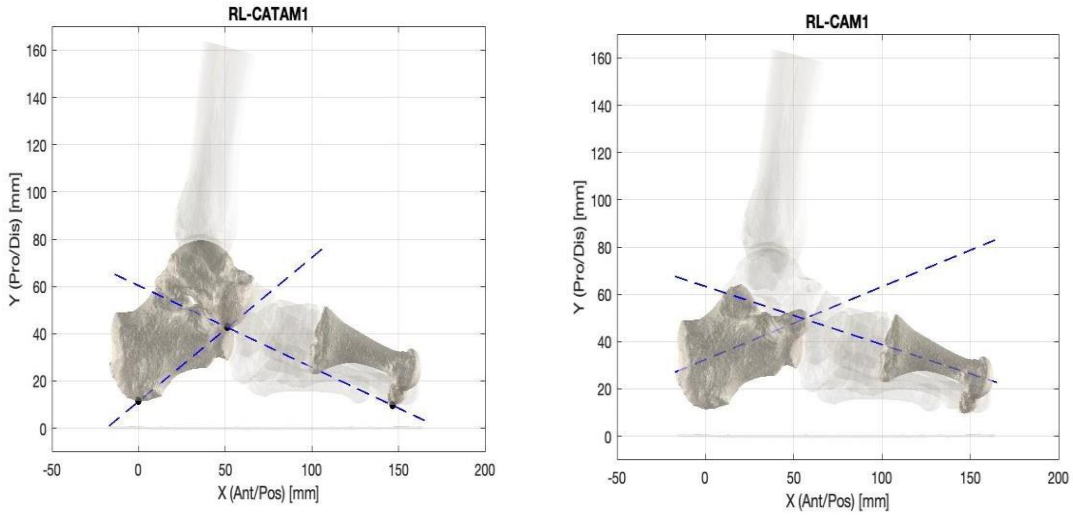

Figure 29 RL_CATAM1 and RL_CAM1, two possible representations of the MLA. The former is called in the literature as the Moreau- Costa-Bertani angle, the latter as the Hibbs angle. These angles are essential to identify the expected elevation of the MLA after operation.

-The hindfoot valgus, to date, is assessed by the Hindfoot Alignment Angle, by Williamson, collected from X-ray imaging [Williamson at al., 2015]. This measure was called HAA_Will in this study and it was obtained following the definition of Williamson. Firstly, the calcaneus was projected onto the frontal plane and only this planar projection

was considered. The frontal plan was then divided into 2 different regions, one containing the upper part of the calcaneus and the other the lower one. For each part, the most medial and the most lateral points were collected. Consequently, the two lines connecting the two medial points and the two lateral ones were found and the bisector of that angle was determined. The bisector was called calcaneal tuberosity axis, and, the angle formed by this axis and the longitudinal axis of the tibial shaft corresponded to the hindfoot alignment angle (Figure 30). In order to improve this definition of Hindfoot alignment, and, given the 3D model of the calcaneus, another parameter was defined. It was called HAA_Tub and it was obtained considering the tuberosity of the calcaneus, corresponding to 15% of its whole length. Then, PCA was applied to this portion to find the calcaneal tuberosity axis as the one of highest variance. Finally, the intersection between the calcaneus tuberosity axis and the longitudinal axis of the tibial shaft identified the hindfoot angle.
The hindfoot valgus was highlighted also by the relative angle RF_TICA, explained above.

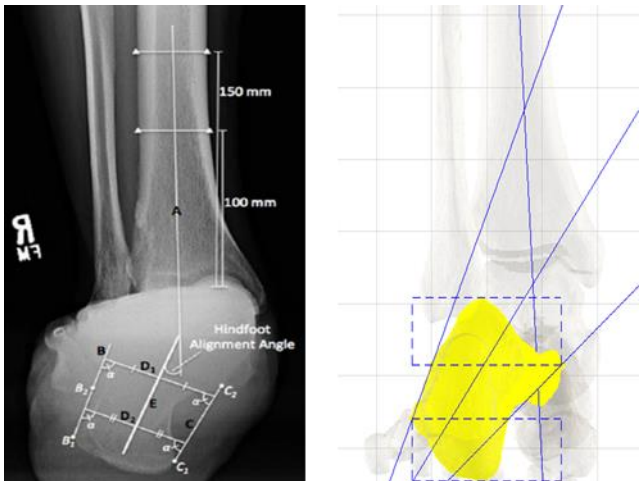

Figure 30 Comparison between the HAA_Will from the literature and the one from Matlab. The planar projection of the calcaneus on the frontal plane is considered. This is divided into 2 different regions, one containing the upper part of the calcaneus and the other the lower one. For each part, the most medial and the most lateral points are collected. Consequently, the two lines connecting the two medial points and the two lateral ones are found and the bisector of that angle is determined. This is the calcaneal tuberosity axis that form the angle with the longitudinal axis of the tibia.

Moreover, in planar views, according with literature, the heights of the midfoot bones from the ground were performed. These distances were computed between the ground and the most plantar point of navicular, cuboid, and medial cuneiform bones such as in literature [Gwani et al., 2017, Shakoor et al., 2021]. In addition, these distances were also computed

from the centroid of the bone. It was possible due to the disposal of 3D models of the bones from CBCT.

- Hg_NA_c, Hg_CU_c, Hg_CM_c: heights, with respect to the ground, of the centroid (c) of the navicular bone, cuboid and medial cuneiform, respectively;
- Hg_NA, Hg_CU, Hg_CM: heights, with respect to the ground, of the most plantar aspect of the navicular bone, cuboid and medial cuneiform, respectively (Figure 31).

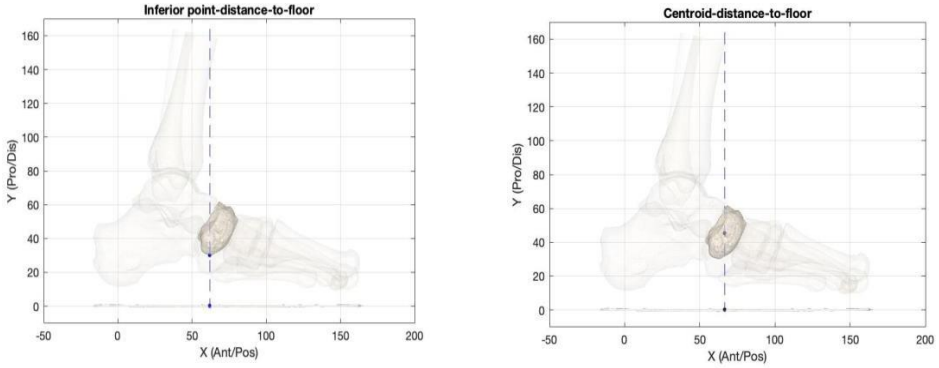

Figure 31 Hg_NA, measured both as the distance between the lowest point of the navicular and the ground (left) and as the distance between the centroid of the navicular and the ground (right).

The last 2D measurements are the Foot and Ankle Offset FAO [%], FAO [mm]. This parameter was proposed by Lintz to relate the hindfoot valgus to the forefoot position. So, it aimed to be a more successful measure of hindfoot alignment than the other HAA previously described. Its measurement was performed by collecting the 3D coordinates of specific anatomical landmarks: the lowest point on the surfaces of the first and fifth metatarsals heads of the calcaneus and the centre of the ankle joint. First, the midpoint of the line connecting the most plantar aspects of the two metatarsals heads was marked. Secondly, the foot length was defined and drawn as the line connecting this point to the point of the calcaneus. Then, the centre of the ankle was projected onto the ground plane and the line passing through this point and perpendicular to the foot length was tracked. Finally, the distance between the obtained intersection point and the projection of the centre of the talus represented the offset (FAO) (Figure 32). FAO [%] was the value of that offset expressed as the percentage of the entire foot length in order to make it independent on the foot size. On the other hand, FAO [mm] was the actual distance measured in millimetres.

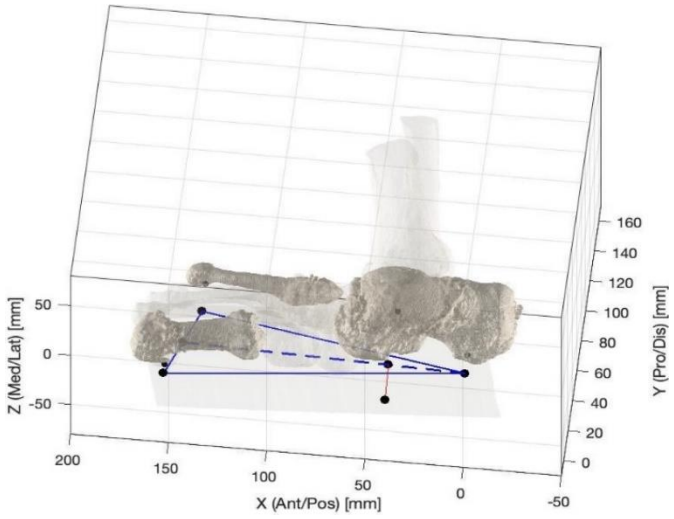

Figure 32 Construction of FAO (red line) in Matlab environment. It starts from the identification of four specific points: the most plantar aspect of the first metatarsal head, the fifth metatarsal head, the calcaneus, and the talus. The foot length can be calculated as the length of the line that joins the most plantar point of the calcaneus to the middle point between the most plantar points of the first and the fifth metatarsi. Then, the perpendicular line to the foot length, passing through the projection on the transversal plane of the most plantar talus point is drawn. This distance represents the desired offset that is given as a percentage of foot length.

Most of the planar metrics described above find some correspondence in literature, concerning the AAFD. In fact, traditionally, these geometric parameters were outlined on 2D X-ray imaging. However, the X-ray imaging tracking has some limitation. Firstly, the finding of landmarks and anatomical axes are operator dependent. Secondly, The X-ray imaging represents all the bone structure projections overlapped, so the identification of bones could present some artifacts. In this study, the first limit was overcome by the use of an automatic algorithm that defines the axes through an automatic process, involving PCA. The second limitation did not exist anymore, because the projection onto the anatomical planes came from each single 3D bone model separately from the others.

The greatest innovation of CBCT is the possibility to obtain 3D absolute and relative angles. It is possible considering the 3D anteroposterior axes of each bone, that can be used to assessed relative angles i.e. between two different segment and absolute angles i.e. the inclination angle of the bone with the respect of the ground.

- I3_TA: 3D angle between the anterior-posterior axis of the talus and the ground;
- I3_CA: 3D angle between the anterior-posterior axis of the calcaneus and the ground;
- R3_TICA: 3D angle between the proximal-distal axis of the tibia and the anterior-posterior axis of the calcaneus;
- R3_TACA: 3D angle between the anterior-posterior axis of the talus and that of the calcaneus;
- R3_CAM1: 3D angle between the anterior-posterior axis of the calcaneus and that of the diaphysis of the first metatarsal;
- R3_TAM1: 3D angle between the anterior-posterior axis of the talus and that of the diaphysis of the first metatarsal;
- R3_TANA: 3D angle between the anterior-posterior axis of the talus and that of the navicular;
- R3_CATAM1: 3D angle representing the MLA, calculated similarly to its projection onto the lateral plane (RL_CATAM1), as showed.

5.5. Repeatability Analysis

Intraclass Correlation Coefficient (ICC) is an index that reflects both the degree of correlation and the agreement between repeated measurements. ICC has not a standard value for admissible repeatability. In the literature, an ICC value smaller than 0.5 indicates poor repeatability, values between 0.5 and 0.75 indicate moderate repeatability, values between 0.75 and 0.9 indicate good repeatability, and values greater than 0.90 indicate excellent repeatability. Nevertheless, a low ICC could not only reflect the low degree of repeatability, because it can be affected by the small number of operators or measurements repetitions [Koo and Li, 2016]. In addition, ICC index is not unique, but different methods exist. These are distinguished by the model, the definition, and the type (Table 6).

ICC Methods
One-way random effects, absolute agreement, single rater/measurement
Two-way random effects, consistency, single rater/measurement
Two-way random effects, absolute agreement, single rater/measurement
Two-way mixed effects, consistency, single rater/measurement
Two-way mixed effects, absolute agreement, single rater/measurement
One-way random effects, absolute agreement, multiple raters/ measurements
Two-way random effects, consistency, multiple raters/measurements
Two-way random effects, absolute agreement, multiple raters/ measurements
Two-way mixed effects, consistency, multiple raters/measurements
Two-way mixed effects, absolute agreement, multiple raters/measurements

Table 6 ICC methods list, in according with Koo and Li, 2016.

- The model can be *one-way random effect*, *two-way random effect*, or *two-way mixed effects*. The former is used when the operators are randomly chosen from the entire population of possible operators, the latter when the operators are chosen randomly from a population with similar characteristics, the third one when the result is not generalizable to different classes of population, but only to the operator one.
- The definition can be *"consistency"* or *"absolute agreement"*. The former concerns the degree to which the measurement of the first operator can be equated to the measurement of a second one plus a systematic error, the latter is more restrictive, and it is used when the measurements are equal.
- The type can be *single operator* or *multiple operators* in according with the repeatability analysis purpose.

In this study, the ICC method was chosen following the scheme below (Figure 33).

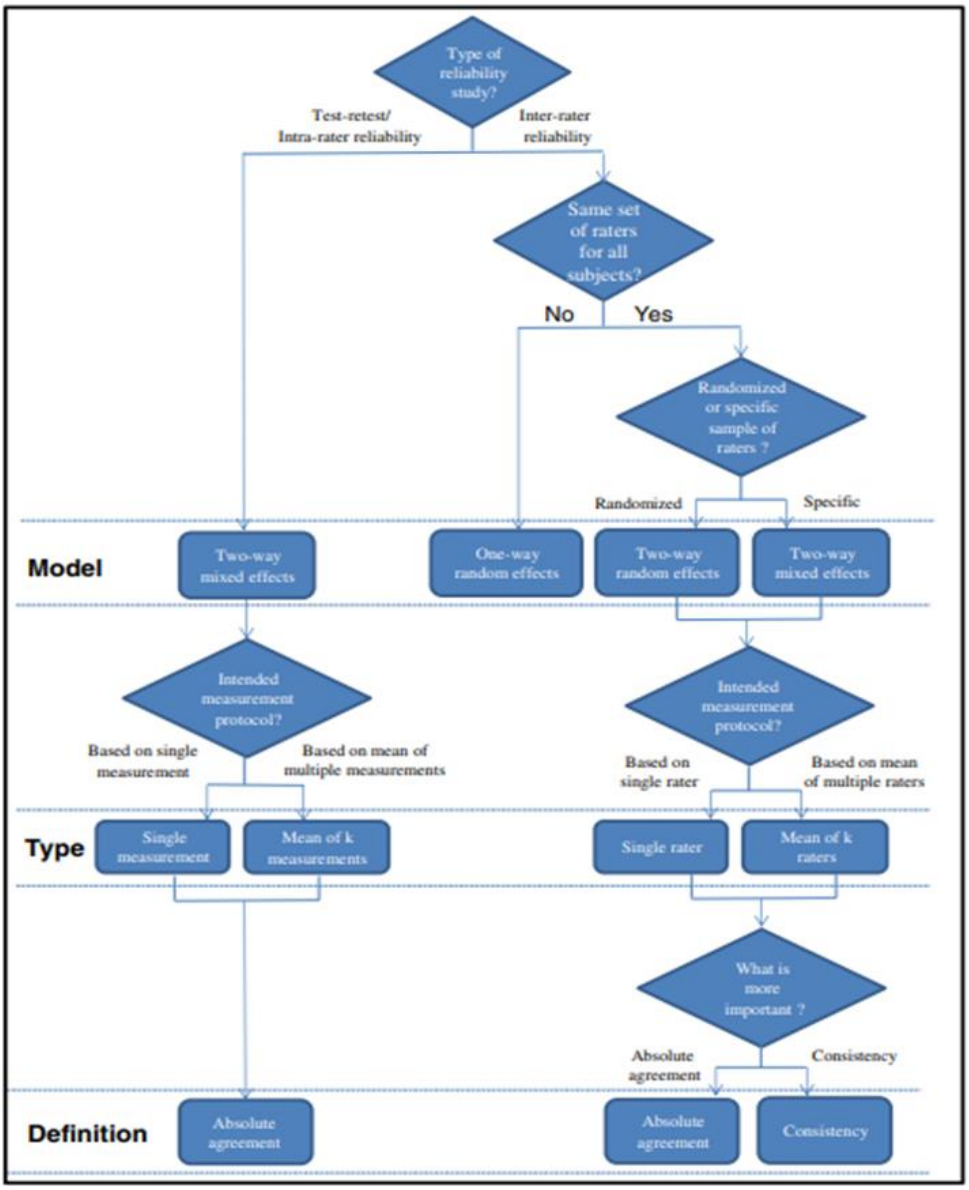

Figure 33 This flowchart explains the way a researcher should choose the best ICC in his repeatability study. The selection of the correct ICC form can be guided by 4 questions: The first 2 questions guide the "Model" selection, question 3 guides the "Type" selection, and the last question guides the "Definition" selection [Koo and Li, 2016].

For the inter-operator repeatability, the two-way random effects, consistency, multiple operators ICC was used, while for the intra-operator repeatability the two-way mixed effects, absolute agreement, single operator ICC was used [Koo and Li, 2016]. Finally, the intra-operator repeatability was applied on 39 measurements of the foot bones. These were computed on three different scans, each of them segmented three times by the same operator at a time distance of five weeks. The ICC was computed for each measurement on a n x m matrix, where n indicates the three different scans and m represents the three different repetitions (Figure 34).

	Rep.1	Rep.2	Rep.3
Foot 1	2.8	3.1	3.6
Foot 2	22.3	22.7	22.6
Foot 3	12.4	12.6	12.8

Figure 34 Matrix example. It is the n x m matrix of the first measurement (IL_TI). This layout of matrix is used for computing the ICC of every measurement. The rows represent the three different feet, while the columns are the three different repetitions (here abbreviated with Rep.).

All the measurements obtained were used to assess the inter-operator repeatability. These were computed on three different scans, each of them segmented by three different operators. The ICC was computed for each measurement on a n x m matrix, where n are the three different scans and m are the three operators (Figure 35).

	OP.1	OP.2	OP.3
Foot 1	3.1°	3.1°	3.3°
Foot 2	22.6°	22.6°	22.7°
Foot 3	12.8°	12.5°	12.7°

Figure 35 Matrix example. It is the n x m matrix of the first measurement (IL_TI). This layout of matrix is used for computing the ICC of every measurement. The rows represent the three different feet, while the columns are the three different operators (here abbreviated with Op.).

5.6. Statistical analysis

Statistical analysis about the differences between pre-op and post-op measurements was performed in the Matlab environment. All the differences pre-post for each measurement and each patient were first checked for normal data distribution by applying the Shapiro-Wilk test. Accordingly, where the distribution of the data was found to be normal, Student's paired-t test was used for comparison between pre-op and post-op values; otherwise, Wilcoxon rank-sum tests was applied. Tests were applied to understand whether the differences between the data pre-op and post-op were statistically significant, making this procedure robust for the evaluation of a foot deformity improvement. T-test and Wilcoxon Rank Sum test p-values were taken into account for the assessment of significance in terms of differences. Among all the p-values, those of less than 5 percent ($p < 0.05$) were considered statistically significant.

Furthermore, a linear regression model was applied on pre-post differences of the geometrical measurements and the clinical indices FPI and FFI, in order to derive correlations by means of the Pearson product-moment correlation coefficient (r) and its squared form (r^2), i.e. the determination coefficient. Corresponding p-values were taken into account for the assessment of significance in terms of differences and correlations. As far as the latter is concerned, among all the p-values, those of less than 5 percent ($p < 0.05$) were considered statistically significant and therefore accepted.

Chapter 6: Results

In this chapter, the results obtained from the application of the above-explained procedures on the acquired subjects will be illustrated and discussed. As stated in the introduction, the aim of the present work is two-fold: on the one hand, investigating the intra- and inter-operator repeatability of the segmentation process; on the other hand, providing a 3D characterization of the architecture of the foot and ankle under load, stating its value for both planning and evaluating the treatments for pes planus deformity corrections (in this case, the SAMBB technique will be considered). The outcomes of the surgical technique introduced in the present study will be shown, and an evaluation will be given by means of 10 patients analyzed.

6.1. Repeatability Analysis

6.1.1. Intra-operator repeatability

Intra-operator repeatability was applied on 39 measurements. These were computed on three different pre-op scans, that are identified by the initials BA0, TV0 and SM0, each one segmented three times at a time distance of five weeks by the same operator. All the measurements for BA0 are reported below (table 7). Just the measurements for one scan were reported since all of them have similar data variability between the repetitions.

	Repetition 1	Repetition 2	Repetition 3	Average	sd	$\left\|\frac{sd}{Average}\right\| * 100$
IL_TI [°]	2.8	3.1	3.6	3.2	0.4	12.2 %
IL_TA [°]	22.7	22.3	22.3	22.4	0.2	0.9 %
IL_M1 [°]	16.9	17.3	17.5	17.2	0.3	1.7 %
IL_CA [°]	-12.2	-12.5	-12.3	-12.3	0.2	1.6 %
IT_TA [°]	26.2	22.3	27.5	25.3	2.7	10.7 %
IT_NA [°]	-16.6	-15.4	-14.6	-15.5	1.0	6.5 %
IT_CA [°]	4.8	5.7	6.1	5.5	0.7	1.8 %
RF_TICA [°]	36.7	40.0	41.6	39.4	2.5	6.3 %
HAA_tub [°]	13.4	12.2	12.1	12.6	0.7	5.6 %
HAA_will [°]	38.3	39.7	38.7	38.9	0.7	1.8 %
RL_TICA [°]	-87.2	-86.8	-86.4	-86.8	0.4	0.5 %
RT_TICA [°]	84.9	84.6	83.3	84.3	0.9	1.1 %
RF_TACA [°]	70.8	74.4	77.8	74.3	3.5	4.7 %
RL_TACA [°]	32.4	32.2	32.2	32.3	0.1	0.3 %
RT_TACA [°]	-21.5	-20.4	-21.3	-21.1	0.6	2.8 %
RF_TANA [°]	67.6	66.9	67.8	67.4	0.5	0.7 %
RL_TANA [°]	19.9	20.0	19.8	19.9	0.1	0.5 %
RT_TANA [°]	-42.8	-41.4	-42.0	-42.1	0.7	1.7 %
RL_CAM1 [°]	150.9	150.3	150.2	150.5	0.4	0.3 %
RL_CATAM1 [°]	130.1	130.0	129.9	130.0	0.1	0.1 %
RL_TAM1 [°]	-6.6	-5.6	-5.5	-5.9	0.6	10.2 %
RT_TAM1 [°]	-20.5	-19.7	-19.8	-20.0	0.4	2.0 %
RT_M1M2 [°]	-10.4	-10.0	-10.6	-10.3	0.3	2.9 %
FAO [mm]	17.6	17.4	17.7	17.6	0.2	1.1 %
FAO [%]	11.8	11.6	11.8	11.7	0.1	0.9 %
Hg-NA_C [mm]	49.5	49.7	49.6	49.6	0.1	0.2 %
Hg-CU_C [mm]	36.7	36.7	36.7	36.7	0.0	0.0 %
Hg-CM_C [mm]	39.7	39.9	39.9	39.8	0.1	0.3 %
Hg-NA [mm]	30.5	30.6	30.5	30.5	0.1	0.3 %
Hg-CU [mm]	21.7	21.7	21.7	21.7	0.0	0.0 %
Hg-CM [mm]	22.2	22.3	22.2	22.2	0.1	0.5 %
I3_CA [°]	-12.2	-12.4	-12.3	-12.3	0.1	0.8 %
I3_TA [°]	20.6	20.2	20.0	20.3	0.3	1.5 %
R3_TICA [°]	76.9	76.6	76.4	76.6	0.3	0.4 %
R3_TACA [°]	39.0	38.3	38.5	38.6	0.4	1.0%
R3_TANA [°]	41.6	40.8	41.4	41.3	0.4	1.0%
R3_CAM1 [°]	151.0	150.4	150.4	150.6	0.3	0.2 %
R3_CATAM1 [°]	126.5	126.5	126.5	126.5	0.0	0.0 %
R3_TAM1 [°]	19.8	18.9	18.9	19.2	0.5	2.6 %

Table 7 Measurements (column on the left) recorded on the foot #1. Every measurement was computed 3 times, in different time moments, using the same procedure. The last three columns show the average over the repetitions, the related standard deviation (sd) and percentage of sd.

As shown in the above-reported table, all the measurements assessed very close values over the repetitions. The intra-operator repeatability is detectable from the standard deviation, which is one order lower than the average values. In order to better visualize the small dispersion of data, the boxplots of the same measurements are reported below (figure 36).

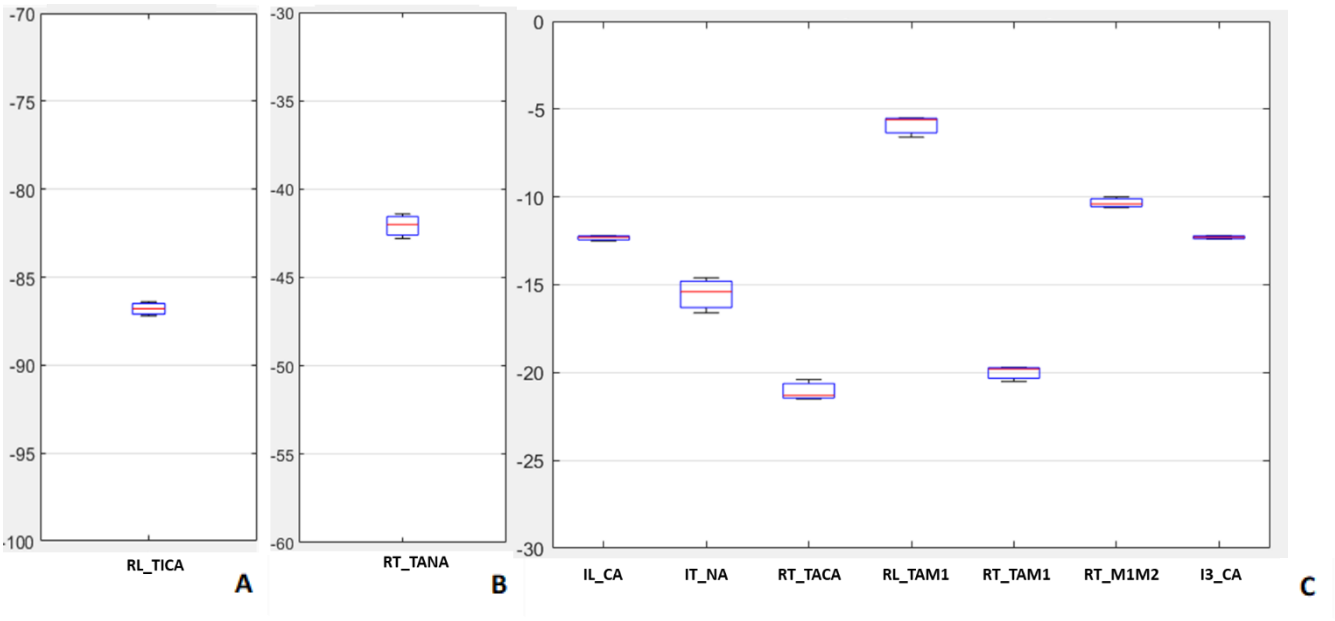
-70
-75
-80
-85
-90
-95
-100
RL_TICA
A
-30
-35
-40
-45
-50
-55
-60
RT_TANA
B
0
-5
-10
-15
-20
-25
-30
IL_CA
IT_NA
RT_TACA
RL_TAM1
RT_TAM1
RT_M1M2
I3_CA
C

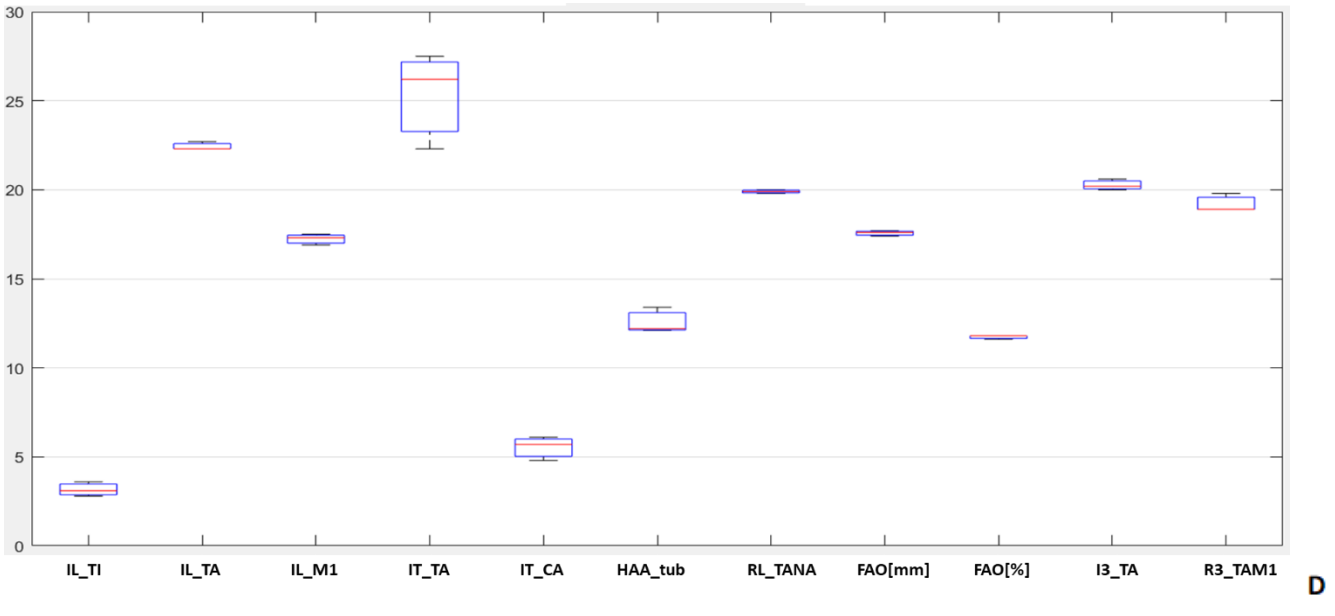
30
25
20
15
10
5
0
IL_TI
IL_TA
IL_M1
IT_TA
IT_CA
HAA_tub
RL_TANA
FAO[mm]
FAO[%]
I3_TA
R3_TAM1
D

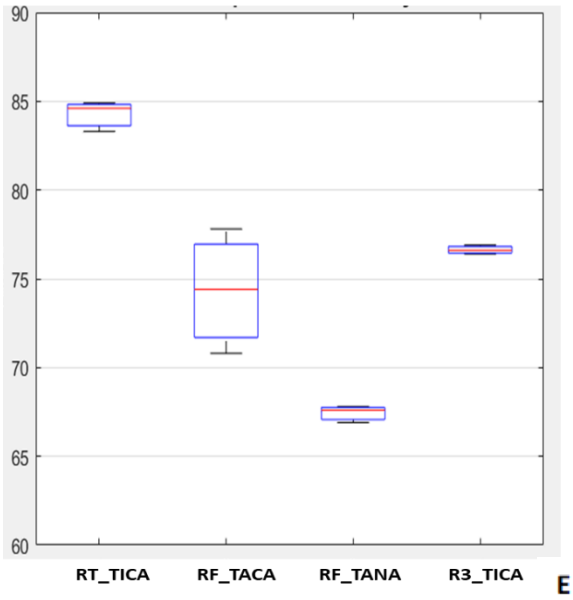
90
85
80
75
70
65
60
RT_TICA
RF_TACA
RF_TANA
R3_TICA
E

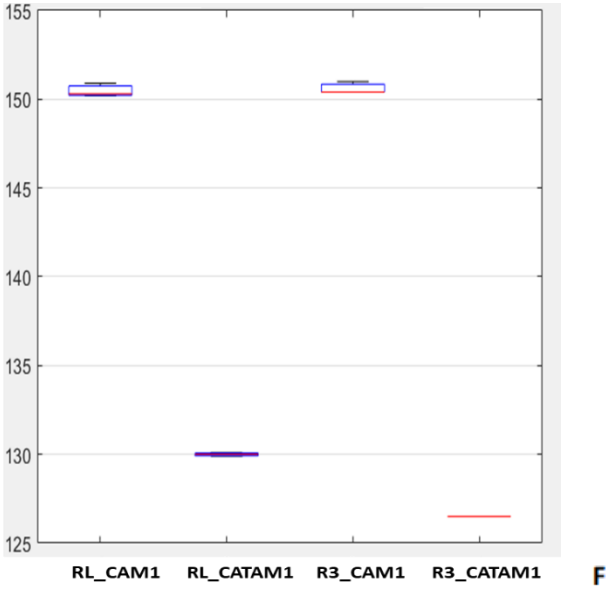
155
150
145
140
135
130
125
RL_CAM1
RL_CATAM1
R3_CAM1
R3_CATAM1
F

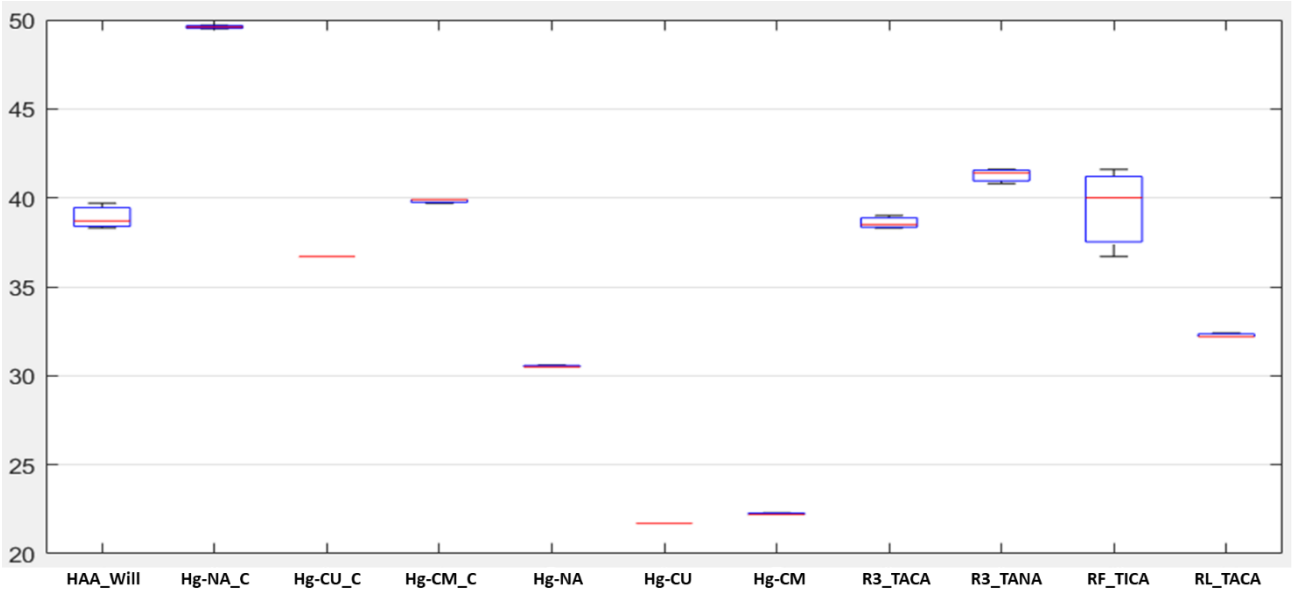

Figure 36 Box plots of foot #1 measurements. The data are divided in different plots in order to have the same scale and, so, to compare them. The intervals of the y-axis are: [-100; -70] (A), [-60; -30] (B), [-30; 0] (C), [0; 30] (D), [20; 50] (E), [60; 90] (F), [125; 155] (G). the scale of the y-axis is the same for every plot.

On each plot, the central line indicates the median, while the bottom and top edges of the box indicate the 25th and 75th percentiles, respectively. The outliers are plotted individually using the '+' marker symbol, but these were not found in this case. Within the considered intervals, all the boxplots show a repeatable behaviour of the measurements with low dispersion. There are only three measurements that appear more variable if compared to the others. They are RF_TACA, RF_TICA, and IT_TA. However, the amplitude of these boxes is always limited, and the number of less repeatable variables is very small, just 3 out of 39.

Finally, in order to evaluate quantitatively the intra-operator repeatability, the ICCs are computed for all the measurements and are here reported in two tables. The former contains the ICCs of the 2D measurements (Table 8), while the latter of the 3D ones (Table 9). In addition to ICCs, the p-values of each coefficient are recorded. p-values are necessary to validate ICCs, because, if the former are smaller than 0.05, the latter are statistically relevant. Moreover, in Table 10, the average value, the standard deviation and the maximum and minimum value of all the ICCs are reported.

	INTRA-OP ICC: 2D MEASUREMENTS	P.VALUE
IL_TI [°]	1.00	4.1E-08
IL_TA [°]	0.87	8.9E-04
IL_M1 [°]	0.99	1.0E-05
IL_CA [°]	1.00	4.9E-07
IT_TA [°]	0.75	2.2E-02
IT_NA [°]	0.93	4.1E-03
IT_CA [°]	0.90	4.4E-03
RF_TICA [°]	0.86	8.4E-03
HAA_tub [°]	0.98	2.5E-04
HAA_will [°]	0.98	3.0E-04
RL_TICA [°]	1.00	2.1E-08
RT_TICA [°]	1.00	1.7E-07
RF_TACA [°]	0.86	8.4E-03
RL_TACA [°]	0.99	1.0E-05
RT_TACA [°]	0.97	2.2E-04
RF_TANA [°]	0.99	7.7E-05
RL_TANA [°]	0.95	1.0E-03
RT_TANA [°]	0.96	6.5E-04
RL_CAM1 [°]	1.00	1.9E-07
RL_CATAM1 [°]	0.99	1.7E-05
RL_TAM1 [°]	0.96	3.7E-05
RT_TAM1 [°]	0.99	8.7E-06
RT_M1M2 [°]	0.98	3.4E-04
FAO [mm]	0.99	1.1E-05
FAO [%]	0.99	1.6E-04
Hg-NA_C [mm]	1.00	1.4E-08
Hg-CU_C [mm]	0.98	2.2E-04
Hg-CM_C [mm]	1.00	7.3E-06
Hg-NA [mm]	1.00	4.3E-10
Hg-CU [mm]	1.00	7.3E-06
Hg-CM [mm]	1.00	1.1E-08

Table 8 Intra-operator ICCs and related p-values, for each 2D measurement. For all the measurements, ICC is higher or equal to 0,75, so a good or excellent intra-operator reliability is assessed

	INTRA-OP ICC: 3D MEASUREMENTS	P.VALUE
I3_CA [°]	1.00	6.4E-08
I3_TA [°]	0.75	1.3E-02
R3_TICA [°]	1.00	1.0E-07
R3_TACA [°]	0.99	1.2E-08
R3_TANA [°]	0.88	7.2E-03
R3_CAM1 [°]	1.00	4.8E-07
R3_CATAM1 [°]	0.99	3.9E-05
R3_TAM1 [°]	0.99	2.2E-06

Table 9 Intra-operator ICCs and related p-values, for each 3D measurement. For all the measurements, ICC is higher or equal to 0,75, so a good or excellent intra-operator reliability.

	INTRA-OP: OVERALL	INTRA-OP: 2D MEASUREMENTS	INTRA-OP: 3D MEASUREMENTS
Average	0.96	0.96	0.95
sd	0.07	0.06	0.09
max	1.00	1.00	1.00
min	0.75	0.75	0.75

Table 10 Intra-operator Average ICC and its related sd. The average ICC is reported for all the measurements, but also for the 2D and 3D ones separately. Also, the maximum and minimum values is reported for the three cases

ICCs values confirmed what was qualitatively visible from the boxplot, i.e., a low dispersion of the data. From the tables, it is notable that, for all the measurements, ICC is higher or equal to 0.75: this proves the good intra-repeatability of the procedure. Moreover, the p-values are smaller than 0.05 for all the ICCs, so these can be considered statistically significant. The robustness of the techniques here exploited was also confirmed by the overall mean value (greater than 0.9) over all the ICCs and its related small standard deviation. This indicates an excellent intra-operator repeatability on average. For instance, apart from 6 measurements (IL_TA, IT_TA, RF_TICA, RF_TACA, I3_TA and R3_TANA), all the others have ICCs values higher than 0.9. Finally, Table 10 clearly demonstrates that there is not a great difference between 2D and 3D data.

6.1.2. Inter-operator repeatability

Even in this case, 39 measurements of the foot bones were used to assess the inter-operator repeatability. These are computed on three different scans, the same used in the intra-operator repeatability analysis (#1, #2, #3), each of them segmented by three operators. All the measurements for the three scans are reported below (table 11).

	BA0						TV0						SM0					
	Op. 1	Op. 2	Op. 3	Average	sd	$\frac{sd}{\lvert Average \rvert} * 100$	Op. 1	Op. 2	Op. 3	Average	sd	$\frac{sd}{\lvert Average \rvert} * 100$	Op.1	Op.2	Op.3	Average	sd	$\frac{sd}{\lvert Average \rvert} * 100$
IL_TI [°]	3.1	3.1	3.3	3.2	0.1	3.1 %	22.6	22.6	22.7	22.6	0.1	0.4 %	12.8	12.5	12.7	12.7	0.2	1.6 %
IL_TA [°]	22.3	22.6	22.6	22.5	0.2	0.9 %	21.9	22.3	21.5	21.9	0.4	1.8 %	20.6	21.2	20.9	20.9	0.3	1.4 %
IL_M1 [°]	17.3	17.4	17.4	17.4	0.1	0.6 %	12.3	12.2	12.3	12.3	0.1	0.8 %	16.0	16.2	16.3	16.2	0.2	1.2 %
IL_CA [°]	-12.5	-12.3	-12.3	-12.4	0.1	0.8 %	-4.7	-4.6	-5.0	-4.8	0.2	4.2 %	-11.6	-11.3	-11.7	-11.5	0.2	1.7 %
IT_TA [°]	22.3	27.5	27.7	25.8	3.1	12.0 %	21.5	22.4	20.6	21.5	0.9	4.2 %	18.7	20.3	20.3	19.8	0.9	4.5 %
IT_NA [°]	-15.4	-15.1	-15.0	-15.2	0.2	1.3 %	-24.1	-23.5	-23.5	-23.7	0.3	1.3 %	-19.4	-16.0	-19.1	-18.2	1.9	10.4 %
IT_CA [°]	5.7	5.7	5.9	5.8	0.1	1.7 %	4.1	4.5	4.4	4.3	0.2	4.7 %	6.8	7.5	7.6	7.3	0.4	5.5 %
RF_TICA [°]	40.0	41.2	41.0	40.7	0.6	1.5 %	48.5	50.6	48.7	49.3	1.2	2.4 %	37.3	40.9	39.6	39.3	1.8	4.6 %
HAA_tub [°]	12.2	13.2	11.8	12.4	0.7	5.6 %	-12.1	-12.4	-11.6	-12.0	0.4	3.3 %	3.7	4.9	4.4	4.3	0.6	14.0 %
HAA_will [°]	39.7	40.5	39.1	39.8	0.7	1.8 %	35.1	34.6	32.2	34.0	1.6	4.7 %	26.9	20.9	28.5	25.4	4.0	15.7 %
RL_TICA [°]	-86.8	-86.9	-74.5	-82.7	7.1	8.6 %	-66.7	-66.7	-62.4	-65.3	2.5	3.8 %	-76.6	-76.9	-65.5	-73.0	6.5	8.9 %
RT_TICA [°]	84.6	85.3	84.3	84.7	0.5	0.6 %	20.7	20.2	21.8	20.9	0.8	3.8 %	35.9	38.1	36.2	36.7	1.2	3.3 %
RF_TACA [°]	74.4	76.2	76.9	75.8	1.3	1.7 %	85.8	89.1	84.9	86.6	2.2	2.5 %	72.0	77.2	76.6	75.3	2.8	3.7 %
RL_TACA [°]	32.2	32.3	34.9	33.1	1.5	4.5 %	25.8	26.1	26.4	26.1	0.3	1.1 %	30.1	30.4	32.7	31.1	1.4	4.5 %
RT_TACA [°]	-20.4	-21.7	-21.8	-21.3	0.8	3.8 %	-17.4	-17.9	-16.2	-17.2	0.9	5.2 %	-11.9	-12.8	-12.8	-12.5	0.5	4.0 %
RF_TANA [°]	66.9	68.2	68.1	67.7	0.7	1.0 %	76.9	77.3	75.6	76.6	0.9	1.2 %	62.3	62.2	63.7	62.7	0.8	1.3 %
RL_TANA [°]	20.0	19.4	19.2	19.5	0.4	2.1 %	13.1	12.6	13.4	13.0	0.4	3.1 %	22.9	19.5	23.4	21.9	2.1	9.6 %
RT_TANA [°]	-41.4	-42.6	-42.7	-42.2	0.7	1.7 %	-45.6	-45.9	-44.1	-45.2	1.0	2.2 %	-38.1	-36.3	-39.5	-38.0	1.6	4.2 %
RL_CAM1 [°]	150.3	150.3	150.3	150.3	0.0	0.0 %	163.0	163.2	162.8	163.0	0.2	0.1 %	152.4	152.5	151.9	152.3	0.3	0.2 %
RL_CATAM1 [°]	130.0	130.1	129.7	129.9	0.2	0.2 %	144.4	145.0	145.0	144.8	0.3	0.2 %	124.5	126.9	127.0	126.1	1.4	1.1 %
RL_TAM1 [°]	-5.6	-5.8	-5.2	-5.5	0.3	5.5 %	-10.4	-10.9	-9.2	-10.2	0.9	8.8 %	-5.1	-5.6	-4.6	-5.1	0.5	9.8 %
RT_TAM1 [°]	-19.7	-21.2	-21.8	-20.9	1.1	5.3 %	-9.6	-9.9	-8.7	-9.4	0.6	6.4 %	-3.8	-4.8	-4.9	-4.5	0.6	13.3 %
RT_M1M2 [°]	-10.0	-9.8	-9.1	-9.6	0.5	5.2 %	-13.8	-14.2	-13.8	-13.9	0.2	1.4 %	-15.8	-16.0	-16.0	-15.9	0.1	0.6 %
FAO [mm]	17.4	17.6	17.3	17.4	0.2	1.1 %	16.4	15.7	16.7	16.3	0.5	3.1 %	11.3	10.4	10.3	10.7	0.6	5.6 %
FAO [%]	11.6	11.8	11.6	11.7	0.1	0.9 %	10.4	10.0	10.6	10.3	0.3	2.9 %	8.8	8.1	8.0	8.3	0.4	4.8 %
Hg-NA_C [mm]	49.7	49.6	49.5	49.6	0.1	0.2 %	43.3	43.2	43.3	43.3	0.1	0.2 %	51.6	51.5	51.5	51.5	0.1	0.2 %
Hg-CU_C [mm]	36.7	36.7	39.5	37.6	1.6	4.3 %	35.5	35.4	35.3	35.4	0.1	0.3 %	36.6	36.5	36.5	36.5	0.1	0.3 %
Hg-CM_C [mm]	39.9	39.9	39.7	39.8	0.1	0.3 %	36.7	36.6	36.6	36.6	0.1	0.3 %	41.2	41.3	41.3	41.3	0.1	0.2 %
Hg-NA [mm]	30.6	30.6	30.5	30.6	0.1	0.3 %	23.1	23.1	23.0	23.1	0.1	0.4 %	35.0	34.8	35.1	35.0	0.2	0.6 %
Hg-CU [mm]	21.7	21.7	21.6	21.7	0.1	0.5 %	20.7	20.6	20.6	20.6	0.1	0.5 %	21.4	21.4	21.4	21.4	0.0	0.0 %
Hg-CM [mm]	22.3	22.2	22.1	22.2	0.1	0.5 %	18.7	18.6	18.6	18.6	0.1	0.5 %	25.1	24.9	24.7	24.9	0.2	0.8 %
I3_CA [°]	-12.4	-12.2	-12.2	-12.3	0.1	0.8 %	-4.7	-4.6	-4.9	-4.7	0.2	4.3 %	-11.5	-11.2	-11.7	-11.5	0.3	2.6 %
I3_TA [°]	20.2	20.2	20.3	20.2	0.1	0.5 %	20.5	20.7	20.2	20.5	0.3	1.5 %	19.6	20.0	19.7	19.8	0.2	1.0 %
R3_TICA [°]	76.6	76.9	76.7	76.7	0.2	0.3 %	63.6	63.6	63.3	63.5	0.2	0.3 %	66.9	67.6	66.9	67.1	0.4	0.6 %
R3_TACA [°]	38.3	38.9	38.9	38.7	0.3	0.8 %	30.4	30.9	29.8	30.4	0.6	2.0 %	33.2	33.6	33.8	33.5	0.3	0.9 %
R3_TANA [°]	40.8	41.6	41.5	41.3	0.4	1.0 %	42.2	42.4	41.0	41.9	0.8	1.9 %	39.1	36.8	40.3	38.7	1.8	4.7 %
R3_CAM1 [°]	150.4	150.5	150.4	150.4	0.1	0.1 %	161.6	161.6	161.5	161.6	0.1	0.1 %	151.8	152.0	151.5	151.8	0.3	0.2 %
R3_CATAM1 [°]	126.5	126.7	126.4	126.5	0.2	0.2 %	141.6	141.8	142.2	141.9	0.3	0.2 %	124.4	127.1	126.9	126.1	1.5	1.2 %
R3_TAM1 [°]	18.9	20.3	20.9	20.0	1.0	5.0 %	12.5	12.9	11.7	12.4	0.6	4.8 %	5.4	6.3	6.1	5.9	0.5	8.5 %

Table 11 The table show the repetitions of the 39 measurements (column on the left), by three different operators (op.1, op.2 and op.3). In the table, on the left the data from scan BA0, at the centre from scan TV0 and on the right from scan SM0.

As shown in the above-reported table, all the measurements showed very close values over the repetitions. The inter-operator repeatability is detectable from the standard deviation, which is at least one order lower than the average values. It is also shown by the percentage of standard deviation that remains small, the only exceptions are some angles

with values lower than 25°. In order to better visualize the small dispersion of data, the boxplots of the data, which seem to have the worst repeatability, are reported below (figure 37). They are the 6 measurements with the lower intra-operator repeatability (IL_TA, IT_TA, RF_TICA, RF_TACA, I3_TA and R3_TANA) and the ones with higher standard deviations among the three operators (RL_TICA, HAA_will and Hg_CU_c). It is also noticeable that some of the measurements with the lower intra-operator repeatability, have also high standard deviation among three different operators, such as IT_TA, RF_TACA and R3_TANA.

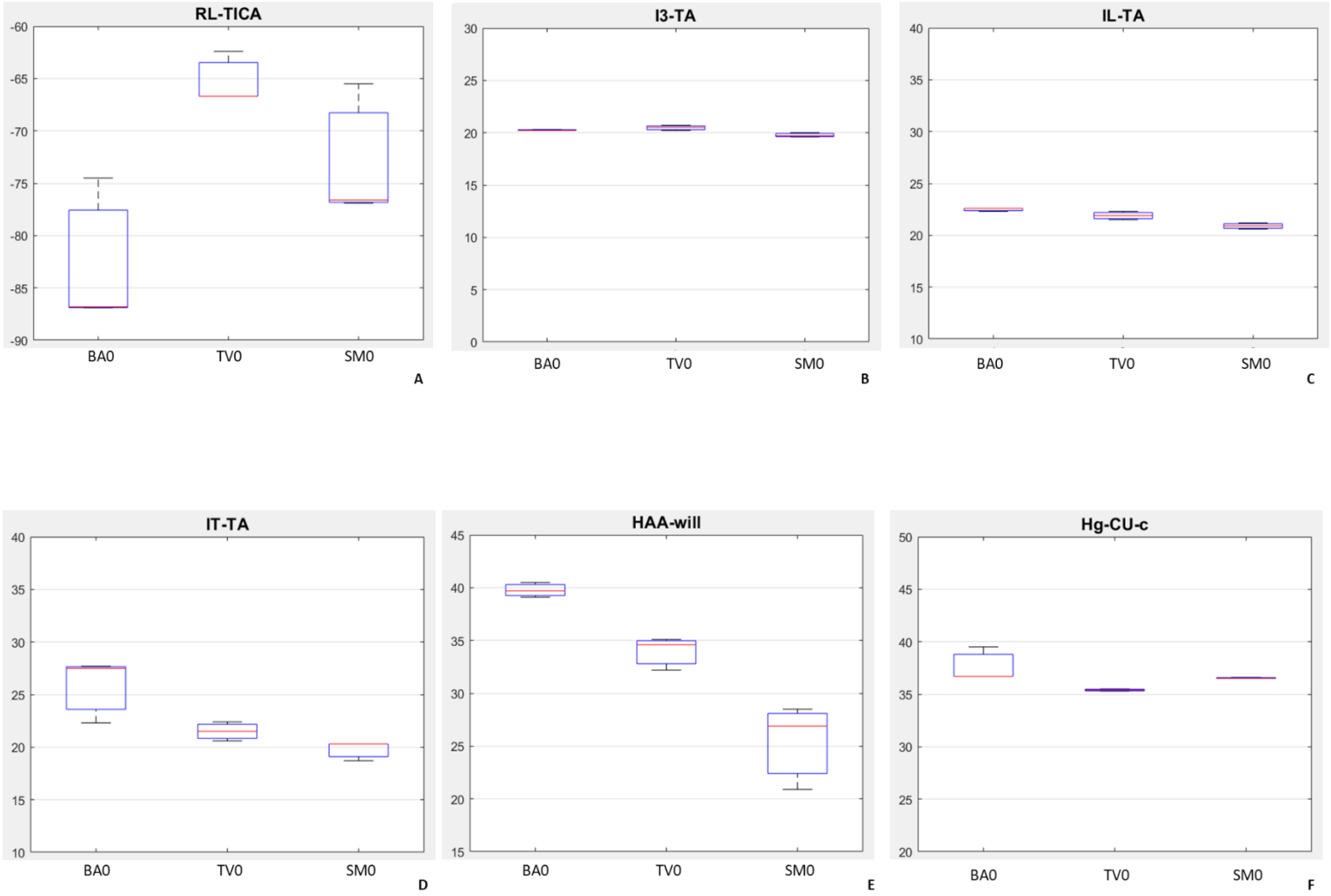

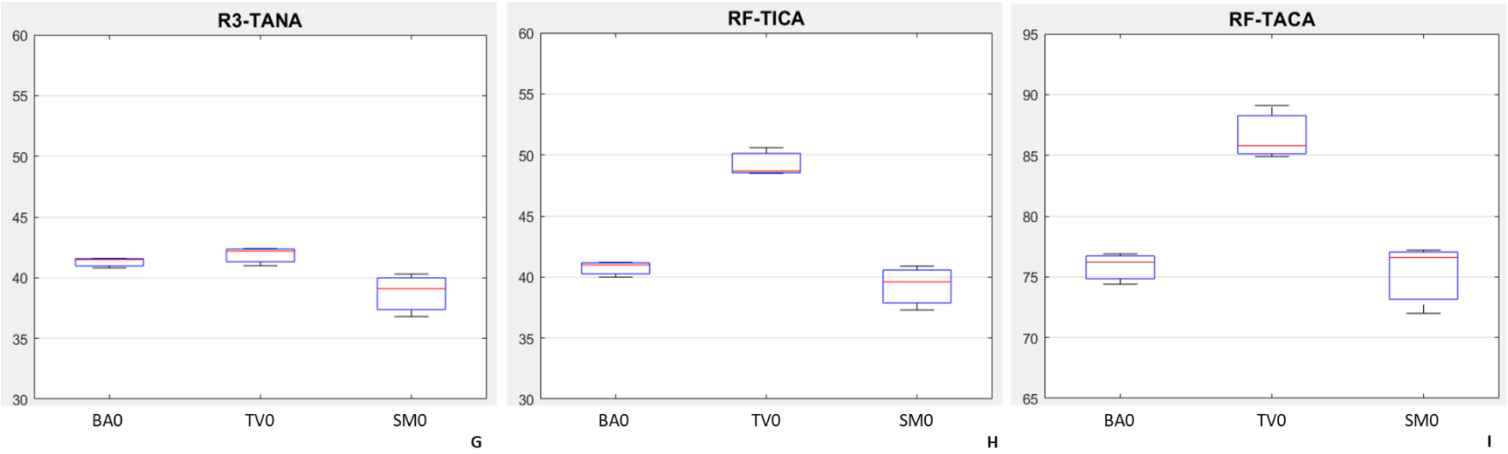

Figure 37 Boxplots of 9 less repeatable measurement compared among BA0, TV0 and scan SM0. The data are divided in different plots in order to better distinguish the different measurements. Boxplots have the same scale, and, so, they are comparable. Moreover, the scale is the same as the intra-operator repeatability boxplots. The intervals of the y-axis are: [-90; -60] (A), [0; 30] (B), [10; 40] (C), [10; 40] (D), [15; 45] (E), [20; 50] (F), [30; 60] (G), [30; 60] (H), [65; 95] (I). Moreover, the scale of the y-axis is the same for every plot.

The boxplots show the dispersion of the measurements with lower repeatability. However, the variability is very low, with a variability between the 25th and 75th percentiles of less than 5 degrees in all the boxplot, with the exception of RL_TICA and HAA_will. In addition, to better evaluate the inter-operator repeatability, the ICCs were computed for all the measurements, similarly to the intra-operator ones. Below two tables are reported: the former contains the ICCs of the 2D measurements (Table 12) while the latter the ICCs of the 3D measurements (Table 13). Moreover, in Table 14, the average value, the standard deviation, and the maximum and minimum value of all the ICCs are reported. Even for the inter-operator repeatability, the p-values related to each ICC are showed.

	INTER-OP ICC: 2D MEASUREMENTS	P.VALUE
IL_TI [°]	1.00	4.4E-09
IL_TA [°]	0.97	3.2E-03
IL_M1 [°]	1.00	6.1E-07
IL_CA [°]	1.00	6.6E-07
IT_TA [°]	0.91	2.5E-02
IT_NA [°]	0.98	1.3E-03
IT_CA [°]	0.99	1.6E-04
RF_TICA [°]	0.99	1.6E-04
HAA_tub [°]	1.00	2.5E-06
HAA_will [°]	0.95	8.8E-03
RL_TICA [°]	0.97	2.7E-03
RT_TICA [°]	1.00	3.2E-07
RF_TACA [°]	0.99	1.6E-04
RL_TACA [°]	0.99	6.1E-04
RT_TACA [°]	0.99	3.0E-04
RF_TANA [°]	0.99	1.4E-04
RL_TANA [°]	0.98	1.5E-03
RT_TANA [°]	0.95	7.7E-03
RL_CAM1 [°]	1.00	1.6E-07
RL_CATAM1 [°]	1.00	1.7E-05
RL_TAM1 [°]	1.00	5.5E-05
RT_TAM1 [°]	1.00	3.1E-05
RT_M1M2 [°]	1.00	3.6E-05
FAO [mm]	0.99	1.2E-04
FAO [%]	0.99	7.9E-04
Hg-NA_C [mm]	1.00	1.4E-08
Hg-CU_C [mm]	0.75	1.1E-01
Hg-CM_C [mm]	1.00	8.5E-07
Hg-NA [mm]	1.00	6.0E-08
Hg-CU [mm]	1.00	1.5E-05
Hg-CM [mm]	1.00	1.7E-07

Table 12 Inter-operator ICCs and related p-values, for each 2D measurement. For all the measurements is higher or equal than 0,75.

	INTER-OP ICC: 3D MEASUREMENTS	P.VALUE
I3_CA [°]	1.00	6.7E-07
I3_TA [°]	0.92	2.0E-02
R3_TICA [°]	1.00	3.2E-07
R3_TACA [°]	1.00	3.7E-05
R3_TANA [°]	0.79	9.0E-02
R3_CAM1 [°]	1.00	6.8E-08
R3_CATAM1 [°]	1.00	3.1E-05
R3_TAM1 [°]	1.00	4.5E-05

Table 13 Inter-operator ICCs and related p-values, for each 3D measurement. For all the measurements, ICC is higher to 0,75, so a good or excellent inter-operator reliability is assessed

	INTER-OP: OVERALL	INTER-OP: 2D MEASUREMENTS	INTER-OP: 3D MEASUREMENTS
Average	0.98	0.98	0.96
sd	0.05	0.05	0.08
max	1.00	1.00	1.00
min	0.75	0.75	0.79

Table 14 Inter-operator Average ICC and its related sd. The average ICC is reported for all the measurements, but also for the 2D and 3D ones separately. Also, the maximum and minimum values is reported for the three cases.

Overall, the mean ICC is equal to 0.98, with a standard deviation of 0.05, indicating an excellent inter-operator reliability on average. The high repeatability resemble the ICCs values the intra-operator ones. The ICCs of only 2 measurements (Hg-CU_c and R3_TANA) are lower than 0.9, while all the other values indicate an excellent inter-operator repeatability, with p-values lower than 0.05, so statistically relevant. Even the two measurements that seemed less repeatable from the boxplot, present, actually, an excellent repeatability.

In conclusion, none of the 39 measurements have an ICC lower than 0.75 for both intra-operator and inter-operator repeatability analysis. Hence, this process can be considered intra- and inter-operator repeatable.

6.2. Pre-op and Post-op outcomes

The analyzed cohort of the present study involved 10 patients with indication for SAMBB: these were scanned both pre-op and post-op. the average follow up is 10.6 months with a standard deviation of 5.9, maximum follow up of 25.7 months and minimum of 7 months. It is worth to highlight that, by having such a small population, results cannot have a great statistical power. However, these were sufficient for the aim of this thesis, proving the validity of the technical procedure presented in this study. In order to prove that, the characterization of the morphology of flatfoot, by means of measurements automatically computed will be reported, for both the pre-op and the post-op scans.

The relevant question is whether the surgery pointed in the right direction and whether the measures computed by automatic algorithms are able to characterize and quantify this change. To answer it, only 27 out of the 39 reported measurements were used, being the ones that better describe this pathology. The choice of these measures was, in fact, based on a survey proposed to surgeons who were asked to choose which of the proposed angles could be most useful to characterize flatfoot, thus better highlighting any sort of improvement in bones relationship.

The evaluation of the changes in the foot morphology pre- and post-op was accomplished by three different analyses. First, the pre-op and post-op measurements were observed and compared to values from controls by means of tables, plots, and images. Secondly, among all the patients, the two with the biggest and smallest pre-post differences in the measurements were analyzed more in detail. Lastly, a statistical analysis was performed, to assess if the differences between pre-op and post-op values are statistically significant and if there is any correlation between the measurements and the clinical indices FPI and FFI.

Data collected from 10 analysed subjects were reported in two tables, separately for the pre-op (Table 15) and the post-op values (Table 16). If the patient code ends with “0”, it refers to the pre-op evaluation, while “1” refers to the post-op one. The 3D models of the scans were segmented by two operators (operator 1 and operator 3 of the repeatability analysis). Each operator segmented the same foot in the pre-op and in the post-op. In particular, operator 1 segmented BA, DER, DN, SM, TV; while, operator 3 segmented AC, CP, LM, MM, VL.

Scan code / Measurement	AC0	BA0	CP0	DER0	DN0	LM0	MM0	SM0	TV0	VL0	Average	sd
IL_TA [°]	17.5	22.3	27.6	30.3	20.5	34.9	33.2	20.6	21.9	25.4	25.4	5.9
IL_CA [°]	-17.2	-12.5	-7.8	-5.3	-7.9	-7.7	-5.0	-11.6	-4.7	-3.1	-8.3	4.3
IT_TA [°]	19.3	22.3	33.9	15.3	15.3	44.4	40.9	18.7	21.5	40.1	27.2	11.4
IT_CA [°]	5.3	5.7	5.5	10.6	10.7	12.1	3.9	6.8	4.1	5.5	7.0	3.0
HAA_Will [°]	40.3	39.7	40.2	35.9	49.4	42.3	36.9	26.9	35.1	37.9	38.5	5.7
RL_TACA [°]	34.6	32.2	35.5	35.6	28.3	42.6	38.2	72.0	25.8	28.4	37.3	13.2
RT_TANA [°]	-28.7	-41.4	-69.5	-31.2	-53.8	-69.1	-65.0	-38.1	-76.9	-58.5	-53.2	17.3
RL_CAM1 [°]	149.0	150.3	161.8	164.1	169.2	159.0	165.2	152.4	163.0	161.5	159.6	6.8
RL_CATAM1 [°]	129.6	130.0	142.2	150.3	144.3	141.7	144.1	124.5	144.4	144.2	139.5	8.4
RL_TAM1 [°]	-3.6	-5.6	-17.2	-19.7	-17.6	-21.6	-23.3	-5.1	-10.4	-10.0	-13.4	7.3
RT_TAM1 [°]	-22.7	-19.7	-28.4	-20.8	-6.7	-32.6	-36.8	-3.8	-9.6	-34.8	-21.6	11.8
RT_M1M2 [°]	-6.5	-10.0	-14.5	-11.9	-19.3	-16.6	-12.4	-15.8	-13.8	-13.5	-13.4	3.6
FAO [%]	11.5	11.6	17.9	22.5	24.9	14.2	12.7	8.8	10.4	15.1	15.0	5.3
Hg_NA_c [mm]	45.1	49.7	36.3	39.9	38.0	37.0	38.2	51.6	43.3	41.6	42.1	5.3
Hg_CU_c [mm]	33.3	36.7	32.8	39.9	34.7	30.3	27.9	36.6	35.5	25.8	33.4	4.3
Hg_CM_c [mm]	37.3	39.9	31.2	31.7	28.3	31.2	30.8	41.2	36.7	36.7	34.5	4.4
Hg_NA [mm]	30.0	30.6	15.7	19.3	16.7	19.8	20.7	35.0	23.1	26.7	23.8	6.5
Hg_CU [mm]	18.5	21.7	17.2	26.9	19.7	18.4	13.7	21.4	20.7	11.6	19.0	4.3
Hg_CM [mm]	21.1	22.3	15.1	16.1	12.4	15.9	15.9	25.1	18.7	21.8	18.4	4.0
I3_CA [°]	-17.1	-12.4	-12.4	-5.2	-7.7	-7.5	-5.0	-11.5	-4.7	-3.0	-8.7	4.5
I3_TA [°]	16.6	20.2	20.2	29.4	19.8	26.5	26.3	19.6	20.5	19.9	21.9	4.0
R3_TICA [°]	60.8	76.6	76.6	88.5	72.7	66.7	76.8	66.9	63.6	77.6	72.7	8.3
R3_TACA [°]	36.3	38.3	38.3	34.9	27.9	46.3	47.5	33.2	30.4	41.0	37.4	6.3
R3_TANA [°]	31.6	40.8	40.8	28.6	49.7	58.5	54.9	39.1	42.2	53.6	44.0	10.0
R3_CAM1 [°]	147.9	150.4	150.4	157.5	169.2	159.5	165.2	151.8	161.6	161.6	157.5	7.1
R3_CATAM1 [°]	127.4	126.5	126.5	129.8	125.9	136.8	139.1	124.4	141.6	133.3	131.1	6.2
R3_TAM1 [°]	22.0	18.9	18.9	27.1	18.2	33.4	38.5	5.4	12.5	33.4	22.8	10.3

Table 15 Pre-op scans measurements. The first column identifies the measurement, the first row identifies the scan by mean of a code, ordered by alphabet. Each code ends with "0", which mean pre-op scan. Also, the Average over the sans and related standard deviation are reported.

Scan code / Measurement	AC1	BA1	CP1	DER1	DN1	LM1	MM1	SM1	TV1	VL1	Average	sd
IL_TA [°]	4.8	15.9	17.4	12.8	18.7	13.3	13.3	6.6	5.5	8.5	11.7	5.0
IL_CA [°]	-16.4	-9.9	-10.2	-11.1	-7.9	-12.0	-7.5	-18.2	-10.5	-4.4	-10.8	4.1
IT_TA [°]	-5.2	26.4	-2.8	-1.2	12.5	13.8	16.8	10.3	-4.2	24.7	9.1	11.9
IT_CA [°]	-12.4	-2.2	3.2	1.4	7.4	-0.6	-1.5	1.0	4.0	1.5	0.2	5.2
HAA_Will [°]	13.1	29.0	34.5	30.3	44.7	15.8	21.7	25.3	24.9	28.2	26.8	9.1
RL_TACA [°]	21.2	25.8	26.3	22.9	26.6	24.2	20.8	23.9	15.7	12.9	22.0	4.6
RT_TANA [°]	7.1	-36.5	-2.1	-0.7	-42.7	-20.4	-21.9	-18.2	-8.2	-32.9	-17.7	16.6
RL_CAM1 [°]	141.8	156.1	165.4	151.2	165.6	150.8	157.6	147.2	154.5	157.9	154.8	7.5
RL_CATAM1 [°]	118.4	129.8	125.7	121.8	136.8	126.2	129.9	117.0	129.6	133.0	126.8	6.3
RL_TAM1 [°]	16.9	-1.8	2.7	4.9	-12.1	3.9	1.6	8.1	9.5	9.2	4.3	7.8
RT_TAM1 [°]	11.4	-14.8	-8.6	-13.4	-6.5	1.2	-9.1	-9.4	-14.0	-12.7	-7.6	8.2
RT_M1M2 [°]	-6.6	-11.7	-8.4	-10.4	-13.6	-14.3	-9.1	-14.4	-11.0	-11.9	-11.1	2.6
FAO [%]	4.5	6.6	4.3	5.0	22.1	10.6	5.2	2.3	0.7	6.9	6.8	6.0
Hg_NA_c [mm]	56.7	46.5	61.9	55.1	40.1	48.9	47.5	54.4	54.5	50.9	51.7	6.2
Hg_CU_c [mm]	34.9	32.0	41.6	33.1	33.4	31.4	28.8	34.5	34.6	27.1	33.1	3.9
Hg_CM_c [mm]	49.7	41.3	52.6	46.1	30.0	41.3	39.5	46.1	47.8	45.5	44.0	6.3
Hg_NA [mm]	44.2	29.3	47.3	41.0	20.5	35.5	32.8	40.2	38.7	38.3	36.8	7.7
Hg_CU [mm]	18.3	16.5	25.3	16.6	18.2	18.3	14.0	18.7	18.2	12.0	17.6	3.5
Hg_CM [mm]	33.6	23.3	35.3	27.7	13.8	25.2	23.9	29.3	29.2	29.6	27.1	6.1
I3_CA [°]	-16.0	-9.9	-10.2	-11.1	-7.8	-12.0	-7.5	-18.2	-10.5	-4.4	-10.8	4.0
I3_TA [°]	4.8	14.3	17.4	12.8	18.3	12.9	12.8	6.4	5.5	7.7	11.3	4.9
R3_TICA [°]	64.7	69.9	82.9	71.3	78.6	66.9	72.5	62.3	71.9	86.4	72.7	7.8
R3_TACA [°]	22.0	37.3	28.2	24.0	26.6	28.7	27.2	26.3	17.9	26.1	26.4	5.0
R3_TANA [°]	34.5	37.4	15.2	21.8	40.7	35.7	31.4	33.9	29.2	40.4	32.0	8.1
R3_CAM1 [°]	138.1	152.7	146.8	147.6	165.6	147.5	155.9	143.1	146.9	155.9	150.0	7.8
R3_CATAM1 [°]	118.3	129.2	126.5	122.2	125.7	126.4	130.5	118.0	128.5	133.1	125.8	5.0
R3_TAM1 [°]	20.1	14.4	8.5	13.6	13.4	3.9	9.0	11.8	16.4	15.7	12.7	4.6

Table 16 Post-op scans measurements. The first column identifies the measurement, the first row identifies the scan by mean of a code, ordered by alphabet. Each code ends with "0", which mean pre-op scan. Also, the Average over the sans and related standard deviation are reported.

Differences between pre-op and post-op values can be observed but the necessary step forward is to understand if these changes pointed in the direction of morphological improvement. To this purpose, a comparison with a non-pathological foot would be necessary. However, as healthy patients cannot undergo WBCT due to ethical issues associated to radiation doses, only three physiological feet, whose scans were available in the archive for some previous works, were used. But, in order to have more reliable control measurements, it was decided to use some values taken from the literature, whenever a solid control group was found (Table 17). In fact, large dataset of control values was found, but the drawback is that the measurements in literature were computed on 2D RX and by using another procedure. So, control values were used in the comparison between pre-op and post-op, just as an indication of normal values (Table 18).

	Control Average	sd
IL_TA [°]	12.7	3.5
IL_CA_lit. [°]	-22.0	8.0
IT_TA [°]	-23.3	1.7
IT_CA [°]	1.3	10.1
HAA_Will_lit. [°]	5.60	5.4
RL_TACA [°]	-26.7	6.0
RT_TANA [°]	-32.8	10.7
RL_CAM1 [°]	144.6	4.7
RL_CATAM1_lit. [°]	114.20	5,4
RL_TAM1_lit. [°]	0.0	5.0
RT_TAM1 [°]	-10.6	6.3
RT_M1M2 [°]	-12.8	2.3
FAO_lit. [%]	2.30	2.9
Hg_NA_c [mm]	53.8	3.0
Hg_CU_c [mm]	37.1	3.8
Hg_CM_c [mm]	45.2	4.0
Hg_NA [mm]	39.0	4.6
Hg_CU [mm]	22.7	4.0
Hg_CM [mm]	29.3	3.8
I3_CA [°]	-15.5	4.1
I3_TA [°]	11.7	3.3
R3_TICA [°]	73.2	9.2
R3_TACA [°]	36.6	10.0
R3_TANA [°]	45.1	7.1
R3_CAM1 [°]	141.5	9.1
R3_CATAM1 [°]	118.8	6.4
R3_TAM1 [°]	13.0	7.7

Table 17 Reference values obtained as an average over the three normal feet and related standard deviation. These values cannot be considered as real control, because only three patients have been analysed, but they are just indicative numbers. Moreover, the measurements whose name finished with "lit." and their standard deviation have been found in literature [Akoh and Phisitkul, 2019; Williamson et al., 2015; Fernández-Seguín et al., 2019; Lintz et al., 2017].

	Pre-op Average	Post-op Average	Control Average
IL_TA [°]	25.4	11.7	12.7
IL_CA [°]	-8.3	-10.8	-22.0
IT_TA [°]	27.2	9.1	-23.3
IT_CA [°]	7.0	0.2	1.3
HAA_Will [°]	38.5	26.8	5.60
RL_TACA [°]	37.3	22.0	-26.7
RT_TANA [°]	-53.2	-17.7	-32.8
RL_CAM1 [°]	159.6	154.8	144.6
RL_CATAM1 [°]	139.5	126.8	114.20
RL_TAM1 [°]	-13.4	4.3	0.0
RT_TAM1 [°]	-21.6	-7.6	-10.6
RT_M1M2 [°]	-13.4	-11.1	-12.8
FAO [%]	15.0	6.8	2.30
Hg_NA_c [mm]	42.1	51.7	53.8
Hg_CU_c [mm]	33.4	33.1	37.1
Hg_CM_c [mm]	34.5	44.0	45.2
Hg_NA [mm]	23.8	36.8	39.0
Hg_CU [mm]	19.0	17.6	22.7
Hg_CM [mm]	18.4	27.1	29.3
I3_CA [°]	-8.7	-10.8	-15.5
I3_TA [°]	21.9	11.3	11.7
R3_TICA [°]	72.7	72.7	73.2
R3_TACA [°]	37.4	26.4	36.6
R3_TANA [°]	44.0	32.0	45.1
R3_CAM1 [°]	157.5	150.0	141.5
R3_CATAM1 [°]	131.1	125.8	118.8
R3_TAM1 [°]	22.8	12.7	13.0

Table 18 Comparison among pre-op, post-op and control values. Pre-op and post-op measurements are an average over the 10 scans, the control measurements come from an average over the three normal patients, and when possible, from the literature.

To better visualize the changes between pre-op and post-op measurements and their comparison with control values, scatter charts of 20 out of 27 measurements were reported (IL_TA, IT_TA, IL_CA, IT_CA, RL_TACA, RL_CATAM1, RL_TAM1, RT_TAM1, Hg_NA_c, Hg_CU_c, Hg_CM_c, HAA_Will, FAO [%], I3_CA, I3_TA, R3_TICA, R3_TACA, R3_CAM1, R3_TAM1) (Figure 38). Some of the measurements were not considered for the following reasons. RL_CAM1 and R3_CATAM1 were avoided because these both represent the MLA (medial longitudinal arch) morphology, such as the reported RL_CATAM1 and R3_CAM1. Concerning the distances between middle foot bones and the ground, only the measurements from the centroid of the bones to the ground were chosen because the centroid does not change its position after the surgery. Moreover, relative angles involving the navicular bone were not reported because its axes were hardly identified through the PCA technique. Finally, RT_M1M2 and R3_TAM1 were excluded, because mainly RT_TAM1 and RL_TAM1 (i.e., Meary's angle) are taken into account in the literature, for showing the changing in the forefoot orientation with the respect of the hindfoot.

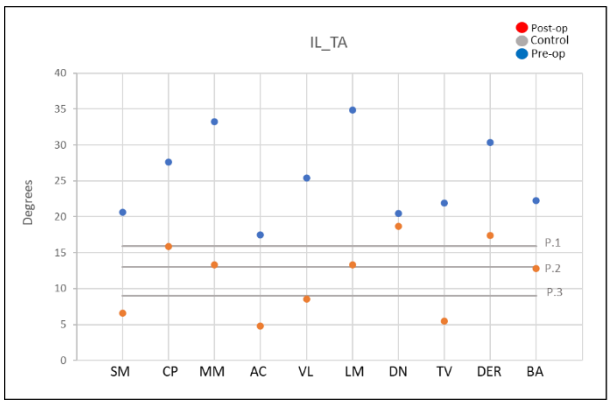

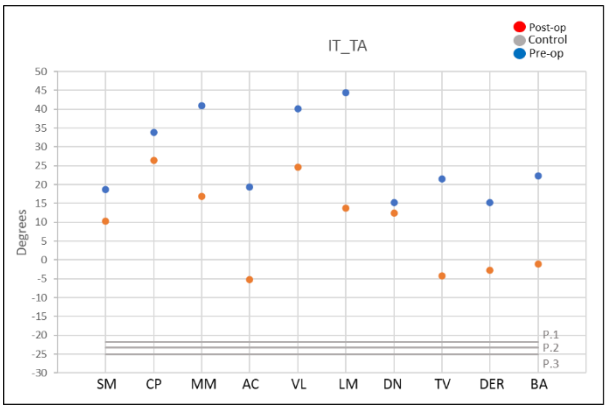

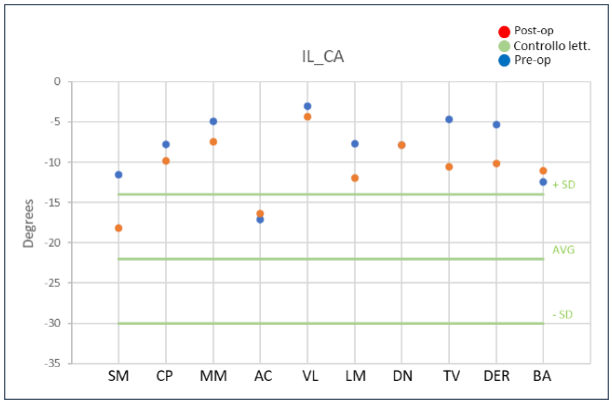

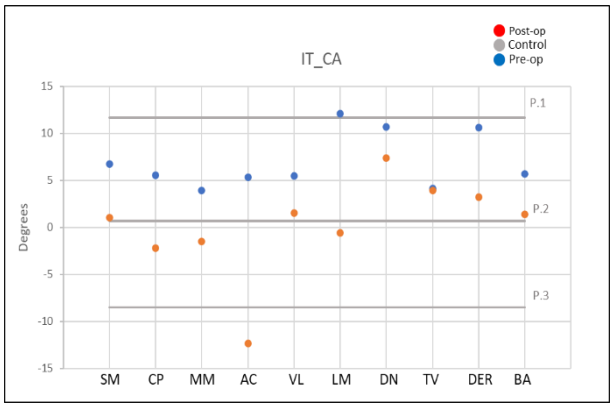

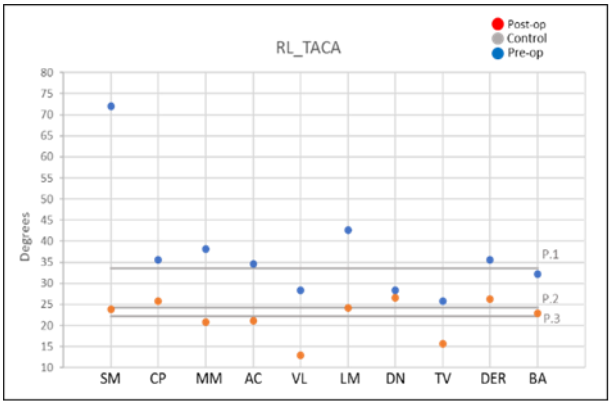
RL_TACA
Post-op
Control
Pre-op
Degrees
P.1
P.2
P.3
SM CP MM AC VL LM DN TV DER BA

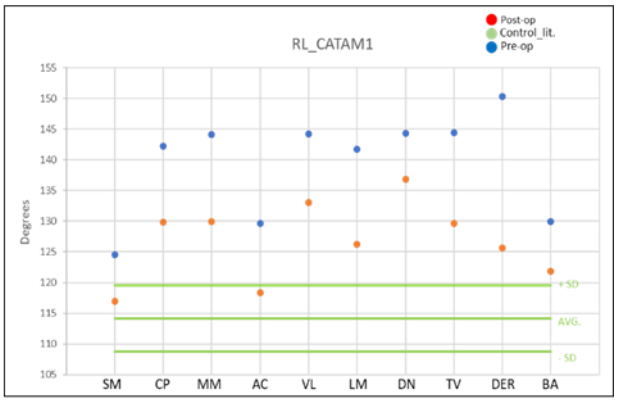
RL_CATAM1
Post-op
Control_lit.
Pre-op
Degrees
+ SD
AVG.
- SD
SM CP MM AC VL LM DN TV DER BA

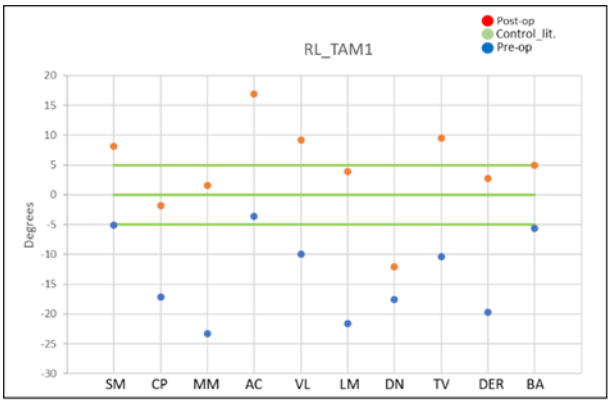
RL_TAM1
Post-op
Control_lit.
Pre-op
Degrees
SM CP MM AC VL LM DN TV DER BA

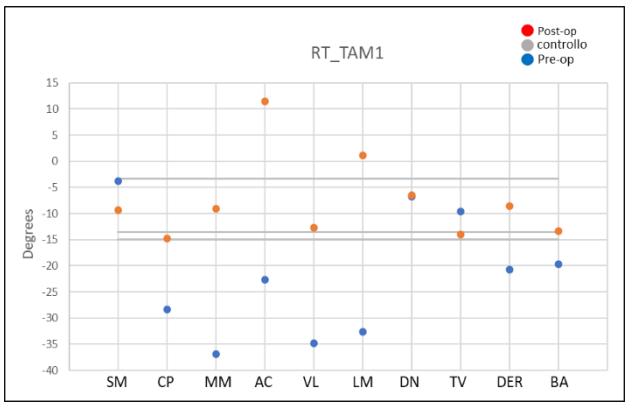
RT_TAM1
Post-op
controllo
Pre-op
Degrees
SM CP MM AC VL LM DN TV DER BA

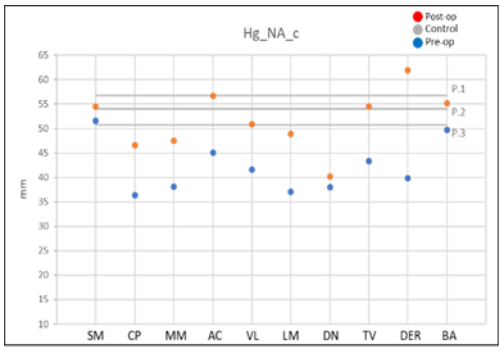
Hg_NA_c
Post-op
Control
Pre-op
mm
P.1
P.2
P.3
SM CP MM AC VL LM DN TV DER BA

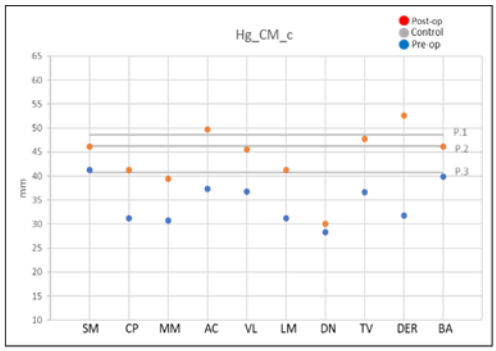
Hg_CM_c
Post-op
Control
Pre-op
mm
P.1
P.2
P.3
SM CP MM AC VL LM DN TV DER BA

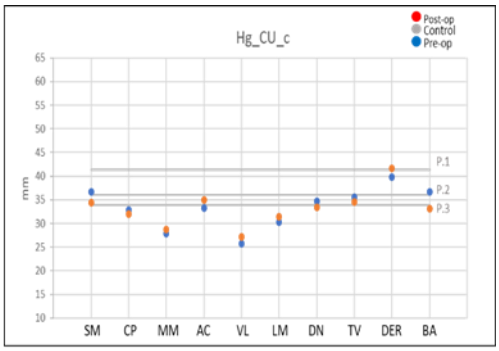
Hg_CU_c
Post-op
Control
Pre-op
mm
P.1
P.2
P.3
SM CP MM AC VL LM DN TV DER BA

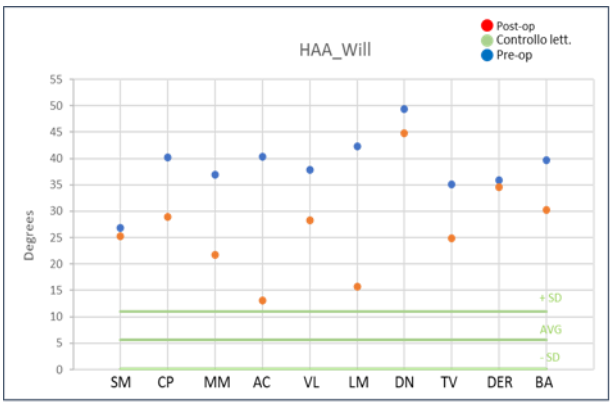
HAA_Will
Post-op
Controllo lett.
Pre-op
Degrees
+ SD
AVG
- SD
SM CP MM AC VL LM DN TV DER BA

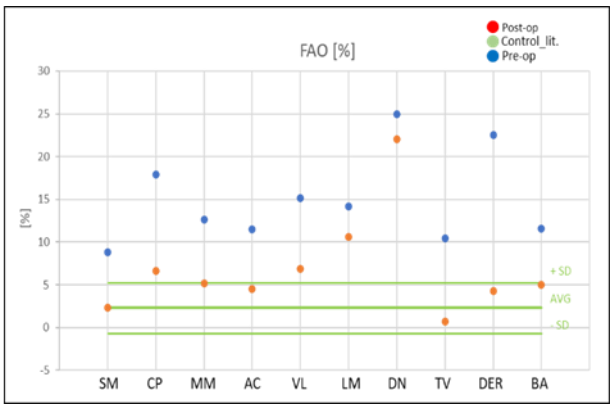
FAO [%]
Post-op
Control_lit.
Pre-op
[%]
+ SD
AVG
- SD
SM CP MM AC VL LM DN TV DER BA

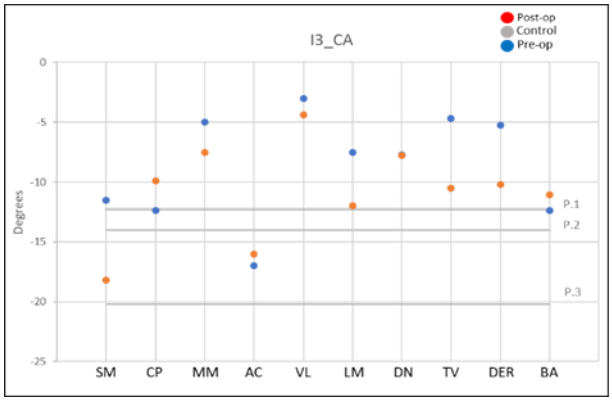

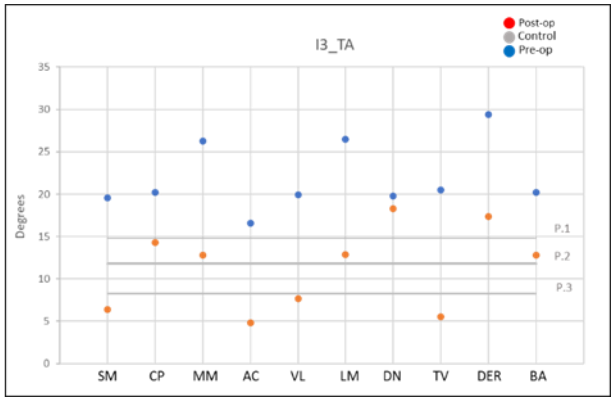

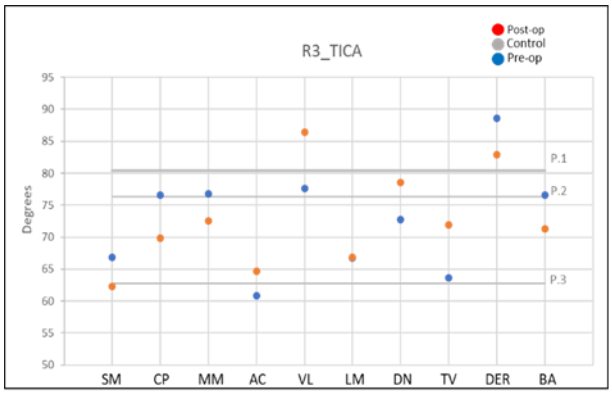

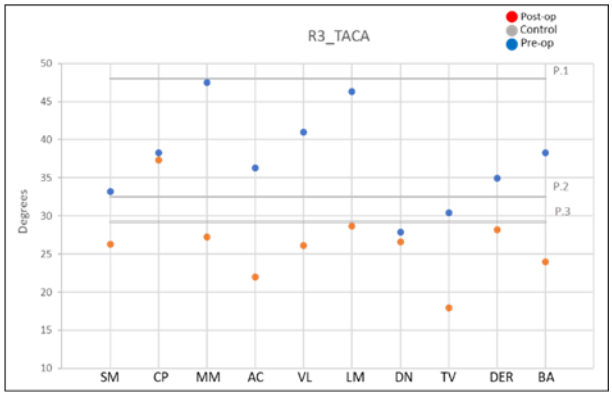

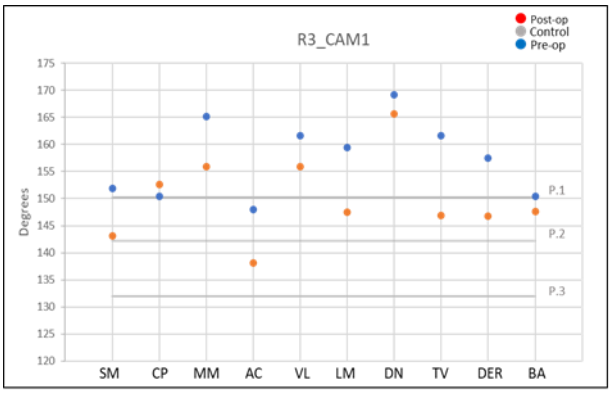

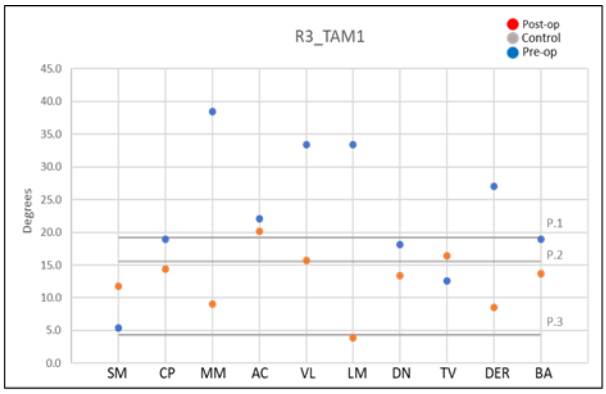

Figure 38 scatter charts representing IL_TA, IT_TA, IL_CA, IT_CA, RL_TACA, RL_CATAM1, RL_TAM1, RT_TAM1, Hg_NA_c, Hg_CU_c, Hg_CM_c, HAA_Will, FAO [%], I3_CA, I3_TA, R3_TICA, R3_TACA, R3_CAM1, R3_TAM1. Blu points are the pre-op measurements, the red points are the post-op measurements. For each plot, the three lines indicates the control values. The grey lines are the control patients, the green lines are the values from the literature.

Overall, the linear and angular measurements obtained from the pre-op versus post-op evaluation were very encouraging, for example, the major deformities involving hindfoot valgus, MLA collapse and forefoot abduction of symptomatic adult foot, revealed interesting improvements. as listed below:

- Absolute angle of the talus reduced in both the lateral (IL_TA) and the transversal (IT_TA) planes. IL_TA from an average value of 25.4° ± 5.9° reached a value of 11.7° ± 5.0°, while IT_TA from 27.2° ± 11.4° went to 9.1° ± 11.9°**.** This means that the axis of the talus after the surgery appears more dorsiflexed and less valgus;
- The inclination of calcaneus on the lateral plane (IL_CA) follows the behaviour of the talus, with a reduction of the angle, passing from -8.3° ± 4.3° to -10.8° ± 4.1°. On the transversal plane (IT_CA), all the values of the post-op scans are closer to 0° (0.2° ± 5.2°), so that the AP axis of the calcaneus appears almost parallel to the anatomical AP axis of the foot;
- Hg_NA_c and Hg_CM_c, represent the hight of navicular and cuneiform medial centroid and can also be used to indicate the MLA height, increased from 42.1 ± 5.3 mm to 51.7 ± 6.2 mm and from 34.5 ± 4.4 mm to 44.0 ± 6.3 mm respectively. However, Hg_CU_c decreased on average from 33.4 ±4.3 mm to 33.1 ±3.9 mm. This can be attributed to a sort of compensation in the bones heights.
- HAA_WILL is the angle between calcaneus tuberosity and the tibial longitudinal axis. It was computed to investigate the valgus of the calcaneus before and after surgery: the preoperative average showed an improvement from 38.5° ± 5.7° to 26.8° ± 9.1° post-op, closer to the literature values of 5.6° ± 5.4°. The hindfoot correction occurred also along with a suitable forefoot correction demonstrated by the decreasing of the Foot and Ankle Offset (FAO): the mean pre-op FAO [%] went from 15.0 ± 5.3 to 6.8 ± 6.0 after surgery, approaching literature values (2.3 ± 2.9).
- Forefoot abduction was here represented as RL_TAM1 and RT_TAM1. They relative angles between the AP axis of the talus and of the first metatarsus. The former is on the lateral view, the latter on the transversal plane. These seemed to move towards normality, passing from a pre-op value of -13.4° ± 7.3° to a post-op value of 4.3 ± 7.8 for RL_TAM1 and from -21.6 ° ± 11.8 ° to -7.6 ° ± 8.2 ° for RT_TAM1. RL_TAM1 was widely reported in literature as Meary's angle, with a value of 0° ± 5°, while the control value for RT_TAM1 is -10.6 ° ± 6.3°. This correction is represented the figure below (Figure 39), where the hindfoot realignment affecting the forefoot orientation is showed

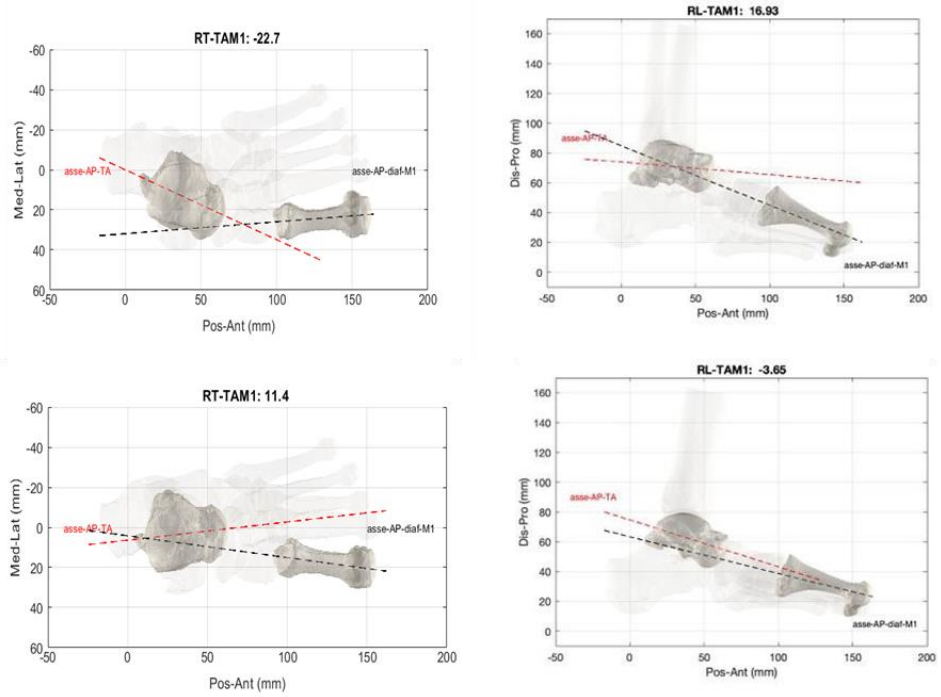

Figure 39 RL_TAM1 and RT_TAM1 pre (top) versus post (bottom), for the patient AC

- The sliding of the talus over the calcaneus, described as the orientation of its longitudinal axis with respect to the longitudinal axis of the calcaneus (RL_TACA), projected on the sagittal plane, has been successfully corrected: the mean preoperative RL_TACA observed was 37.3° ± 13.2 with a post-op improvement to 22.0 ° ± 4.6° at present follow-up. This correction is clearly visible in the figure below (Figure 40), where the repositioning of the talus on the calcaneus for the patient MM was represented in the sagittal plane.

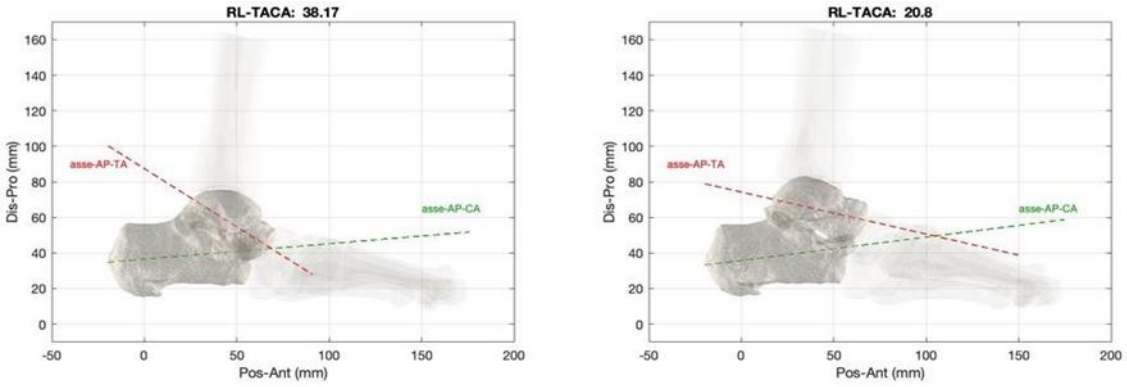

Figure 40 RL_TACA pre-op (left) versus post-op (right) of MM scan. The angle between the AP axes of the talus and of the calcaneus decreased.

.

- The MLA increased its height, so its representative angle decreased in the post-op evaluation as expected, giving a less obtuse angle. For four definitions (RL_CAM1, RL_CATAM1 and the corresponding 3D measures R3_CAM1, R3_CATAM1), the difference before and after surgery was around 7°. An example is given in the figure below (Figure 41) for the patient LM, with initial 141.7° for RL_CATAM1, and 126.2° after treatment.

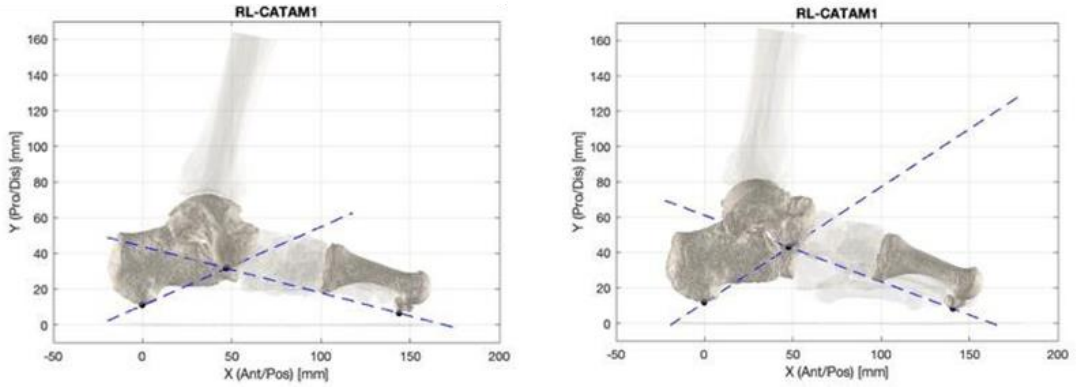

Figure 41 RL_CATAM1 pre-op (left) versus post-op (right) of LM scan. The angle decreased, indicating an uprise of the MLA

Another way to observe if the values of the measurements follow the direction of the desired outcomes of the surgical technique can be carried out by comparing the differences of the pre-op and of the post-op mean values with the control. In the figure below, histograms that represent these differences (in absolute value) were reported (Figure 42). If the height of the column is null, it means that the value is equal to that of the control.

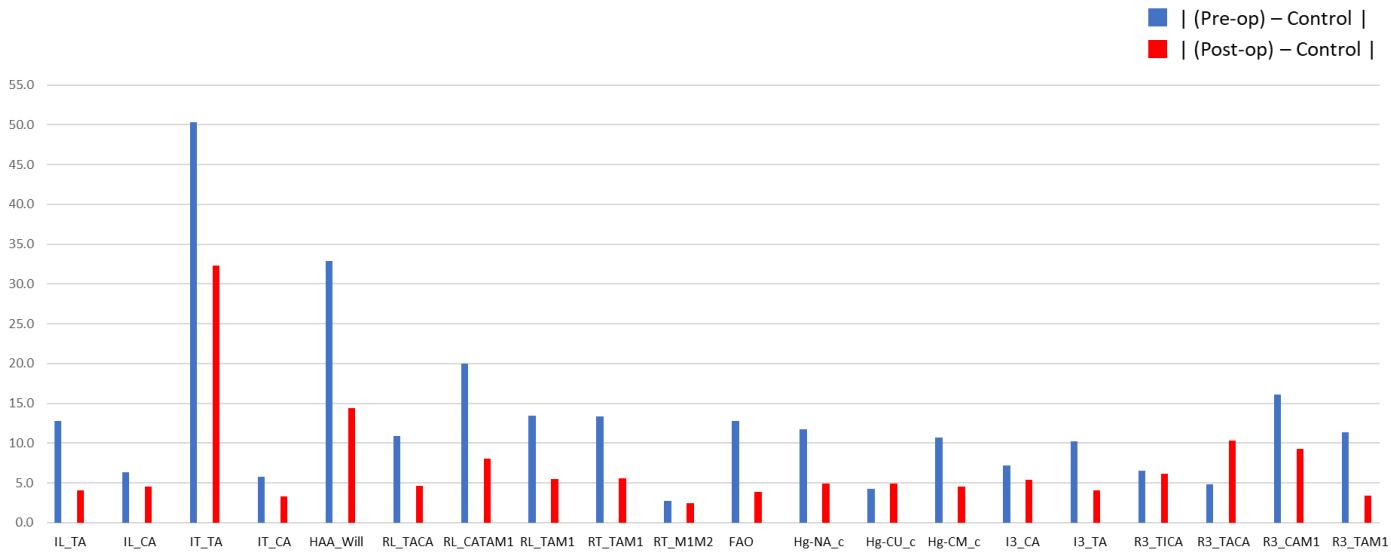

Figure 42 Differences in modulus between the pre-op mean value and the control mean value (blue columns), and differences in modulus between the post-op mean value and the control mean value (red columns). The shorter the column is, the closer to the control the measurement is.

Overall, it is encouraging to note that most of the measurements present a mean difference between post-op and control lower than that between pre-op and control, thus indicating a global re-arrangement of foot morphology in the desired direction. Only Hg_CU_c and some 3D measurements behaved differently. This could be to the fact that the cuboid is the only bone of the middle foot that in some patients descend for compensating the uprising of the MLA. While, concerning the 3D measurements, these are unusual for surgeons and still of difficult geometrical interpretation. This underlines the need to proceed with improvement and updating of these measurements.

6.3. Qualitative Analysis

All the reported results are encouraging because the procedure of segmentation and of computation of automatic measurements gave different outcomes between pre-op and post-op scans and the values became closer to those of the controls. A subsequent step is the observation of the 3D foot models. For this reason, some pictures representing the 3D foot models were provided to qualitatively compare the pre-op and post-op foot bone architecture. Figure 43 shows the models obtained from the scan MM, both in the back (left) and in the lateral (right) views: this one was chosen because presented values very close to the average over the patients, so it can be considered representative of the whole cohort

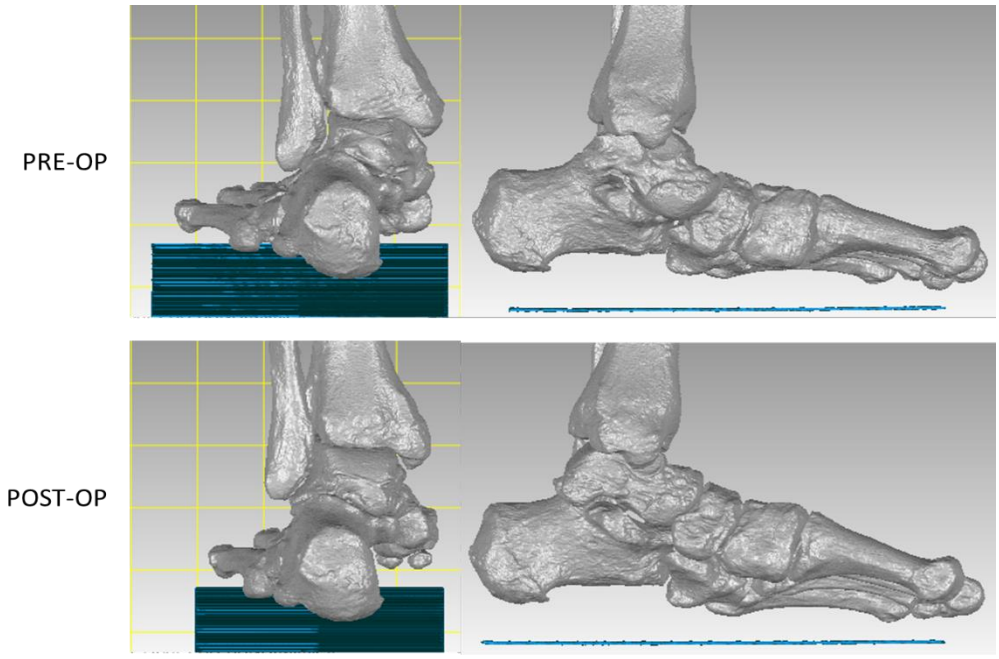

Figure 43 The back and the lateral views of MM scan are shown. The pre-op 3D model is on the top, while the post-op 3D model is on the bottom.

This picture gives a general idea about the overall morphological changes that occurred in the foot after the surgery. In the posterior view, it is immediately visible how the hindfoot has been realigned. Moreover, in the post-op model the first metatarsus appears clearly visible, while in the pre-op it is hidden for a half, indicating a reduction in the abduction of the forefoot. In the lateral view, the MLA arch appears higher, especially in the position of the navicular and of the medial cuneiform, resembling the increasing in Hg_NA_c and Hg_CM_c values. Other clearly visible changes are the extra-rotation and the uprising of the talus, as indicated by IL_TA and IT_TA values. In addition, in the lateral view, the first metatarsus appears more tilted, and all the metatarsal bones are better distinguishable in the post-op model. The comparison between pre-op and post-op scans can also be reported by overlapping the 3D structures, always keeping the calcaneus as reference. In this way the movement of the bones from the pre-op position to the post-op one can be well discernible. In Figure 44 reported below is shown the overlapping of the calcaneus pre-op on the post-op one.

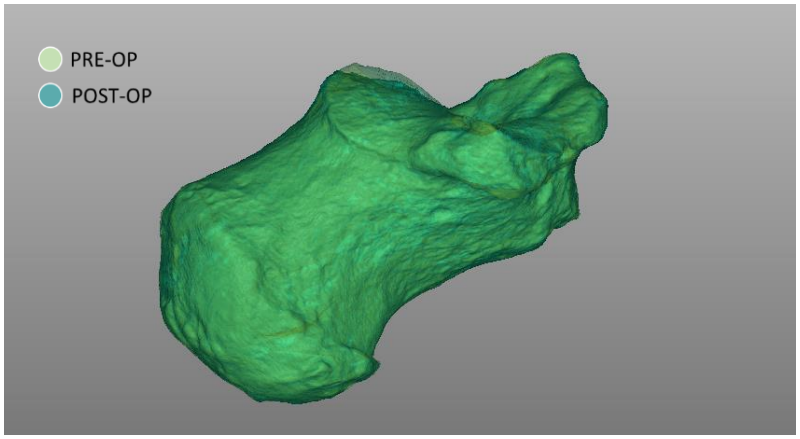

Figure 44 superimposition of the 3D model of the pre-op and post-op calcaneus. The pre-op calcaneus is in light green, the post-op in blue.

The superposition of the calcaneus pre-op over the post-op shows that they are aligned after the best fitting procedure, for instance the two colors are hardly distinguishable. Hence in the following figures only the post-op calcaneus will be reported.

The comparison between pre-op and post-op models by overlapping them, with a focus on the hindfoot (Figure 45), on the forefoot (Figure 46) and on the MLA (Figure 47) are shown below.

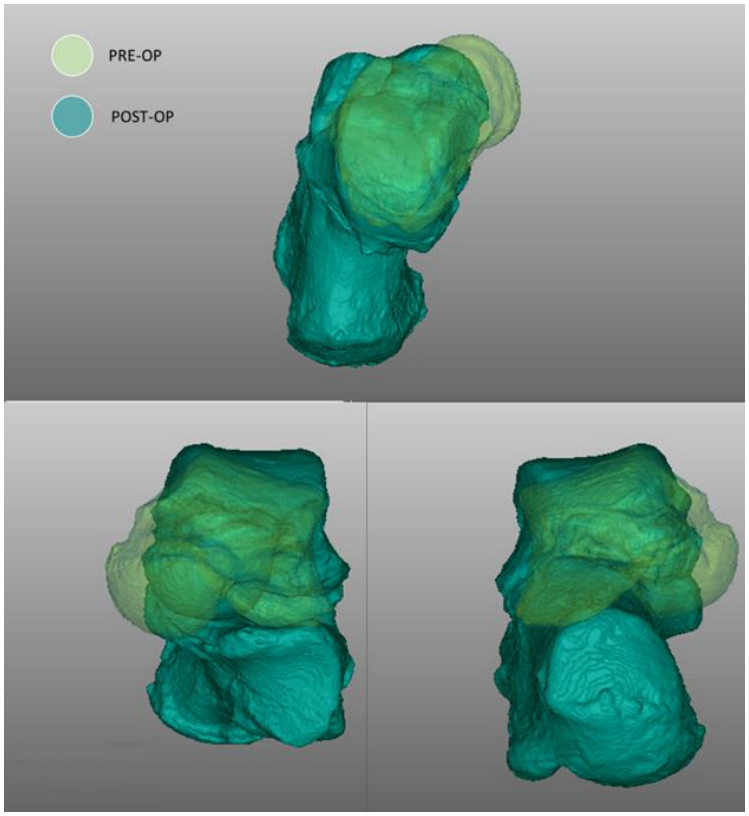

Figure 45 3D model of the MM scan hindfoot. The image is obtained keeping the calcaneus the same position and overlapping the talus pre-op (green) to the talus post-op (blu). The Hindfoot is represent into three different views. The horizontal view (top), the frontal view (bottom-left) and the back view (bottom-right)

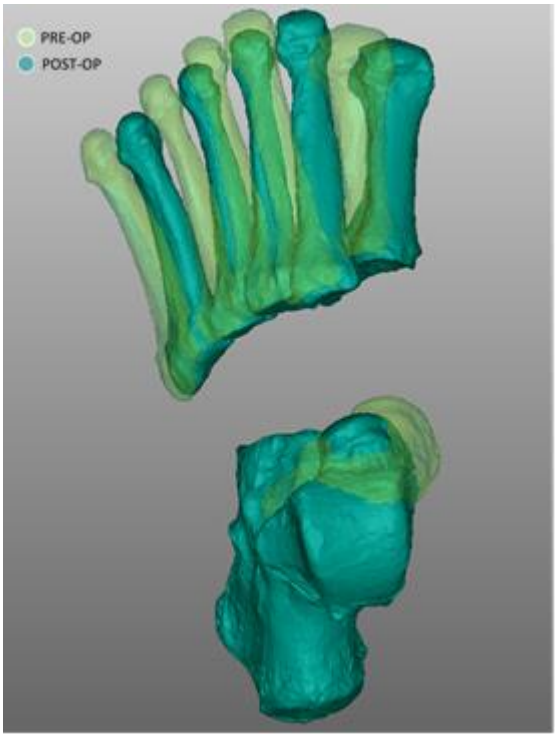

Figure 46 3D model of the MM scan forefoot. The image is obtained keeping the calcaneus as a reference and overlapping the five metatarsal bones and the talus pre-op (green) to the talus post-op (blu). The foot is represented into the horizontal view

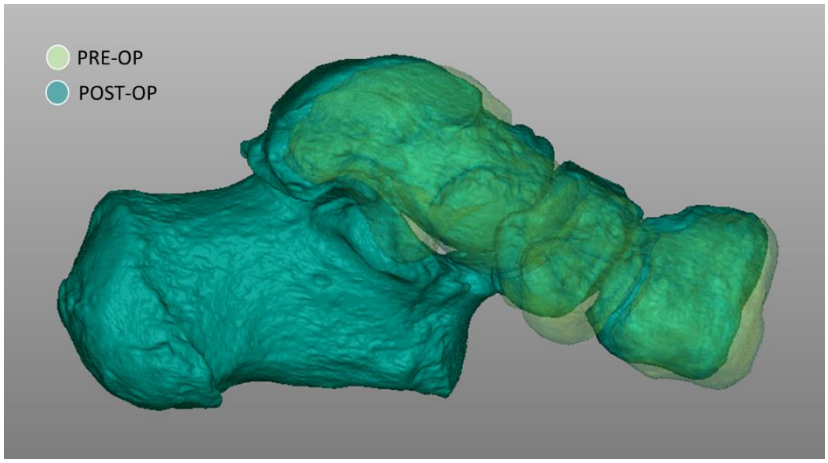

Figure 47 3D model of the MM scan MLA. The image is obtained keeping the calcaneus as a reference and overlapping the navicular and the medial cuneiform pre-op (green) to the talus post-op (blu). The foot is represented into the lateral view

In the figures reported above, it is evident that the talus appears realigned and extra-rotated, the forefoot reduces its abduction, and the bones of the MLA arise.

Eventually, these qualitative views of 3D models are consistent with the quantitative outcomes of the analysis procedure, characterizing all the major and most common deformities of the flatfoot and their changes after surgery.

6.4. Specific cases

In the analysis of foot morphology, both pre-op and post-op, the angular values changed a lot over all the patients, because the level of foot deformation can be very different considering the patient age, sex, and lifestyle. In view of this, two different cases will be here discussed and reported: the first one is the scan LM (LM0 when pre-op, LM1 when post-op), which is a left foot whose differences between pre-op and post-op showed higher values than the average in most of the measurements; the second one is the scan DN (DN0 when pre-op, DN1 when post-op), which is a right foot and showed minimal variations in most of the data instead. For a better understanding, the differences between pre-op and post-op of these two scans were reported in the table below (Table 19).

	LM	DN
IL_TA [°]	21.6	1.8
IL_CA [°]	4.3	0.0
IT_TA [°]	30.6	2.8
IT_CA [°]	12.7	3.3
HAA_Will [°]	26.5	4.7
RL_TACA [°]	18.4	1.8
RT_TANA [°]	48.7	11.1
RL_CAM1 [°]	8.2	3.7
RL_CATAM1 [°]	15.5	7.5
RL_TAM1 [°]	25.5	5.4
RT_TAM1 [°]	33.8	0.2
RT_M1M2 [°]	2.3	5.7
FAO [%]	3.6	2.9
Hg_NA_c [mm]	11.9	2.1
Hg_CU_c [mm]	1.1	1.3
Hg_CM_c [mm]	10.1	1.7
Hg_NA [mm]	15.8	3.8
Hg_CU [mm]	0.1	1.5
Hg_CM [mm]	9.3	1.5
I3_CA [°]	4.5	0.1
I3_TA [°]	13.6	1.5
R3_TICA [°]	0.2	5.9
R3_TACA [°]	17.5	1.3
R3_TANA [°]	22.9	9.0
R3_CAM1 [°]	11.9	3.6
R3_CATAM1 [°]	10.4	0.1
R3_TAM1 [°]	29.5	4.8

Table 19 (Pre-op) - (Post op) differences of the analysed measurements for scan LM and DN.

Table 19 reports larger differences in the values for scan LM than DN. This mismatch involves measurements of the talus, such as IL_TA and IT_TA, whose pre-post difference is 21.6° and 30.6° respectively for LM, and 1.8° and 2.8 for DN. Moreover, in LM scan the forefoot is more affected by the surgical correction than the hindfoot with respect to DN. For instance, RT_TAM1 pre-post difference is 33.8° for LM while it is 0.2° for DN. Other worth-mentioned measurements are the height of the navicular and of the medial cuneiform (Hg_NA_c and Hg_CM_c) that represent the arise of the MLA. Hg_NA_c pre-post difference is 11.9 mm for LM and 2.1 mm for DN, while Hg_CM_c pre-post difference is 10.1 mm for LM and 1.7 mm for DN. This variability between scan DN (right foot) and scan LM (left foot) can be also displayed in the figures below (Figure 48-50).

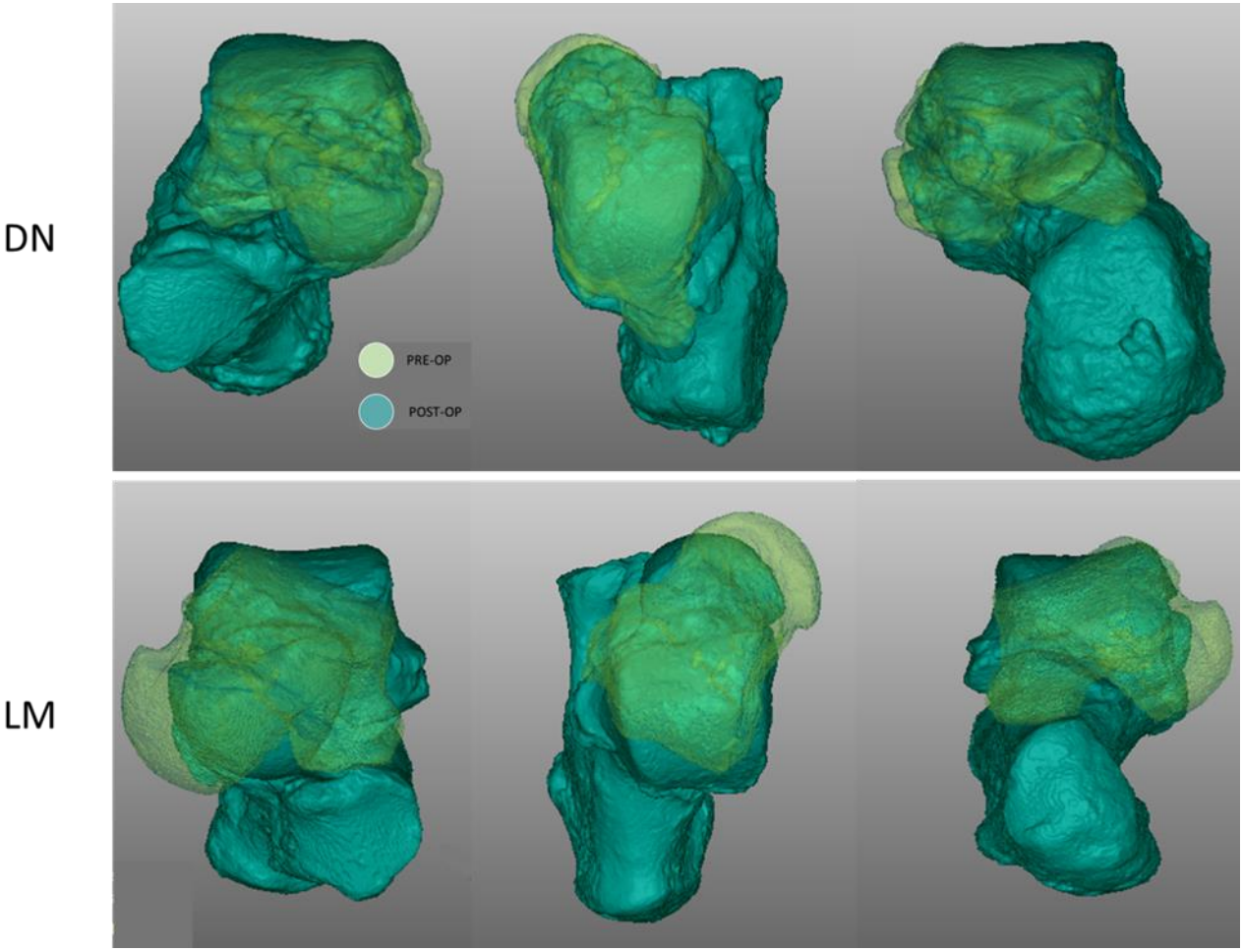

Figure 48 Hindfoot alignment comparison between pre-op and post-op for the scans DN and LM. On the top the pre-post overlapping of DN is represented on the frontal view (top-left), on the horizontal view (top-centre), and on back view (top-right). On the bottom the pre-post overlapping of LM is represented on the frontal view (bottom-left), on the horizontal view (bottom-centre), and on back view (bottom-right). The reference is the calcaneus and the bones in pre-op and post op disposition are shown in green and in blue respectively.

Concerning the talus, besides IL_TA and IT_TA, the different changes in morphology between DN and LM are visible in the 3D models of the overlapped bones. For instance, while the tilting of the talus in LM is noticeable, in DN is barely distinguishable.

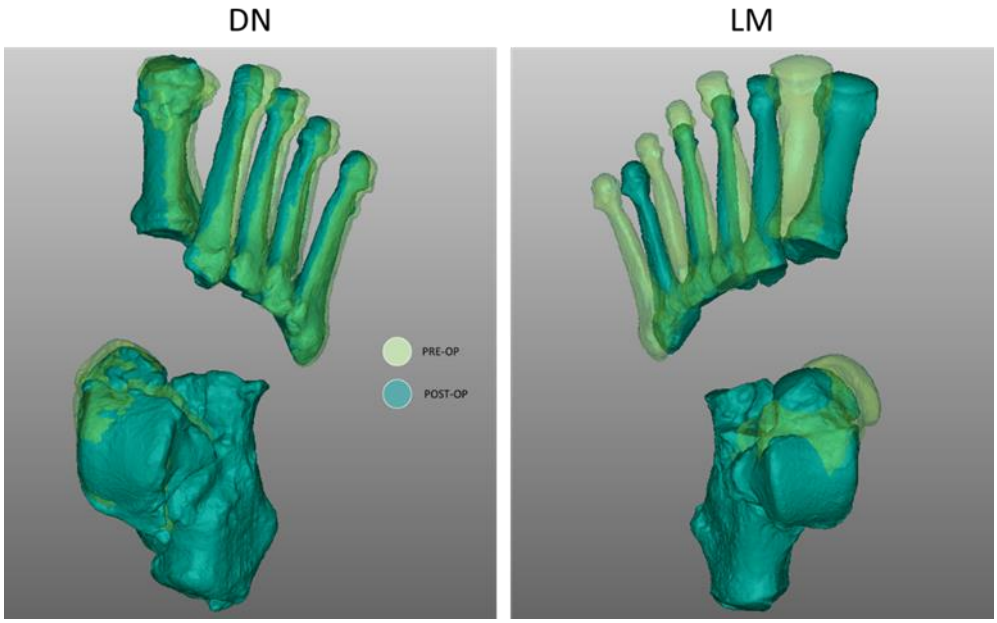

Figure 49 Forefoot abduction comparison between pre-op and post-op for the scans DN and LM. On the left the pre-post overlapping of DN is represented on the horizontal view. On the right the pre-post overlapping of LM is represented on the horizontal view. The reference is the calcaneus and the bones in pre-op and post op disposition are shown in green and in blue respectively.

Figure 49 is a 3D depiction of the relationship between the talus and the metatarsal bones on the transversal view, quantitatively represented by RT_TAM1 measurement, which is the relative angle between these two bones on the transversal plane. The difference between pre-op and post-op is higher in LM than in DN. For instance, in LM, RT_TAM1 decreased from an absolute value of 32.6° to 1.2°. This high reduction of the angle is due to a combination of the reduction in forefoot abduction and in hindfoot valgus.

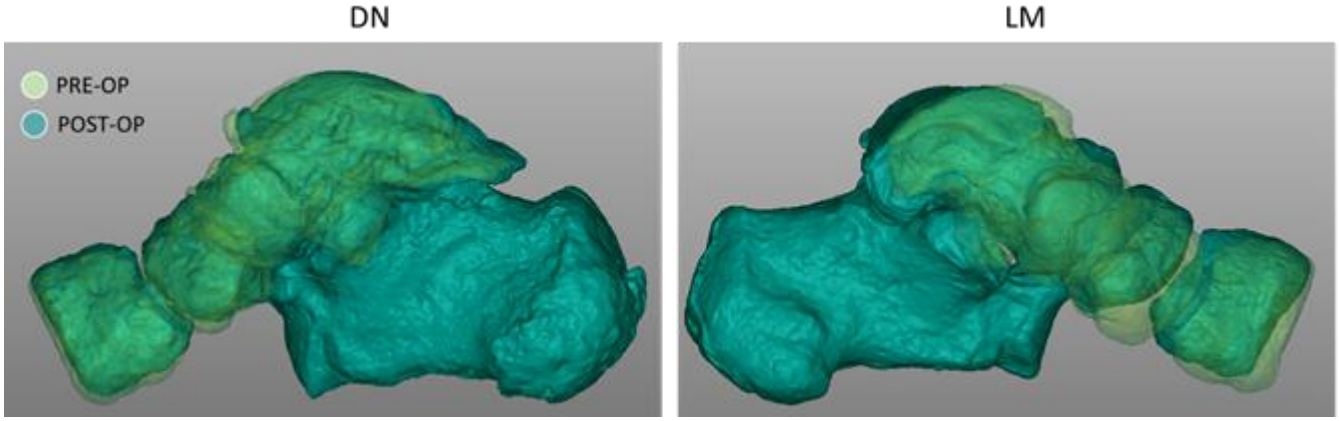

Figure 50 middle foot bones comparison between pre-op and post-op for the scans DN and LM. On the left the pre-post overlapping of DN is represented on the lateral view. On the right the pre-post overlapping of LM is represented on the lateral view. The reference is the calcaneus and the bones in pre-op and post op disposition are shown in green and in blue respectively.

On the lateral view, the uprising of the medial cuneiform and of the navicular are observable. The changing in the hight of these bones is represented by the measurements Hg_NA_c and Hg_CM_c, and even in this case, the figure is coherent to the outcomes of the measurements. For instance, the changing in LM is higher than in DN. What arises now is the question about the reasons of the different effects of the surgery in DN and LM. To do so the LM and DN images of the entire pre-op and post-op models are reported (Figure 51).

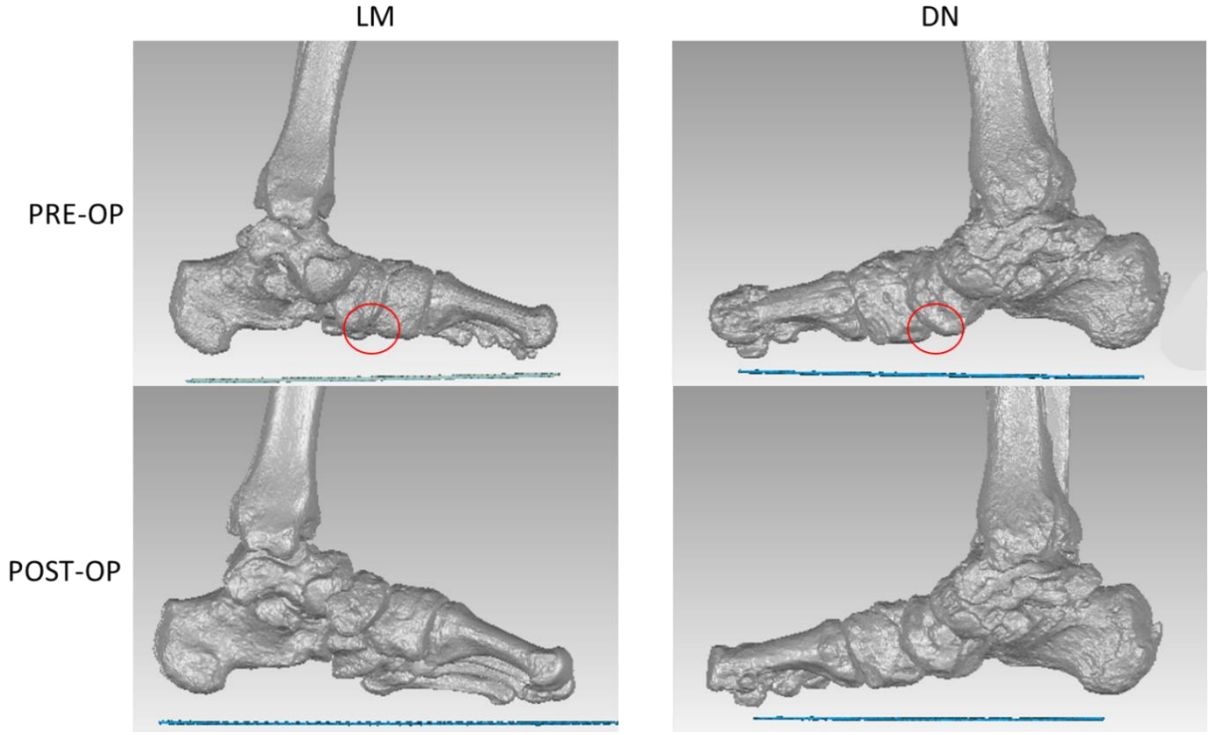

Figure 51 Lateral view of LM (left) and DN (right) scans. Pre-op and post-op scan are represented on the top and on the bottom respectively. The red circle points out the navicular-cuneiform joint.

The SAMBB procedure acts only on the hindfoot alignment, changing all the other bones orientation, thanks to their connections. However, if the deformation of the foot is too severe, only the hindfoot surgery could not be sufficient. The red circle in the figure 50 points out the navicular-cuneiform joint. For instance, in DN the navicular appears more collapsed than in LM, with a substantial reduction of the area of the navicular-cuneiform joint, mainly due to soft tissue laxity. In this case, the correction in the hindfoot is not enough, because the collapsed of the navicular bone reduce the morphological connection

between all the bones, hindering the whole foot architecture improvement. Another proof is the DER scan reported in figure 52.

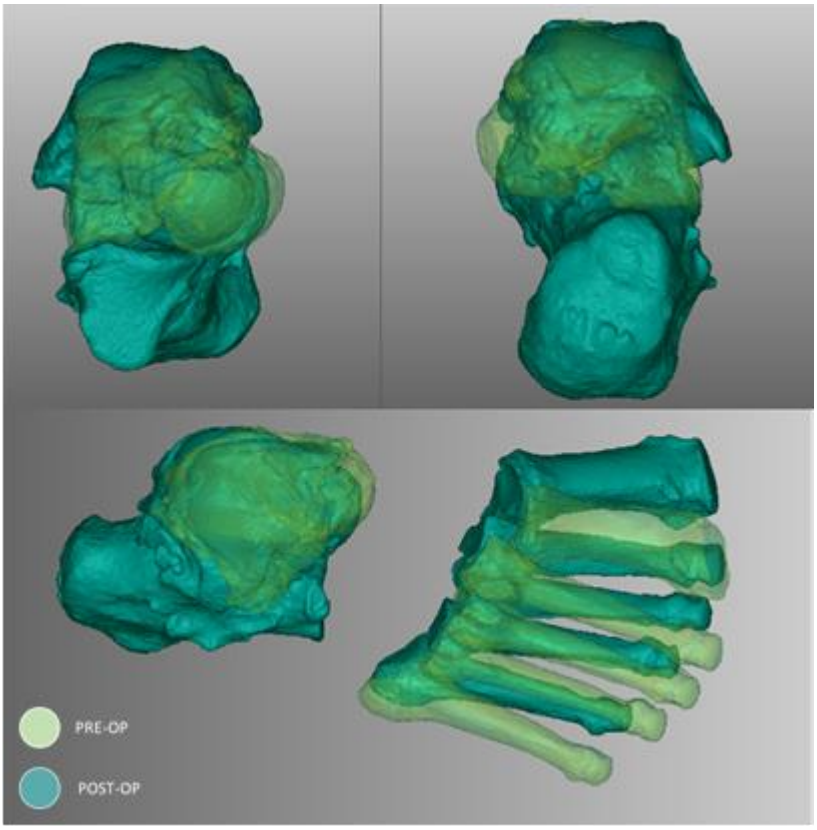

Figure 52 DER 3D model, pre-op versus post op. On the top there is a focus on the hindfoot alignment, on the bottom on the forefoot abduction reduction. The image was saved overlapping the pre-op scan on the post-op, keeping the calcaneus as a reference

This model immediately highlights the changes in the forefoot position probably caused by the hindfoot morphological modification. In particular, while the hindfoot alignment is on average, the forefoot correction is one of the highest among all the cases reported. The cases DN and DER showed how a similar correction in the hindfoot valgus can lead to very different changes in the forefoot alignment.

6.5. Statistical analysis

For the sake of completeness, also the statistical analysis is necessary. The purpose of this analysis is to demonstrate that the differences of the measurements between pre-op and post-op scans are statistically relevant. If so, this morphological analysis procedure can be considered robust. In the table below the pre-op and post-op differences of the data are shown for each scan (Table 20).

	(Pre-op) – (Post-op) Difference											
Scan code / Measurement	AC	BA	CP	DER	DN	LM	MM	SM	TV	VL	Average	sd
IL_TA [°]	12.7	9.5	11.8	12.9	1.8	21.6	19.9	14.0	16.4	16.9	13.8	5.6
IL_CA [°]	-0.7	-1.4	2.0	4.9	0.0	4.3	2.5	6.6	5.9	1.3	2.5	2.8
IT_TA [°]	24.5	23.4	7.5	18.1	2.8	30.6	24.1	8.4	25.7	15.4	18.1	9.2
IT_CA [°]	17.7	4.3	7.8	7.4	3.3	12.7	5.5	5.7	0.2	4.0	6.9	5.0
HAA_Will [°]	27.2	9.5	11.2	1.4	4.7	26.5	15.2	1.6	10.2	9.6	11.7	9.1
RL_TACA [°]	13.4	9.3	9.7	9.4	1.8	18.4	17.4	48.1	10.1	15.5	15.3	12.5
RT_TANA [°]	-35.8	-40.7	-33.0	-29.1	-11.1	-48.7	-43.1	-19.9	-68.8	-25.6	-35.6	16.2
RL_CAM1 [°]	7.2	-0.9	5.7	-1.3	3.7	8.2	7.6	5.2	8.6	3.7	4.8	3.5
RL_CATAM1 [°]	11.2	8.1	12.4	24.6	7.5	15.5	14.2	7.5	14.8	11.2	12.7	5.1
RL_TAM1 [°]	-20.6	-10.6	-15.4	-22.4	-5.4	-25.5	-25.0	-13.1	-19.9	-19.2	-17.7	6.5
RT_TAM1 [°]	-34.1	-6.4	-13.5	-12.1	-0.2	-33.8	-27.8	5.6	4.4	-22.1	-14.0	15.0
RT_M1M2 [°]	0.0	0.4	-2.8	-3.5	-5.7	-2.3	-3.3	-1.4	-2.8	-1.6	-2.3	1.8
FAO [%]	7.0	6.6	11.3	18.2	2.9	3.6	7.5	6.5	9.7	8.2	8.2	4.3
Hg_NA_c [mm]	-11.6	-5.4	-10.2	-22.0	-2.1	-11.9	-9.4	-2.8	-11.2	-9.3	-9.6	5.6
Hg_CU_c [mm]	-1.6	3.7	0.8	-1.8	1.3	-1.1	-0.9	2.2	0.9	-1.3	0.2	1.8
Hg_CM_c [mm]	-12.3	-6.3	-10.1	-20.9	-1.7	-10.1	-8.7	-4.8	-11.1	-8.8	-9.5	5.1
Hg_NA [mm]	-14.2	-10.4	-13.6	-28.0	-3.8	-15.8	-12.1	-5.2	-15.5	-11.6	-13.0	6.6
Hg_CU [mm]	0.2	5.1	0.7	1.5	1.5	0.1	-0.3	2.7	2.5	-0.5	1.4	1.7
Hg_CM [mm]	-12.5	-5.4	-8.2	-19.2	-1.5	-9.3	-8.0	-4.2	-10.5	-7.8	-8.7	4.9
I3_CA [°]	-1.0	-1.3	-2.5	5.0	0.1	4.5	2.5	6.7	5.9	1.3	2.1	3.3
I3_TA [°]	11.7	7.4	5.9	12.0	1.5	13.6	13.6	13.2	15.1	12.2	10.6	4.3
R3_TICA [°]	-3.9	5.4	6.7	5.7	-5.9	-0.2	4.2	4.5	-8.3	-8.8	-0.1	6.2
R3_TACA [°]	14.3	14.3	1.0	6.8	1.3	17.5	20.3	6.9	12.5	14.9	11.0	6.6
R3_TANA [°]	-2.9	19.1	3.4	13.3	9.0	22.9	23.5	5.2	13.0	13.2	12.0	8.5
R3_CAM1 [°]	9.8	2.8	-2.3	10.7	3.6	11.9	9.3	8.7	14.7	5.7	7.5	5.0
R3_CATAM1 [°]	9.0	4.4	-2.7	3.3	0.1	10.4	8.6	6.4	13.2	0.2	5.3	5.1
R3_TAM1 [°]	1.9	5.3	4.5	18.5	4.8	29.5	29.5	-6.4	-3.8	17.7	10.2	12.9

Table 20 (Pre-op) - (Post op) differences of the analysed measurements for all the scans. On the left the average over all the patients and related standard deviation are reported.

(Pre-op)-(Post-op) differences were evaluated for normality with the Shapiro-Wilk test and all of them showed a normal distribution, except for RL_TACA because of an outlier. For instance, RL_TACA of SM scan shows a pre-post difference much higher than the other ones. Therefore, where the distribution of the data was found to be normal, Student's paired-t test was used for comparison between pre-op and post-op values; otherwise,

Wilcoxon rank-sum tests was applied. In the table below T-test and Wilcoxon Rank Sum test p-values are shown (Table 21).

	P value
IL_TA [°]	2.90E-05
IL_CA_lit. [°]	1.79E-02
IT_TA [°]	1.62E-04
IT_CA [°]	2.02E-03
HAA_Will_lit. [°]	2.78E-03
RL_TACA [°]	3.79E-04 *
RT_TANA [°]	6.61E-05
RL_CAM1 [°]	2.10E-03
RL_CATAM1_lit. [°]	2.59E-05
RL_TAM1_lit. [°]	1.21E-05
RT_TAM1 [°]	1.62E-02
RT_M1M2 [°]	2.69E-03
FAO_lit. [%]	2.14E-04
Hg_NA_c [mm]	4.46E-04
Hg_CU_c [mm]	7.15E-01
Hg_CM_c [mm]	2.40E-04
Hg_NA [mm]	1.57E-04
Hg_CU [mm]	3.51E-02
Hg_CM [mm]	3.21E-04
I3_CA [°]	7.14E-02
I3_TA [°]	2.65E-05
R3_TICA [°]	9.76E-01
R3_TACA [°]	5.41E-04
R3_TANA [°]	1.64E-03
R3_CAM1 [°]	1.11E-03
R3_CATAM1 [°]	9.74E-03
R3_TAM1 [°]	3.45E-02

*Table 21 T-test p-values. *RL_TACA is the only Wilcoxon-rank sum p-value.*

Considering a p-value < 0.05 significant, 24 measurements out of 27 showed significant differences between the pre-op and post-op values. The only exceptions are Hg_CU_c, I3_CA and R3_TICA. The former is due to the fact that the cuboid bone remains very close to the original position after the surgery, reducing its hight from the soil. It was explained by the fact that the position of the cuboid compensates the uprising of the MLA bones. Concerning I3_CA, the calcaneus remained almost in the same position during the surgery, while the talus is moved on it, so, the values of its inclination does not change

significantly. Finally, R3_TICA is an attempt of representing the hindfoot alignment using 3D axes, however this measurement has a difficult geometrical interpretation, so other ways to observe the 3D hindfoot alignment are necessary.

Eventually, the method presented in this study showed promising outcomes, well highlighting the changing of morphology pre and post operatively, this was demonstrated by the differences between the pre-op and post-op measurements, which are statistically significant and coherent with the images of the 3D foot model. Moreover, these high differences between pre-op and post-op find also support in the clinic. For instance, FPI (Foot Posture Index) and FFI (Foot Function Index) diagnostic clinical indices were recorded in the pre-op and in the post-op and reported below (Table 22). The former is the clinical assessment of foot deformity, the latter is an index concerning the foot functionality and pain Unfortunately, FPI and FFI of only 9 out of 10 patients were available because DER indices were not recorded in the post-op.

	FPI PRE-OP	FPI POST-OP	FFI PRE-OP	FFI POST-OP
AC	12	0	52.4	2.9
BA	6	4	67.1	8
CP	12	1	84.7	7.1
DN	12	5	67.7	56.5
LM	8	1	57.1	24.7
MM	12	2	34.7	25.3
SM	8	3	77.6	8
TV	12	3	76.5	2
VL	10	5	69.4	8.4
Average	10.2	2.7	65.2	15.9
sd	2.3	1.8	15.2	17.4

Table 22 FPI and FFI comparison between pre-op and post-op.

Overall, the clinical evaluation of foot deformity and pain improved in all the patients, the FPI average went from 10.2 to 2.7 and the FFI average from 65.2 to 15.9. Furthermore, a linear regression model was applied on pre-op differences in order to derive correlations between the variation of these clinical indices and all the geometrical measurements. The results are reported in the Table 23 below.

	FPI (PRE-POST)			FFI (PRE-POST)		
Measurement PRE-POST	r	r^2	P_value	r	r^2	P_value
IL_TA [°]	-0.70*	0.49*	0.04*	0.12	0.01	0.76
IL_CA_lit. [°]	0.06	0.00	0.87	-0.14	0.02	0.72
IT_TA [°]	-0.70*	0.49*	0.03*	0.21	0.04	0.60
IT_CA [°]	-0.44	0.19	0.23	0.62	0.38	0.08
HAA_Will [°]	-0.64	0.41	0.06	0.44	0.19	0.24
RL_TACA [°]	-0.07	0.00	0.87	0.20	0.04	0.61
RT_TANA [°]	0.53	0.28	0.15	-0.02	0.00	0.95
RL_CAM1 [°]	-0.31	0.10	0.42	0.27	0.07	0.48
RL_CATAM1 [°]	-0.55	0.30	0.12	0.00	0.00	1.00
RL_TAM1 [°]	0.78*	0.61*	0.01*	-0.29	0.08	0.46
RT_TAM1 [°]	0.66	0.44	0.05	-0.35	0.12	0.35
RT_M1M2 [°]	-0.65	0.42	0.06	0.57	0.32	0.11
FAO [%]	-0.48	0.23	0.19	0.25	0.06	0.51
Hg_NA_c [mm]	0.79*	0.62*	0.01*	-0.37	0.14	0.33
Hg_CU_c [mm]	0.55	0.30	0.12	-0.45	0.20	0.23
Hg_CM_c [mm]	0.86*	0.74*	0.00*	-0.55	0.30	0.13
Hg_NA [mm]	0.77*	0.59*	0.02*	-0.27	0.07	0.48
Hg_CU [mm]	0.34	0.12	0.37	-0.25	0.06	0.51
Hg_CM [mm]	0.86*	0.74*	0.00*	-0.63	0.40	0.07
I3_CA [°]	0.06	0.00	0.88	-0.11	0.01	0.78
I3_TA [°]	-0.68*	0.46*	0.04*	0.36	0.13	0.34
R3_TICA [°]	-0.01	0.00	0.98	-0.22	0.05	0.56
R3_TACA [°]	-0.72*	0.52*	0.03*	0.19	0.04	0.62
R3_TANA [°]	-0.06	0.00	0.89	-0.66	0.44	0.05
R3_CAM1 [°]	-0.32	0.10	0.40	0.27	0.07	0.49
R3_CATAM1 [°]	-0.40	0.16	0.29	0.26	0.07	0.50
R3_TAM1 [°]	-0.30	0.09	0.42	-0.31	0.10	0.42

Table 23 Pearson product–moment correlation coefficient (r) and its squared form (r^2), i.e. the coefficient of determination, showing the correlation between FPI and FFI with the geometrical measurements. (statistically significant correlations are indicated with "").*

Statistically significance correlation was found between FPI and 9 out of 27 geometrical measurements (IL_TA, IT_TA, RL_TAM1, Hg_NA_c, Hg_NA, Hg_CM_c, Hg_CM, I3_TA, R3_TACA), while non-Statistically significance correlation was found between FFI and any of the geometrical data. This is an expected result, because FPI is the clinical assessment of foot deformity, that is the same purpose of the presented objective measurements, while FFI is an index concerning the foot functionality and pain. Moreover, comparing 3D and 2D measurements, it is noticeable that there is correlation between FPI and R3_TACA, but not between FPI and RL_TACA, which is the corresponding 2D measurement. On the other hand, the correlation between the 3D measurement I3_TA and FPI (r^2 = 0.46) is similar to the correlation between FPI and IL_TA (r^2=0.48) and between FPI and IT_TA (r^2=0.49), which are the corresponding 2D measurements.

Chapter 7: Discussion and conclusion

In the clinical assessment of foot and ankle pathologies, the state-of-the-art technique is X-rays (radiographs) imaging. It provides 2D weight-bearing images but affected by rotational and projection errors as well as operator bias. On the other hand, the standard CT provides technicians with one 3D dataset, multiplane reformation, automated image analysis but it does not allow for the loading that is acting on the joints in the natural standing position, i.e. non 'natural' weight bearing. Since 2011, with the advent of CBCT (Cone Beam CT), a combination of all the benefits mentioned before was provided and exploited for the present work. In fact, CBCT has a high spatial resolution that allows to perfectly acquire bones and to assess their 3D relationships and alignments. Moreover, other advantages include fast image acquisition time, low radiation dosage, and its ergonomics. Using this technique, scans of the feet were obtained, from which 3D bone models for each patient were built up by means of MIS (Mimics Innovation Suite, Materialise), the state-of-the-art segmentation tool, and properly analysed on Matlab and Geomagic. The aim of this procedure is to have a semi-automatic, non-operator dependent, reliable, and robust characterization of foot bones morphology, alignment, and architecture.

The only step of this method that could be affected by operator-dependent errors is the segmentation process, since the subsequent computation of bones axes and their absolute or relative angles is fully automatic. Therefore, an intra-operator and inter-operator analysis was carried out segmenting three different scans. In the first case these were segmented by the same operator in three different time moments, in the second case, the same scans were segmented by three different operators. By means of the ICCs (Intraclass Correlation Coefficient), it has been demonstrated an excellent intra-operator and inter-operator repeatability on average. The main issue, during the segmentation process, is that the operator must choose whether to segment the osteophytes. This is not always an easy choice, especially if it is not clear whether these are in contact with the bone of interest or not. Moreover, it could happen that an osteophyte is linked to two adjacent bones, so the operator can choose to segment it with one of the two bones or to split it into two different parts. Therefore, foot morphological deformities could lead to differences in operators'

decisions. Nevertheless, only 2 out of 27 measurements had an ICC lower than 0.9, but still higher than 0.75, hence this process can be considered intra- and inter-operator repeatable.

Once the repeatability has been demonstrated, the foot morphological analysis procedure showed the effectiveness of using a fully automatic method for the characterisation of the bone models, capable of making repeatable and reliable measurements not affected by mispositioning of the foot and operator bias. To this regard, characterisation of 10 post-op feet was also conducted, as an instance to show how these measurements can provide a detailed overview of both a multi-segmental and multi-planar realignment of bones achieved after surgery. In fact, the differences between pre-op and post-op values showed a statistically significant difference. Moreover, the results obtained from the pre-op versus post-op evaluation were very encouraging, for example, the major deformities involving hindfoot valgus, MLA (Medial Longitudinal Arch) collapse and forefoot abduction of symptomatic adult foot, revealed high improvements. It is interesting because all the changes inside the foot are due only to the surgical hindfoot alignment, demonstrating how all the bones and the structures are interconnected, forming a multi-segment complex, where a single modification affects the whole architecture. Moreover, a correlation between FPI (Foot Posture Index) and 9 out of 27 measurements was assessed, showing how this clinical index, which is a qualitative evaluation of foot deformity improved as some of the geometrical measurements that have the same purpose.

In routine clinical assessments, which necessarily needs a quantitative response, also qualitative views of the 3D model of the feet can play a crucial role in the evaluation of 3D foot morphology, deformities and correction. For instance, images representing the 3D model of the feet can help the interpretation of the numerical data and represent an optimal way of communicating with the clinical staff. In particular, the surgeons found in these images a confirmation of what they expected. Moreover, the observation of the 3D model can lead to the understanding of the reasons of a less successful outcome. One clear example is reported in the paragraph 6.4 where the cases DN, LM DER were presented. LM showed a high improvement of the whole architecture form the hindfoot to the forefoot, while cases DN and DER presented a similar correction in the hindfoot, but very different modification in the forefoot. In particular, they were both very deformed feet, more than the average, and showed that a comparable hindfoot alignment can lead to very different changes in the forefoot correction. The explanation comes from the direct observation of the midfoot bones, that showed a more severe collapse of the navicular at

the navicular-cuneiform joint in DN than in DER, making the correction of the hindfoot not sufficient to restore the correct architecture of the foot in DN. This variability between subjects is more complicated to understand just observing the numerical numbers. Hence, the use of pre-op and post-op images that represent the overlapping of bone structures gives a more complete view of the morphological improvement and of the complex interaction between the foot bones.

In conclusion the role of CBCT in the characterization of AAFD (Adult Acquired Flatfoot Deformity) and in its etiology comprehension is definitely greater than the other imaging modalities, proving to be an effective tool for a proper visualization of 3D foot and ankle morphology under functional loads. Even though new data processing and measuring techniques are required to take full advantage of CBCT 3D nature, the present procedure can be exploited in large clinical populations in case of retrospective and prospective clinical studies, as well as in complex biomechanical analyses. The method described in this work, for instance, showed promising outcomes, well characterizing the morphology of foot bones and capturing the changes in the architecture after the surgery. It can be a valid method to assess the severity of different types of foot deformities, to help the surgeons in the decision process and to evaluate the outcomes of a particular surgical procedure.

However, the present work has some limitations. Regarding CBCT technology, standardization of the postures inside the gantry is still needed so that the amount of load can be exactly defined. Moreover, the image acquisition is limited by the size of the field-of-measurement of the scanner in the specific CBCT machine used for the acquisitions (Carestream, in this work). In fact, some scans presented not fully visible metatarsal heads, resulting in a lack of accuracy for those measurements involving the first metatarsal axis. As concerns the automatic PCA technique, it calculates the bone reference frames automatically. This might result, for some foot bones, in a non-traditional representation of the anatomical axes. Examples are RT_TANA that represents the talo-navicular coverage angle and IT_TA i.e., the talus absolute angle in the traversal plane: these both show the highest values for the standard deviations meaning that their axes are difficult to be defined due to the navicular and talus irregular shapes. In addition, a more robust dataset of control patients would be necessary, because such a small group of subjects cannot be considered as a valid normal population but just as a reference for understanding if the surgical

procedure brought the values to the right direction. However, the scan of physiological feet is actually hindered by ethical issues associated to radiation doses.

In the future, novel original measurements may be obtained, and more careful definitions of the bone anatomical frames shall be introduced, aiming at removing the anomalies associated to the asymmetry of some of the foot bones. For example, in addition to FAO, other new measures representing the overall foot deformities in a single parameter could be defined, to speed up the clinical decision-making process. Moreover, some of the possible future directions are the standardization of these measurements with reliable identification of anatomical landmarks, huge availability of 'normal' values, development of mechanical models that link static imaging with dynamic loading.

In addition, in the future, the time consumption of the entire procedure may be enhanced by automatic segmentation tools, such as DIS (Bonelogic® Ortho Foot and Ankle, Finlandia; Disior) and big data analysis. This may also be supported by modern modalities, such as Artificial Intelligence (AI). For instance, the role of AI is becoming predominant in modern life and in the clinic, supporting the diagnosis, prognosis, and the therapeutic decision-making process.

As concerning the CBCT, its future roles are the assessment of other foot deformities beside the AAFD both before and after surgery. The correlation of AAFD 3D parameters from CBCT with clinical outcomes will overcome the use of the state-of-the-art 2D imaging, which provides distorted projections of the bones. This makes learning how to diagnose and plan in this new world necessary. Next step in terms of imaging might be in four dimensions, and multi-tissue, in which the dynamic life of the foot could be within our grasp.

The interesting challenge will be how to correctly refine the process that will gradually lead to these new tools, so that their future use might provide the patients with the maximum efficient care while remaining within the reasonable boundaries of what is considered ethically acceptable.

Bibliography

Akoh CC, Phisitkul P. Clinical Examination and Radiographic Assessment of the Cavus Foot. *Foot and ankle clinics*. 2019;24(2). doi:10.1016/j.fcl.2019.02.002

Barg A, Bailey T, Richter M, et al. Weightbearing Computed Tomography of the Foot and Ankle: Emerging Technology Topical Review. *Foot & Ankle International*. 2018;39(3). doi:10.1177/1071100717740330

Belvedere C, Giacomozzi C, Carrara C, et al. Correlations between weight-bearing 3D bone architecture and dynamic plantar pressure measurements in the diabetic foot. *Journal of Foot and Ankle Research*. 2020;13(1). doi:10.1186/s13047-020-00431-x

Benedetti MG, Berti L, Straudi S, Ceccarelli F, Giannini S. Clinicoradiographic Assessment of Flexible Flatfoot in Children. *Journal of the American Podiatric Medical Association*. 2010;100(6). doi:10.7547/1000463

Bücking TM, Hill ER, Robertson JL, Maneas E, Plumb AA, Nikitichev DI. From medical imaging data to 3D printed anatomical models. *PLOS ONE*. 2017;12(5). doi:10.1371/journal.pone.0178540

Burssens A, Peeters J, Buedts K, Victor J, Vandeputte G. Measuring hindfoot alignment in weight bearing CT: A novel clinical relevant measurement method. *Foot and Ankle Surgery*. 2016;22(4). doi:10.1016/j.fas.2015.10.002

Byrne N, Forte MV, Tandon A, Valverde I, Hussain T. A systematic review of image segmentation methodology, used in the additive manufacture of patient-specific 3D printed models of the cardiovascular system. *JRSM Cardiovascular Disease*. 2016;5. doi:10.1177/2048004016645467

Caravaggi P, Sforza C, Leardini A, Portinaro N, Panou A. Effect of plano-valgus foot posture on midfoot kinematics during barefoot walking in an adolescent population. *Journal of Foot and Ankle Research*. 2018;11(1). doi:10.1186/s13047-018-0297-7

Carrara C, Belvedere C, Caravaggi P, Durante S, Leardini A. Techniques for 3D foot bone orientation angles in weight-bearing from cone-beam computed tomography. *Foot and Ankle Surgery*. 2021;27(2). doi:10.1016/j.fas.2020.03.013

Carrara C, Caravaggi P, Belvedere C, Leardini A. Radiographic angular measurements of the foot and ankle in weight-bearing: A literature review. *Foot and Ankle Surgery*. 2020;26(5). doi:10.1016/j.fas.2019.07.008

Carrino JA, Muhit AA, Zbijewski W, et al. Dedicated Cone-Beam CT System for Extremity Imaging. *Radiology*. 2014;270(3). doi:10.1148/radiol.13130225

Chepurnyi Y, Chernohorskyi D, Zhukovtceva O, Poutala A, Kopchak A. Automatic evaluation of the orbital shape after application of conventional and patient-specific

implants: Correlation of initial trauma patterns and outcome. *Journal of Oral Biology and Craniofacial Research*. 2020;10(4). doi:10.1016/j.jobcr.2020.10.003

Cody EA, Williamson ER, Burket JC, Deland JT, Ellis SJ. Correlation of Talar Anatomy and Subtalar Joint Alignment on Weightbearing Computed Tomography With Radiographic Flatfoot Parameters. *Foot & Ankle International*. 2016;37(8). doi:10.1177/1071100716646629

Cody EA, Williamson ER, Burket JC, Deland JT, Ellis SJ. Correlation of Talar Anatomy and Subtalar Joint Alignment on Weightbearing Computed Tomography With Radiographic Flatfoot Parameters. *Foot & Ankle International*. 2016;37(8). doi:10.1177/1071100716646629

Dayton P, Feilmeier M, Hirschi J, Kauwe M, Kauwe JSK. Observed Changes in Radiographic Measurements of the First Ray after Frontal Plane Rotation of the First Metatarsal in a Cadaveric Foot Model. *The Journal of Foot and Ankle Surgery*. 2014;53(3). doi:10.1053/j.jfas.2014.01.002

Deland JT. Adult-acquired Flatfoot Deformity. *Journal of the American Academy of Orthopaedic Surgeons*. 2008;16(7). doi:10.5435/00124635-200807000-00005

Durastanti G, Belvedere C, Faldini C, Grant B, Sintini B, Mazzotti A, Durante S, Leardini A. Chirurgia piede e caviglia. Riprotesizzazione della caviglia: protesi custom-made. *Giornale Italiano di Ortopedia e Traumatologia*. 2019A

Durastanti G, Leardini A, Siegler S, Durante S, Bazzocchi A, Belvedere C. Comparison of cartilage and bone morphological models of the ankle joint derived from different medical imaging technologies. *Quantitative Imaging in Medicine and Surgery*. 2019B;9(8). doi:10.21037/qims.2019.08.08

Fernández-Seguín LM, Heredia-Rizo AM, Díaz-Mancha JA, González-García P, Ramos-Ortega J, Munuera-Martínez PV. Immediate and short-term radiological changes after combining static stretching and transcutaneous electrical stimulation in adults with cavus foot. *Medicine*. 2019;98(46). doi:10.1097/MD.0000000000018018

Ferri M, Scharfenberger AV, Goplen G, Daniels TR, Pearce D. Weightbearing CT Scan of Severe Flexible Pes Planus Deformities. *Foot & Ankle International*. 2008;29(2). doi:10.3113/FAI.2008.0199

Flores DV, Gómez CM, Hernando MF, Davis MA, Pathria MN. Adult Acquired Flatfoot Deformity: Anatomy, Biomechanics, Staging, and Imaging Findings. *RadioGraphics*. 2019;39(5). doi:10.1148/rg.2019190046

Gentchos CE, Anderson JG, Bohay DR. Management of the Rigid Arthritic Flatfoot in the Adults. *Foot and Ankle Clinics*. 2012;17(2). doi:10.1016/j.fcl.2012.03.009

GRICE DS. An extra-articular arthrodesis of the subastragalar joint for correction of paralytic flat feet in children. *The Journal of bone and joint surgery American volume*. 1952;34.

Gwani AS, Asari MA, Ismail ZIM. How the three arches of the foot intercorrelate. *Folia Morphologica*. 2017;76(4). doi:10.5603/FM.a2017.0049

Hamard M, Neroladaki A, Bagetakos I, Dubois-Ferrière V, Montet X, Boudabbous S. Accuracy of cone-beam computed tomography for syndesmosis injury diagnosis compared to conventional computed tomography. *Foot and Ankle Surgery*. 2020;26(3). doi:10.1016/j.fas.2019.03.006

Harris EJ. The Natural History and Pathophysiology of Flexible Flatfoot. *Clinics in Podiatric Medicine and Surgery*. 2010;27(1). doi:10.1016/j.cpm.2009.09.002

Hirschmann A, Pfirrmann CWA, Klammer G, Espinosa N, Buck FM. Upright Cone CT of the hindfoot: Comparison of the non-weight-bearing with the upright weight-bearing position. *European Radiology*. 2014;24(3). doi:10.1007/s00330-013-3028-2

Johnson KA, Strom DE. Tibialis posterior tendon dysfunction. *Clinical orthopaedics and related research*. 1989;(239).

Kärkkäinen M, Wilkman T, Mesimäki K, Snäll J. Primary reconstruction of orbital fractures using patient-specific titanium milled implants: the Helsinki protocol. *British Journal of Oral and Maxillofacial Surgery*. 2018;56(9). doi:10.1016/j.bjoms.2018.08.008

Keenan AM, Redmond AC, Horton M, Conaghan PG, Tennant A. The Foot Posture Index: Rasch Analysis of a Novel, Foot-Specific Outcome Measure. *Archives of Physical Medicine and Rehabilitation*. 2007;88(1). doi:10.1016/j.apmr.2006.10.005

Kevles Bettyann. Naked to the Bone: Medical Imaging in the Twentieth Century. 1997

Kido M, Ikoma K, Imai K, et al. Load Response of the Tarsal Bones in Patients with Flatfoot Deformity: In Vivo 3D Study. *Foot & Ankle International*. 2011;32(11). doi:10.3113/FAI.2011.1017

Koivisto J, Kiljunen T, Kadesjö N, Shi XQ, Wolff J. Effective radiation dose of a MSCT, two CBCT and one conventional radiography device in the ankle region. *Journal of Foot and Ankle Research*. 2015;8(1). doi:10.1186/s13047-015-0067-8

Koo TK, Li MY. A Guideline of Selecting and Reporting Intraclass Correlation Coefficients for Reliability Research. *Journal of Chiropractic Medicine*. 2016;15(2). doi:10.1016/j.jcm.2016.02.012

Lamm BM, Stasko PA, Gesheff MG, Bhave A. Normal Foot and Ankle Radiographic Angles, Measurements, and Reference Points. *The Journal of Foot and Ankle Surgery*. 2016;55(5). doi:10.1053/j.jfas.2016.05.005

Leardini A, Durante S, Belvedere C, et al. Weight-bearing CT Technology in Musculoskeletal Pathologies of the Lower Limbs: Techniques, Initial Applications, and Preliminary Combinations with Gait-Analysis Measurements at the Istituto Ortopedico Rizzoli. *Seminars in Musculoskeletal Radiology*. 2019;23(06). doi:10.1055/s-0039-1697939

Lenz AL, Strobel MA, Anderson AM, et al. Assignment of local coordinate systems and methods to calculate tibiotalar and subtalar kinematics: A systematic review. *Journal of Biomechanics*. 2021;120. doi:10.1016/j.jbiomech.2021.110344

Lintz F, Netto C de C, Barg A, Burssens A, Richter M, Group WBCIS. Weight-bearing cone beam CT scans in the foot and ankle. *EFORT Open Reviews*. 2018;3(5). doi:10.1302/2058-5241.3.170066

Lintz F, Welck M, Bernasconi A, et al. 3D Biometrics for Hindfoot Alignment Using Weightbearing CT. *Foot & Ankle International*. 2017;38(6). doi:10.1177/1071100717690806

Mann RA, Thompson FM. Rupture of the posterior tibial tendon causing flat foot. Surgical treatment. *The Journal of bone and joint surgery American volume*. 1985;67(4).

Martinelli N, Scotto GM, Sartorelli E, Bonifacini C, Bianchi A, Malerba F. Reliability, validity and responsiveness of the Italian version of the Foot Function Index in patients with foot and ankle diseases. *Quality of Life Research*. 2014;23(1). doi:10.1007/s11136-013-0435-4

Matsiushevich K, Belvedere C, Leardini A, Durante S. Quantitative comparison of freeware software for bone mesh from DICOM files. *Journal of Biomechanics*. 2019;84. doi:10.1016/j.jbiomech.2018.12.031

Maynou C, Szymanski C, Thiounn A. The adult cavus foot. *EFORT Open Reviews*. 2017;2(5). doi:10.1302/2058-5241.2.160077

Mazis GA, Sakellariou VI, Kanellopoulos AD, Papagelopoulos PJ, Lyras DN, Soucacos PN. Results of Extra-Articular Subtalar Arthrodesis in Children with Cerebral Palsy. *Foot & Ankle International*. 2012;33(6). doi:10.3113/FAI.2012.0469

Menz HB, Munteanu SE, Zammit GV, Landorf KB. Foot structure and function in older people with radiographic osteoarthritis of the medial midfoot. *Osteoarthritis and Cartilage*. 2010;18(3). doi:10.1016/j.joca.2009.11.010

Mosca M, Caravelli S, Vannini F, et al. Mini Bone Block Distraction Subtalar Arthrodesis (SAMBB) in the Management of Acquired Adult Flatfoot with Subtalar Arthritis: A Modification to the Grice–Green Procedure. *Joints*. 2019;07(02). doi:10.1055/s-0039-3400452

Mosca M, Caravelli S, Vocale E, et al. Outcome After Modified Grice-Green Procedure (SAMBB) for Arthritic Acquired Adult Flatfoot. *Foot & Ankle International*. 2020;41(11). doi:10.1177/1071100720938665

Mozzo P, Procacci C, Tacconi A, Martini PT, Andreis IAB. A new volumetric CT machine for dental imaging based on the cone-beam technique: preliminary results. *European Radiology*. 1998;8(9). doi:10.1007/s003300050586

Myerson MS. Adult acquired flatfoot deformity: treatment of dysfunction of the posterior tibial tendon. *Instructional course lectures*. 1997;46.

Myerson MS, Thordarson DB, Johnson JE, et al. Classification and Nomenclature: Progressive Collapsing Foot Deformity. *Foot & Ankle International*. 2020;41(10). doi:10.1177/1071100720950722

Netto C de C, Bang K, Mansur NS, et al. Multiplanar Semiautomatic Assessment of Foot and Ankle Offset in Adult Acquired Flatfoot Deformity. *Foot & Ankle International*. 2020;41(7). doi:10.1177/1071100720920274

Netto C de C, Schon LC, Thawait GK, et al. Flexible Adult Acquired Flatfoot Deformity. *Journal of Bone and Joint Surgery*. 2017;99(18). doi:10.2106/JBJS.16.01366

Ortolani M, Leardini A, Pavani C, et al. Angular and linear measurements of adult flexible flatfoot via weight-bearing CT scans and 3D bone reconstruction tools. *Scientific Reports*. 2021;11(1). doi:10.1038/s41598-021-95708-x

Posadzy M, Desimpel J, Vanhoenacker F. Cone beam CT of the musculoskeletal system: clinical applications. *Insights into Imaging*. 2018;9(1). doi:10.1007/s13244-017-0582-1

Richter M, Lintz F, Netto C de C, Barg A, Burssens A. Results of more than 11,000 scans with weightbearing CT — Impact on costs, radiation exposure, and procedure time. *Foot and Ankle Surgery*. 2020;26(5). doi:10.1016/j.fas.2019.05.019

Richter M, Seidl B, Zech S, Hahn S. PedCAT for 3D-imaging in standing position allows for more accurate bone position (angle) measurement than radiographs or CT. *Foot and Ankle Surgery*. 2014;20(3). doi:10.1016/j.fas.2014.04.004

Saltzman CL, El-Khoury GY. The Hindfoot Alignment View. *Foot & Ankle International*. 1995;16(9). doi:10.1177/107110079501600911

Shakoor D, Netto C de C, Thawait GK, et al. Weight-bearing radiographs and cone-beam computed tomography examinations in adult acquired flatfoot deformity. *Foot and Ankle Surgery*. 2021;27(2). doi:10.1016/j.fas.2020.04.011

Shelton TJ, Singh S, Robinson EB, et al. The Influence of Percentage Weight-Bearing on Foot Radiographs. *Foot & Ankle Specialist*. 2019;12(4). doi:10.1177/1938640018810412

Snäll J, Narjus-Sterba M, Toivari M, Wilkman T, Thorén H. Does postoperative orbital volume predict postoperative globe malposition after blow-out fracture reconstruction? A 6-month clinical follow-up study. *Oral and Maxillofacial Surgery*. 2019;23(1). doi:10.1007/s10006-019-00748-3

Tulaya Prachgosin1, Desmond y.r. Chong2, Wipawan Leelasamran3, Pruittikorn Smithmaitrie4, Surapong Chatpun. Medial longitudinal arch biomechanics evaluationduring gait in subjects with flexible flatfoot. *Acta of Bioengineering and BiomechanicsOriginal paper* Vol. 17, No. 4.
doi: 10.5277/ABB-00296-2015-02

Tuominen EKJ, Kankare J, Koskinen SK, Mattila KT. Weight-Bearing CT Imaging of the Lower Extremity. *American Journal of Roentgenology*. 2013;200(1). doi:10.2214/AJR.12.8481

Virzì A, Muller CO, Marret JB, et al. Comprehensive Review of 3D Segmentation Software Tools for MRI Usable for Pelvic Surgery Planning. *Journal of Digital Imaging*. 2020;33(1). doi:10.1007/s10278-019-00239-7

Williamson ERC, Chan JY, Burket JC, Deland JT, Ellis SJ. New Radiographic Parameter Assessing Hindfoot Alignment in Stage II Adult-Acquired Flatfoot Deformity. *Foot & Ankle International*. 2015;36(4). doi:10.1177/1071100714558846

Wu G, Siegler S, Allard P, et al. ISB recommendation on definitions of joint coordinate system of various joints for the reporting of human joint motion–part I: ankle, hip, and spine. International Society of Biomechanics. *Journal of biomechanics*. 2002;35(4). doi:10.1016/s0021-9290(01)00222-6

Zhang Y, Xu J, Wang X, et al. An *in vivo* study of hindfoot 3D kinetics in stage II posterior tibial tendon dysfunction (PTTD) flatfoot based on weight-bearing CT scan. *Bone & Joint Research*. 2013;2(12). doi:10.1302/2046-3758.212.2000220

Zhou Y, Zhou B, Liu J, et al. A prospective study of midfoot osteotomy combined with adjacent joint sparing internal fixation in treatment of rigid pes cavus deformity. *Journal of Orthopaedic Surgery and Research*. 2014;9(1). doi:10.1186/1749-799X-9-44